Papers Presented at the

th

annual

SUMMER INTERN CONFERENCE

August 13, 2009 — Houston, Texas

Papers Presented at the

Twenty-Fifth Annual Summer Intern Conference

August 13, 2009
Houston, Texas

2009 Summer Intern Program for Undergraduates
Lunar and Planetary Institute

Sponsored by
Lunar and Planetary Institute
NASA Johnson Space Center

Compiled in 2009 by

Publications and Program Services Department
Lunar and Planetary Institute 3600 Bay Area Boulevard
Houston TX 77058-1113

Material in this volume may be copied without restraint for library, abstract service, education, or personal research purposes; however, republication of any paper or portion thereof requires the written permission of the authors as well as appropriate acknowledgement of this publication.

The Lunar and Planetary Institute is operated by the Universities Space Research Association and supported by the National Aeronautics and Space Administration under Cooperative Agreement No. NCC5-679 issued through the Solar System Exploration Division.

Any opinions, findings, and conclusions or recommendations expressed in this volume are those of the author(s) and do not necessarily reflect the views of the National Aeronautics and Space Administration.

AGENDA

8:00 a.m. Breakfast

8:20 a.m. Opening Statements by Dr. Julie Moses, Chair and Staff Scientist

8:30 a.m. **DENISE ANDERS, University of Kiel** (Advisors: D. A. Kring and A. Wittmann)
Carbonate-rich Phases of Meteor Crater Impact Melt Particles

8:45 a.m. **NATTAVADEE SRISUTTHIYAKORN, University of Michigan** (Advisors: W. S. Kiefer and M. Kirchoff)
Mapping the Magmatic Plumbing System in the Marius Hills

9:00 a.m. **ELENA AMADOR, University of California, Santa Cruz** (Advisors: C. C. Allen and D. Z. Oehler)
Regional Mapping and Spectral Analysis of Mounds in Acidalia Planitia, Mars

9:15 a.m. **STEVEN ARAUZA, University of Texas at Austin** (Advisors: J. H. Jones and D. W. Mittlefehldt)
Testing EETA79001 Lithology B, a Martian Basalt

9:30 a.m. **SAMUEL BELL, Amherst College** (Advisors: J. Lasue and T. F. Stepinski)
Automated Classification of the JSC Cosmic Dust Catalog Volume 15

9:45 a.m. **JENNIFER BUZ, Massachusetts Institute of Technology** (Advisor: P. J. McGovern)
Venusian Volcanoes and the Internal Thermal State of Venus

10:00 a.m. **COURTNEY KING, University of Arizona** (Advisors: K. Righter and L. Danielson)
Determining the Metal/Silicate Partition Coefficient of Germanium: Implications for Core and Mantle Differentiation

10:15 a.m. **LAURA MALONE, University of New Brunswick** (Advisors: A. Wittmann and D. A. Kring)
Shock-Petrographic Study of Impactites from the Chesapeake Bay Crater

10:30 a.m. Break

10:45 a.m. **JONATHAN MCLANE, University of Minnesota** (Advisor: T. F. Stepinski)
Progress in Mapping Depth of Impact Craters on Mars

11:00 a.m. **CHELSEA PAYNE, University of Wisconsin – River Falls** (Advisor: P. D. Spudis)
Scattering Properties of Lunar Geological Units Revealed by the Mini-SAR Imaging Radar, Chandrayaan-1 Mission

11:15 a.m. **KATIE ROBINSON, University of Chicago** (Advisor: A. H. Treiman)
Mineral Chemistry and Origin of Mare Basalt Fragments in Lunar Highland Meteorites

11:30 a.m. **SARAH SASLOW, University of Maryland** (Advisors: C. Visscher and J. I. Moses)
The Deep Water Abundance on Jupiter as Derived from Thermochemical Kinetic Modeling

11:45 a.m. **CHISATO SEKIGAWA, Kobe University** (Advisor: L. P. Keller)
The Mineralogy, Petrography and Chemistry of Comet Dust: Sulfides

12:00 p.m. **KEI SHIMIZU, Stony Brook University** (Advisors: W. L. Stefonov and C. A. Evans)
Assessment of a Handheld Forward Looking Infrared Camera as a Potential Lunar Field Geology Tool

12:15 p.m. **MICHELLE THOMPSON, Queens University** (Advisor: R. Christoffersen)
The Smallest Lunar Grains: Analysis of the <1 μm Size Fraction of Lunar Mare Soil 10084

12:30 p.m. **EMILY WORSHAM, University of Tennessee** (Advisor: P. B. Niles)
Experimental Constraints on Low Temperature Acid-Weathering of Olivine: Implications for Mars

12:45 p.m. Closing Remarks, Followed by Lunch

CONTENTS

Papers Presented at the

Twenty-Fifth Annual Summer Intern Conference

August 13, 2009
Houston, Texas

2009 Summer Intern Program for Undergraduates
Lunar and Planetary Institute

Sponsored by
Lunar and Planetary Institute
NASA Johnson Space Center

Compiled in 2009 by

Publications and Program Services Department
Lunar and Planetary Institute 3600 Bay Area Boulevard
Houston TX 77058-1113

Material in this volume may be copied without restraint for library, abstract service, education, or personal research purposes; however, republication of any paper or portion thereof requires the written permission of the authors as well as appropriate acknowledgement of this publication.

The Lunar and Planetary Institute is operated by the Universities Space Research Association and supported by the National Aeronautics and Space Administration under Cooperative Agreement No. NCC5-679 issued through the Solar System Exploration Division.

Any opinions, findings, and conclusions or recommendations expressed in this volume are those of the author(s) and do not necessarily reflect the views of the National Aeronautics and Space Administration.

AGENDA

8:00 a.m. Breakfast

8:20 a.m. Opening Statements by Dr. Julie Moses, Chair and Staff Scientist

8:30 a.m. **DENISE ANDERS, University of Kiel** (Advisors: D. A. Kring and A. Wittmann)
Carbonate-rich Phases of Meteor Crater Impact Melt Particles

8:45 a.m. **NATTAVADEE SRISUTTHIYAKORN, University of Michigan** (Advisors: W. S. Kiefer and M. Kirchoff)
Mapping the Magmatic Plumbing System in the Marius Hills

9:00 a.m. **ELENA AMADOR, University of California, Santa Cruz** (Advisors: C. C. Allen and D. Z. Oehler)
Regional Mapping and Spectral Analysis of Mounds in Acidalia Planitia, Mars

9:15 a.m. **STEVEN ARAUZA, University of Texas at Austin** (Advisors: J. H. Jones and D. W. Mittlefehldt)
Testing EETA79001 Lithology B, a Martian Basalt

9:30 a.m. **SAMUEL BELL, Amherst College** (Advisors: J. Lasue and T. F. Stepinski)
Automated Classification of the JSC Cosmic Dust Catalog Volume 15

9:45 a.m. **JENNIFER BUZ, Massachusetts Institute of Technology** (Advisor: P. J. McGovern)
Venusian Volcanoes and the Internal Thermal State of Venus

10:00 a.m. **COURTNEY KING, University of Arizona** (Advisors: K. Righter and L. Danielson)
Determining the Metal/Silicate Partition Coefficient of Germanium: Implications for Core and Mantle Differentiation

10:15 a.m. **LAURA MALONE, University of New Brunswick** (Advisors: A. Wittmann and D. A. Kring)
Shock-Petrographic Study of Impactites from the Chesapeake Bay Crater

10:30 a.m. Break

10:45 a.m. **JONATHAN MCLANE, University of Minnesota** (Advisor: T. F. Stepinski)
Progress in Mapping Depth of Impact Craters on Mars

11:00 a.m. **CHELSEA PAYNE, University of Wisconsin – River Falls** (Advisor: P. D. Spudis)
Scattering Properties of Lunar Geological Units Revealed by the Mini-SAR Imaging Radar, Chandrayaan-1 Mission

11:15 a.m. **KATIE ROBINSON, University of Chicago** (Advisor: A. H. Treiman)
Mineral Chemistry and Origin of Mare Basalt Fragments in Lunar Highland Meteorites

11:30 a.m. **SARAH SASLOW, University of Maryland** (Advisors: C. Visscher and J. I. Moses)
The Deep Water Abundance on Jupiter as Derived from Thermochemical Kinetic Modeling

11:45 a.m. **CHISATO SEKIGAWA, Kobe University** (Advisor: L. P. Keller)
The Mineralogy, Petrography and Chemistry of Comet Dust: Sulfides

12:00 p.m. **KEI SHIMIZU, Stony Brook University** (Advisors: W. L. Stefonov and C. A. Evans)
Assessment of a Handheld Forward Looking Infrared Camera as a Potential Lunar Field Geology Tool

12:15 p.m. **MICHELLE THOMPSON, Queens University** (Advisor: R. Christoffersen)
The Smallest Lunar Grains: Analysis of the <1 μm Size Fraction of Lunar Mare Soil 10084

12:30 p.m. **EMILY WORSHAM, University of Tennessee** (Advisor: P. B. Niles)
Experimental Constraints on Low Temperature Acid-Weathering of Olivine: Implications for Mars

12:45 p.m. Closing Remarks, Followed by Lunch

CONTENTS

REGIONAL MAPPING AND SPECTRAL ANALYSIS OF MOUNDS IN ACIDALIA PLANITIA, MARS.

Elena S. Amador[1], Carlton C. Allen[2], and Dorothy Z. Oehler[2, 1]University of California, Santa Cruz (Earth and Planetary Sciences, 1156 High St., Santa Cruz, CA 95064, eamador@ucsc.edu), [2] NASA – Johnson Space Center, Astromaterials Research and Exploration Science, 2101 NASAParkway, Houston, TX 77058.

Introduction: Acidalia Planitia is a nearly 3,000 km diameter planum located in the northern plains of Mars. It is believed to be a sedimentary basin containing an accumulation of sediments brought by various Hesperian outflow channels that drain the Highlands. A large number of high albedo mounds have been identified across this basin (Figure 1).

Farrand *et al.* [1] showed that the mounds were dark in THEMIS (Thermal Emission Imaging System) nighttime IR (infrared) image data, implying that the mounds have lower thermal inertia than that of the surrounding plains material (Figure 2). The relatively low thermal inertia can be interpreted to indicate that the material of the mounds is fine-grained or unconsolidated. Farrand et al., [1] also reviewed potential analogs for the mounds and concluded that a combination of mud volcanoes with evaporites around geysers or springs is most consistent with all the data.

We have built on the work of Farrand *et al*. using new data from HiRISE (High Resolution Imaging Science Experiment) and CRISM (Compact Reconnaissance Imaging Spectrometer for Mars) on MRO (Mars Reconnaissance Orbiter) and by creating regional maps of the features. Because these mounds have been identified across Acidalia, understanding the process that formed them will help us understand the history of this region.

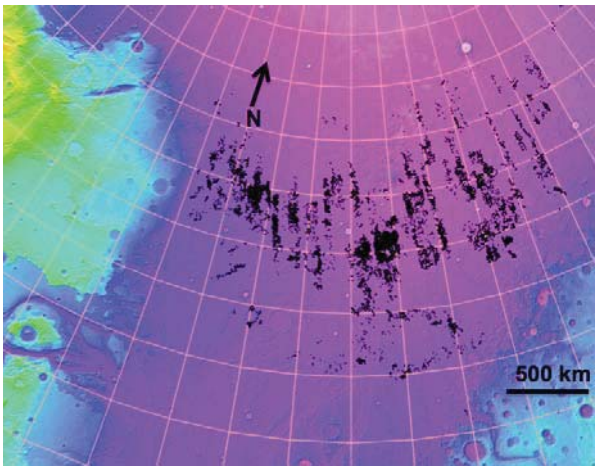

Figure 1. Regional map of Acidalia Planitia on a base map of MOLA (Mars Orbiter Laser Altimeter) data. Black points are mapped mounds.

Methods:

Regional Mapping. THEMIS nighttime and daytime IR images were analyzed using the ESRI software ArcGIS with image mosaics and recently mapped geology that were included in the Mars DVD v 1.4 provided by the USGS. Dark mounds found in nighttime IR images which were larger than three pixels (~300 m) were mapped. Approximately 40% of the southern Acidalia area was surveyed for such spots (Figure 1). Much of the northern region of Acidalia lacks good image data and mapping was not possible there. Stereo HiRISE images were used to obtain estimates of the relief of the mounds. Spatial densities were calculated across Acidalia by counting the number of mounds in three separate areas marked 1, 2, and 3 in Figure 3. Areas used ranged in size from about 22,000 to 29,000 km^2. Average diameters for the mounds were determined by analyzing four separate 1,000 km^2 areas, measuring the diameters of the mounds within each area, and averaging them.

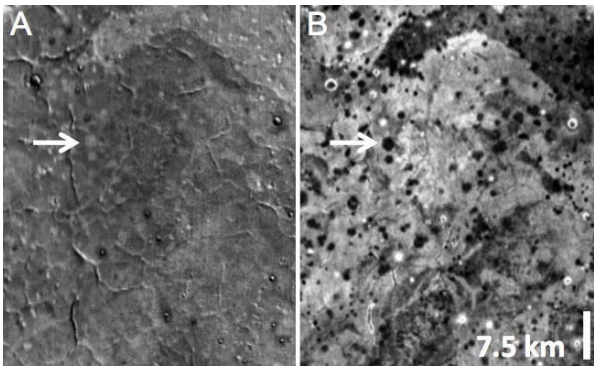

Figure 2. (A) THEMIS Daytime IR image and (B) the same area in THEMIS Nighttime IR. Arrows point to a bright mound in A and the same mound now dark in the nighttime IR, B.

CRISM. Hyperspectral VNIR (visible/near infrared) images from CRISM were examined for spectral differences between the mounds and plains material. Nine CRISM images covering areas in Acidalia with dark mounds identified in the THEMIS Nighttime IR were chosen to be analyzed. CRISM images were processed to remove atmospheric and instrumental noise, and spectra from the mounds were ratioed to spectra from surrounding plains. Both the visible (.4 to

1.1 μm) and IR (1.1 to 2.5 μm) wavelengths were evaluated.

In each CRISM image 5 to 11 ratios were created of mounds. Those ratios were then averaged to create one ratio to represent each image (Figure 4). To calculate ratios for the visible wavelengths, a denominator was created by averaging the spectra in a 25X25 pixel area of background material. The numerator was found by choosing a 5X5 pixel area on a desired mound. Ratios were created in the IR wavelengths using a 5X5 pixel area of the desired mound as the numerator and then a 5X5 pixel area of the background terrain as the denominator.

Results:

Regional Mapping. More than 18,000 mounds were mapped in southern Acidalia using the THEMIS nighttime IR image mosaic. Spatial densities of these mounds ranged from 21 per 1000 km^2 to 114 per 1000 km^2 (Table 1). Area 1 showed a relatively less dense region; mounds appeared to be spread further apart and had a larger average diameter size than in area 2. The mounds in area 1 were patterned in concentric half circles. Area 2 was the highest density region.

Large, well defined polygonal features, ranging from ~ 5 to 15 km across, dominate the region covered by area 3. This area had the lowest density of mounds, but the largest average mound diameter. Average diameters for the mounds range from 0.81 km to 1.06 km in diameter (Table 1). Relief of two mounds was estimated to be in the 100 – 200 m range using the stereo HiRISE images.

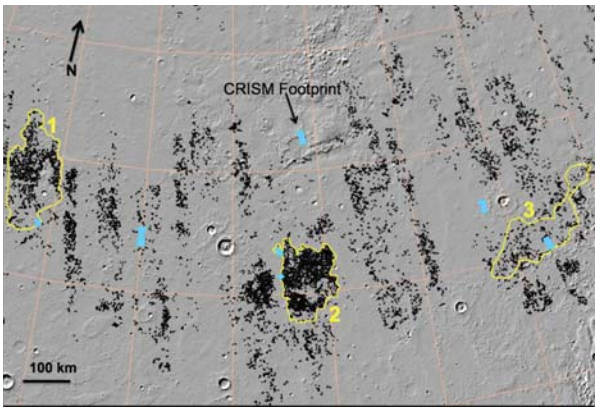

Figure 3. Black points represent mapped mounds. Yellow boundaries designate areas 1, 2, and 3.where density calculations and average diameter calculations were measured. Blue polygons show locations of 7 of the 9 successful CRISM footprints. The other two are off the map just to the east and west. MOLA altimetry background.

CRISM analysis. Ratio analysis of CRISM images showed that the mounds and surrounding terrain were similar in IR wavelengths, and that the mounds were spectrally neutral (Figure 4). However, in the visible wavelengths, ratios derived from all nine images showed that the mounds had a positive slope from .4 to .65 μm compared to the background, indicating the presence of ferric iron in the mounds (Figure 4). Previous work by Baker *et al*. **[2]**, suggested the presence of ferric iron in the visible range in one CRISM image in Acidalia Planitia. Our work has found similar indications of ferric iron enhancements associated with the mounds from the visible ratios in 9 images from across Acidalia.

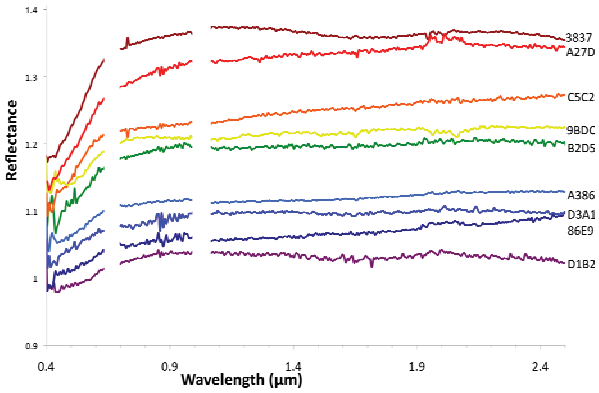

Figure 4. Each spectrum represents the average of ratios taken in each of the nine CRISM images. Numbers on the right are the CRISM image numbers. Note the positive slopes from .4 to ~ .6 μm.

Discussion: These analyses indicate three similarities among the mounds across Acidalia. In all nine areas the mounds 1) have a high albedo, 2) are bright in the THEMIS daytime IR images and dark in the nighttime IR images, and 3) appear to be more ferric than the background terrain.

Few differences between the mounds and plains were observed in the infrared portion of the CRISM data. However, the VIS portion of the spectrum did illustrate some differences. The positive slope from .4 to .65 μm of the mounds implies that they have more ferric iron than the surrounding background terrain. This is consistent with an interpretation that the mounds are more oxidized than the plains.

Possible explanations for the CRISM results might include the following: 1) It may be that the composition of the mounds is in fact different from that of the background material but that there is a low concentration of the differing material causing it to be difficult to detect. 2) It may be that the spectral signatures of minerals in the mounds are actually at a longer wave-

lengths than are investigated by the CRISM instrument. 3) Another possibility is that the mounds may be comprised of an amorphous material, which does not have a spectral signature, or 4) we may not be able to observe strong differences in the IR spectral signatures because the mounds may be coated by an alteration layer.

The high albedo mounds in Acidalia are abundant. With more than 18,000 being mapped in only a portion of the area, there are likely to be tens of thousands across the basin. This abundance suggests that the mounds represent a major geologic process in the northern plains. Most mounds superimpose the Vastitas Borealis Interior and Marginal units of the northern plains and therefore are younger than the Early Amazonian age proposed for those units [3]. These mounds therefore are among the youngest features in Acidalia.

The Acidalia Basin has likely received massive sediment deposition from the outflow channels surrounding it, creating intense pressures of the fine grained material. These regional relationships are consistent with a terrestrial analog of mud volcanoes [4].

On Earth, mud volcanoes form in areas of rapid sedimentation or accretionary wedges where there are highly pressured, fine grained sediments. Any gas or fluid that is trapped underneath the sediments can be brought to the surface due to density differences associated with overpressure. Acidalia appears to be a prime environment for such a process.

The mapped mounds are limited to the Acidalia basin area indicating that the origin of these mounds may correlate with some aspect of the geology of this particular basin. The spatial densities and diameters have large ranges but this would be consistent with a terrestrial mud volcano analog, as terrestrial mud volcanoes show highly variable densities and diameters from meters to kilometers. For example, mud volcanoes in Azerbaijan have spatial densities of approximately 20 mounds per 1,000 km^2, consistent with the lower of the spatial densities found in Acidalia.

The CRISM data also are consistent with this analog as mud volcanoes would be expected to be fairly similar in composition to materials of the plains but might also show enhanced alteration due to the subsurface flow of fluid-rich sediments.

Location	**Area *(km^2)***	**Number of mounds**	**Spatial Density *(No. of Mounds/ 1,000 km^2)***	**Avg. Diameter of mounds in 1,000 km^2 area *(m)***
1	28,822.50	1499	52	1019
2	22,238.90	2546	114	811
3	22,790.00	476	21	1060

Table 1. Table shows spatial densities and average diameter sizes for the three locations.

Future Work: Continued mapping of the mounds will be conducted to determine the relationship of the mounds to the basin boundaries, to the giant polygons that traverse the region, and to possible fractures.

More analysis of the CRISM data and the composition of the plains may help understand the history of Acidalia and the nature of the mounds with relation to the character of the plains in the nighttime IR.

Summary: High albedo mounds in Acidalia Planitia, Mars appear to best resemble terrestrial mud volcanoes. Over 18,000 of these mounds have been mapped in the region. They have indications of thermal inertia, as well as spatial densities and diameters consistent with a mud volcano analog. Analysis of CRISM data suggest that the mounds are more oxidized than the plains and this could reflect enhanced alteration within fluid-rich sediments.

Acknowledgments: I would like to thank the Lunar and Planetary Institute and the JSC ARES division for providing me with this opportunity to perform this research and the SETI Institute CRISM team for their support.

References: [1] Farrand, W.H. *et al.* (2005) *JGR*, **110**, E05005, doi:10.1029/2004JE002297. [2] Baker, D.M., Allen, C.C., Oehler, D.Z., 2008. The Global Search for Spring Mounds on Mars and Evidence for Mud Volcanism in Acidalia Planitia. Lunar and Planetary Institute Summer Intern Conference XXIV. [3] Tanaka, K.L., Skinner, J.A., Jr., Hare, T.M, 2005. Geologic Map of the Northern Plains of Mars. Scientific Investigations Map 2888, U.S. Geological Survey. [4] Oehler, D.Z., Allen, C.C., 2009. Mud Volcanoes in the Martian Lowlands: Potential windows to the fluid-rich samples from depth. Lunar and Planetary Science XXXX, Abs. No. 103.

CARBONATE-RICH PHASES OF METEOR CRATER IMPACT MELT PARTICLES.

[1]Denise Anders and [2]David A. Kring, [1]Institute of Geosciences, Christian-Albrechts-University of Kiel, Kiel, Germany (denise.anders@hotmail.de); [2]Lunar and Planetary Institute, Houston, TX 77058 (kring@lpi.usra.edu)

Introduction: Meteor Crater, located on the Colorado Plateau in Arizona, is one of the best preserved impact craters on Earth. Because of its small size, only a small amount of impact melt was generated [1]. Previous studies of melt particles by Hörz et al. [2] found that most of them were produced by melting of sandy dolomite and complete CO_2 degassing to produce vesicular mafic silicate melt. Carbonate phases, however, were recently found coating some of the silicate melt particles [1,3]. It is not yet clear if these are carbonate melts that were quenched before CO_2 could degas or if they are a secondary caliche coating that precipitate on the particles while buried in the ejecta blanket. In the present study, we analyzed the chemical composition and textures of additional samples to further evaluate the origin of these carbonate rinds.

Methods: Thin sections of three particles were examined by petrographic microscopy to identify carbonate and evaluate any textures. Chemical analyses were obtained with a Cameca SX-100 at the NASA Johnson Space Center (JSC). The following conditions and standard sets were used during the measurements (Table 1).

Table 1 Condition and Standards.

	Carbonates	Silicates
Acceleration Voltage	15 KV	15 KV
Beam Current	10 nA	20 nA
Beam Size	10 µm	1 µm
Standards	K411	Olig
	Olig	Diopside
	Rhod	Ort 2
	Ort 1	Apat
	Dolomite	Rhod
	Kaer	Marj
	NiO	Rutile

Additional backscattered-electron (BSE) images to characterize microstructures and textures were made on a JOEL 50 SEM at NASA JSC.

Petrographic description: Sample Hxx15 is an irregular, ~8 x 6 mm silicate melt particle. Like those described by Hörz et al. [2], they are perforated with vesicles and composed of a fine-grained assemblage of skeletal and anhedral olivine and pyroxene. The melt also entrains relict quartz from the target sediments. The anhedral quartz grains show irregular fractions and cracks as a result of impact-induced deformation. Calcite and clay was detected as a fine grained lining of grey-tan color on the interior surface of vesicles. Additional carbonate exists in the form of simple globules consisting of pure calcite. One area of carbonate is zoned with a calcite-rich core and a clay-rich edge around the core and some clay rich particles within the calcite phase (Figure 1). The carbonate-silicate melt contact is sharp. However, there is no carbonate layer on the surface of the particle like that analyzed in previous studies [1,3]. We are not able to determine if this area is included in the melt or if it is a small layer on the surface which was sectioned in an adversed position. The carbonate areas incorporate anhedral quartz, some pyroxene, and iron oxide particles, but no dolomite.

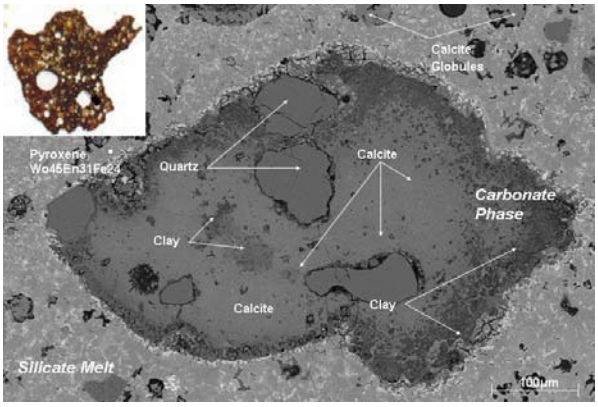

Fig. 1 Sample Hxx15, Irregular formed, zoned carbonate-clay-phase.

Sample Hxx13 (Figure 2) has a size of 6.4 x 5.1 mm and is characterized by a highly vesicular, sometimes frothy melt with skeletal and anhedral olivine and pyroxene. This melt also entrains relict anhedral quartz grains from the target. A 2.4 mm wide edge of the melt particle is coated by carbonate, ultra fine crystals of calcite and a small amount of dolomite (relicts of the target). The

carbonate-silicate melt contact is sharp. The porous texture and the composition of calcite and clay with included quartz grains is similar to the sample described above. The calcite also encloses pyroxene. In addition, the carbonate is present in the melt matrix in the form of homogeneous calcite globules and zoned globules with clay-rich cores and calcite rims.

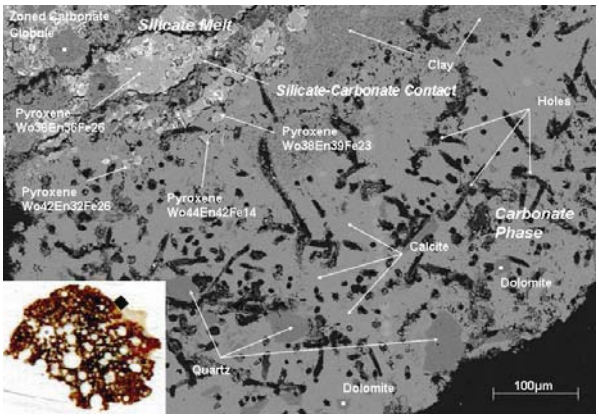

Fig. 2 Porous carbonate layer of sample Hxx-13 including quartz, pyroxene and dolomite.

Sample Hxx11, shown in Figure 3, is sub rounded and has an average diameter of 6mm. This particle is not vesicular, nor does it contain a melt with olivine and pyroxene. Rather, it is composed of quartz grains, showing several deformation structures, embedded in a brown-reddish matrix of iron oxide with traces of SiO_2 up to 10 wt%. Microprobe analyses reveal totals of less than 80wt% confirming the interpretation of hematite, maghemite, or a mix of both. The existence of iron oxide and lack of vesicles indicate the particle is not impact-generated, but was probably a component of the target sediment. However, it was examined because it has a carbonate coating, which might be melt colliding with the particle during the impact process.

Some edges of the particle surface are covered with a fine-grained, white-grey carbonate layer of various lengths, ranging from a width of 2.4 mm to 640 µm. The porous and inhomogeneous bulk mass of carbonate is mainly composed of calcite and clay (Table 2), plus some feldspar, quartz, olivine, pyroxene, and small aggregates of iron oxide. No dolomite was found. The olivine (Fo75Fa25) within the carbonate has a significantly higher proportion of forsterite than the olivine population of the other particles in this project, as well as higher than that in particles examined in Hörz et al [2], which ranges from Fo41 to Fo59. Fractures in the matrix close to the particle surface and within quartz grains contain carbonate phase in the form of pure calcite.

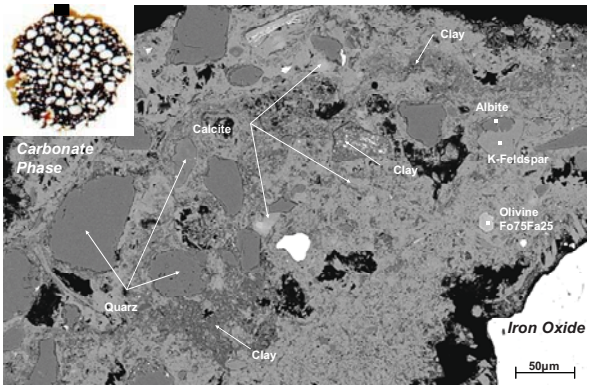

Fig. 3 Sample Hxx-11, Carbonate-clay-layer with embedded quartz and pyroxenes on an iron oxide particle.

Results: Although all analyzed pyroxene crystals in the melt contain a slightly larger wollastonite component than the particles examined by Hörz et al. [2], samples Hxx13 and Hxx15 can definitely be identified as melt particles because of their textures and compositions. In contrast, sample Hxx11 is not a melt particle.

In comparison to previous samples analyzed [1,3], the carbonate zones of the particles described above have different features and textures. No melt fragments were found within the carbonate rinds, there were no distinct transition zones between carbonate layer and underlying vesicular melt, nor was significant dolomite encountered, except for a small amount in sample Hxx13. Hxx15 also lacks a carbonate layer on the surface. Furthermore, Cernok and Kring [1,3] did not describe features like clay containing carbonate and carbonate globules within the silicate melt.

All carbonate zones display similar features, and compositions (Table 2). The phases often looks very porous, altered, and have holes, which may have contained small mineral grains. A possible explanation for the porosity could be, that these minerals dissolved out by weathering (Fig. 2). The origin of the aluminium- and silicate-rich clay in various compositions (Table 2) within every sample is not clear. It might be connected to caliche forming processes.

These similarities indicate that the carbonate zones of all three studied particles have the same origin.

Table 2 Representative compositions of calcite and clay in samples Hxx11, Hxx13 and Hxx15.

	Hxx11	Hxx13	Hxx15
Calcite			
CaO	51.96	51.03	50
MgO	0.34	0.96	1.72
FeO	0.16	0.27	0.23
SiO_2	2.12	0.5	2.07
K_2O	0.13	0.03	0.01
Al_2O_3	0.46	0.13	0.41
Na_2O	0.01	-0.03	0.01
MnO	0	0.08	-0.06
NiO	-0.07	-0.02	0.09
Total (analyzed)	55.18	52.97	54.52
CO_2	41.15	40.19	41.12
Total (calculated)	**96.33**	**94.06**	**95.64**
$CaCO_3$ wt%	92.74	91.08	89.24
$MgCO_3$ wt%	0.71	2.01	3.60
Clay			
CaO	14.85	27.74	10.91
MgO	2.4	8.02	12.81
FeO	3.46	3.03	1.62
SiO_2	38.22	10.36	21.11
K_2O	1.81	0.42	0.03
Al_2O_3	10.34	2.31	3.25
Na_2O	0.15	0.01	-0.02
MnO	0.08	0.03	0.04
NiO	0.04	0.08	0.98
Total (analyzed)	**71.35**	**51.98**	**61.494**

Pyroxene of Hxx13 shows the same compositions as the pyroxenes of silicate melt, which is assumed to have originated from the melt matrix, supported by the fact that the target of Meteor Crater do not consist of pyroxene.

The same applies to sample Hxx11. Because the particle core does not consist of pyroxene, the grains in the rim must be derived from another melt particle. The pyroxenes of sample Hxx15 differ a bit, but still consistent with the type of variation seen by by Hörz et al. [2].

The olivine of Hxx11 (Fo75Fa25) does not correspond to the composition of the olivine in melt particles analyzed in previous studies. However, a relation to impact melt is supposed.

Including pyroxene and olivine grains may probably smashed in the carbonate matrix by collision with melt particles during the impact process but could also be embedded during caliche formation. By reason of the porous texture it is presumed, that originally more grains were included in the phase, which were dissolvated by weathering.

Previous work by [3] found that caliche samples are characterized by a layered texture, consisting of zones of calcite, quartz, and some times phyllosilicates.

None of these mentioned textures appears in the examined carbonate samples. The carbonate does not show layering or any other sorted texture. The mineral grains are not sub rounded, which implies, that no erosion and transport happened. However, the clay amount within the carbonate may be a result of caliche formation.

Conclusions: Based on our investigations regarding texture, structure, and composition of carbonate associated with Meteor Crater impact melt particles, plus previous work, we are presently unable to firmly conclude the origins of all carbonate occurrences. The carbonate areas show features of both caliche and carbonate melt analyzed previous[3].

Acknowledgements: Many thanks to Axel Wittmann and Anne Peslier for their great support with the microprobe. I thank as well George-Ann Robinson for her help on the SEM.

References

[1] Kring D. A. (2007) Guidebook to the Geology of Barringer Meteorite Crater, Arizona (a.k.a. Meteor Crater), *LPI Contribution No. 1355;*

[2] Hörz F. et al. (2002) *Meteoritics and Planetary Science*, 37, p. 501-531;

[3] Cernok A. and Kring D. A. (2009), *LPS XXXX,* Abstract #1825,

Testing EETA79001 Lithology B, a Martian Basalt. S. J. Arauza[1] J.H. Jones[2] L. H. Le[3] and D.W. Mittlefehldt[4], [1] Jackson School of Geosciences, The University of Texas at Austin, 1 University Station C1100, Austin, TX 78712-0254 (arauza@alumni.utexas.edu) [2]Mail Code KR, NASA, Johnson Space Center, 2101 NASA Road 1, Houston, TX 77058, [3]Jacobs Sverdrup Co., Houston, Texas 77058.[4]Mail Code KR, NASA, Johnson Space Center, 2101 NASA Road 1, Houston, TX 77058.

Introduction: EETA79001 is a member of the SNC (shergottite, nakhlite, chassignite) group of Martian meteorites. Most SNC meteorites are cumulates or partial cumulates [1] inhibiting calculation of parent magma compositions; only two (QUE94201 and Y-980459) have been previously identified as true melt compositions. The goal of this study is to experimentally determine if EETA79001-B could also represent true equilibrium melt composition, which would allow for direct determination of parent magma compositions and enable further constraint of mantle conditions on Mars. This study will provide further evidence for or against the use of EETA79001-B to constrain parent magma compositions.

EETA79001 is a large stony meteorite featuring two distinct basaltic lithologies (A & B) joined along a planar igneous contact. Both lithologies are dominantly comprised of pigeonite and augite with maskelynite, a shocked form of plagioclase [2]. These phases comprise the bulk of lithology B and the groundmass of Lithology A. Lithology A features megacrysts of olivine, orthopyroxene, and chromite in a fine-grained groundmass while Lithology B is coarse-grained and non-porphyritic. The presence of two distinctly different basaltic lithologies joined along a planar igneous contact makes EETA79001 a very unique member of the SNC group.

Table 1: Comparison of Lithology B starting composition [4], EETA79001-B, melt analyses of Experiments 18 (1120 °C) & 19 (1110 °C), and melt from a Shergotty experiment (1108 °C) [5].

	Start Comp.	Lith. B	LithB-18	LithB-19	Sh-10
SiO2	49.83	49.38	50.01	51.30	49.90
TiO2	1.39	1.38	1.42	1.49	1.21
Al2O3	12.55	12.44	11.37	11.15	10.80
Cr2O3	0.00	0.00	x	x	0.02
FeO	17.30	17.14	17.41	17.33	19.20
MnO	0.41	0.41	0.42	0.41	0.44
MgO	5.31	5.26	5.16	4.26	4.17
CaO	10.85	10.75	10.69	10.07	9.60
Na2O	1.91	1.89	1.81	1.70	2.08
K2O	0.08	0.08	0.08	0.10	0.28
P2O3	1.30	1.29	1.25	1.23	x
Total	100.91	100.0	99.63	99.05	97.70

Competing models for the origin of EETA79001 call for successive lava flows [2] or significant impact melting [3].

Experimental Methods: Sample charges were prepared using a glass powder of Lithology B bulk composition from [4] processed into a paste and mounted on a loop of Re wire (with Pt wire for drop quenched experiments). Samples were melted for four hours at 1175 °C, and then dropped to either 1110 or 1120 °C for 2 to 7 days in DelTec furnaces at 1 bar. Oxygen fugacity was set to QFM-2 and controlled by a CO/CO2 gas mixture, monitored by a zirconia cell in a designated reference furnace. Quench temperatures were monitored using a Type B (Pt6Rh, Pt30Rh) thermocouple calibrated to the melting point of gold (1064 °C). Samples were then either drop quenched into water or air quenched. Experiments are summarized in Table 2.

The narrow temperature range was chosen based on previous experiments: no crystals were present at 1130 °C (experiment 11) and the presence of olivine at 1110 °C discouraged any lower-temperature experiments. Experiments were run at atmospheric pressure (1 bar) because it is assumed that EETA79001 must have formed near the surface of the parent body in order to have been ejected by meteorite impact.

Table 2: Lithology B experimental conditions.

Exp.	Melt T (°C)	Quench T (°C)	Time (days)	Phases
11	1300	1131	2	none
16	1175	1120	2	plag, aug
17	1175	1110	2	plag, aug, olv
18	1175	1120	7	plag, aug
19	1175	1110	7	plag, aug, olv

Analytical Methods: Resulting glasses and phases were analyzed using the Cameca SX100 electron microprobe at NASA JSC. Calibration and analyses were run with a current of 20 nA and a voltage of 15 kV. Quenched glasses were analyzed using a 5 μm beam while 1 μm spot analyses were performed on plagioclase, augite, and olivine cores. All materials were analyzed for Ti, Fe, Mg, Mn, Ca, Na, Si, and P interpreted as oxides. Analyses of pyroxene and pla-

gioclase were used to compare experimental phases to the natural sample.

Electron microprobe analyses from [5] and [6] were used to construct a phase diagram for SNC meteorites (Fig. 1). Analyses of melts from Shergotty, Zagami, and synthetic EETA79001-A define a cotectic for pigeonite/augite, and a peritectic for low-Ca pyroxene/olivine. The proximity of the lithology B bulk composition (and Shergotty 10 from [5]) to the intersection of these lines is suggestive of an equilibrium melt composition.

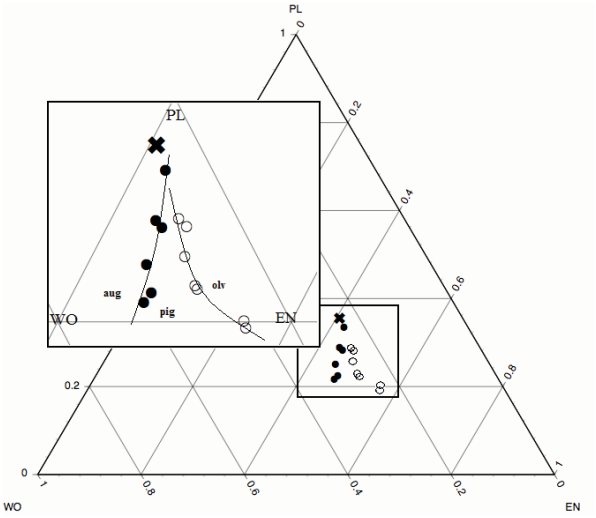

Figure 1: Martian meteorite phase diagram. Pigeonite-augite cotectic defined by data from [5] and Low-Ca pyroxene-olivine peritectic defined by Lith. A experiments from [6]. Starting composition X from [4] plots close to the intersection of these points, which is suggestive of a melt composition.

Results: Two successful 1120 °C crystallization experiments yielded augite and plagioclase with quenched glass (melt). At 1110 °C olivine was also present, which is not found in EETA79001-B.

Pyroxene: Experiments 17, 18, and 19 feature medium-sized (~300 μm), subhedral pyroxene grains growing between euhedral plagioclase crystals. Experiment 16 has smaller, more numerous pyroxenes. Electron microprobe data from [5] were used to construct a pyroxene quadrilateral (Fig. 2). Pyroxenes from these experiments cluster around the augite side of the pyroxene solvus. Chemical analysis of augite cores from previous analysis by Dr. David W. Mittlefehldt of EETA79001 are in agreement with our pyroxenes, though the initial description of the natural sample by [2] features both augite and pigeonite. Crystallization experiments lacked pigeonite.

Plagioclase: In three of the four experiments, plagioclase occurs in large (500-700 μm) twinned crystals with distinct euhedral and skeletal populations. Euhedral plagioclase crystals are often enveloped by augite and olivine (Fig. 3). Experiment 16, however, features the opposite relationship as augite grains have been enveloped by large, blocky plagioclase crystals (Fig. 4). This observation is consistent with the natural sample, which features maskelynite (shocked plagioclase) grains in the interstices between clinopyroxenes [2]. Chemical analyses of plagioclase cores (An61-An70) are in agreement with chemical analyses of maskelynite cores from [2] (An62).

Melt: Melt analyses from crystallization experiments cluster near the lowest-temperature melting point defined by data from [5] and [6].

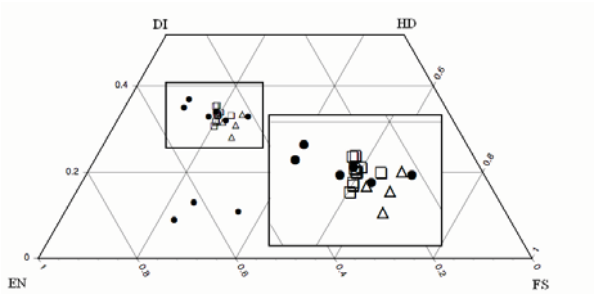

Figure 2: Pyroxene compositions from [5] (filled circles), EETA79001-B analysis from Mittlefehldt (open squares), and crystallization experiments from this study (open triangles). Experiments from this study crystallized augite exclusively, though EETA79001-B features both phases.

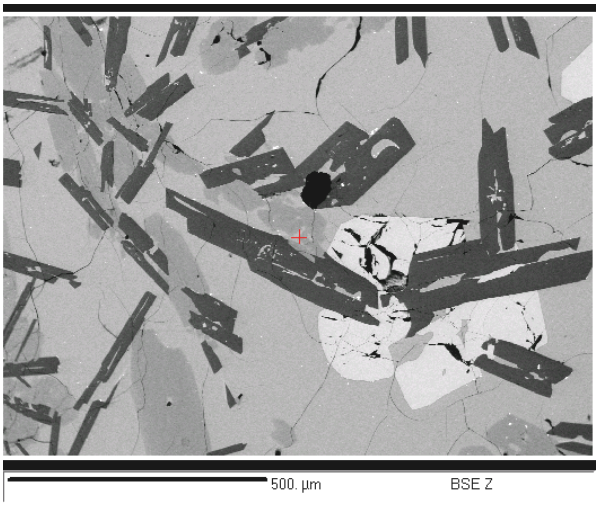

Figure 3: Backscatter electron image of experiment 19. This image features large plagioclase crystals (dark) enveloped by augite (gray) and olivine (lightest). This relationship is different from the relationship observed in the natural sample [2]. Olivine is not present in EETA79001-B.

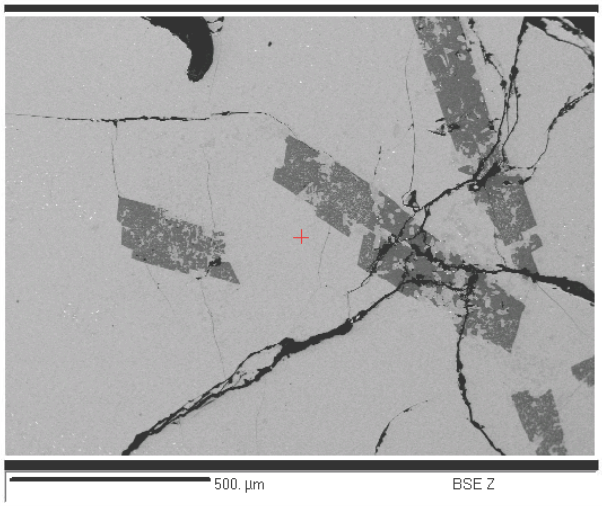

Figure 4: Backscatter electron image of experiment 16 illustrating relationship between plag (dark crystals), aug (light colored inclusions), and melt. The plagioclase crystals overgrow and envelop the pyroxenes, which is similar to the relationship between maskelynite and pyroxenes in the natural sample [2].

Olivine: At 1110 °C olivine appears in crystallization experiments. These crystals are also moderately-sized (~300 µm) and grow in the interstices between larger plagioclase grains. Olivine composition ranges from Fo75.7 to Fo79.5. Olivine is not found in EETA79001-B.

Discussion: The initial plot of Lithology B melt compositions versus pigeonite-augite and pyroxene-olivine phase boundaries suggested that Lithology B may represent a true equilibrium melt composition. In addition, Lithology B resembles a partial melt of Shergotty Sh-10 [5]. That our bulk composition plots close to the low-temperature melting point for these phases under these conditions is a strong argument for a melt composition, but textural and chemical analyses indicate otherwise.

The majority of the crystallization experiments from this study feature textural differences from descriptions of EETA79001-B in the literature. The most striking of these differences is the disparity in the apparent order of crystallization. McSween and Jarosewich document plagioclase crystals growing in the interstices of pyroxenes in EETA79001-B [2], this is consistent with the common interpretation that pyroxene crystallizes before plagioclase in EETA79001-B as well as Shergotty and Zagami [5]. Phase relationships in experimental charges are reversed, with plagioclase overgrown by augite (except in experiment 16), although the order of crystallization of the two phases cannot be determined by this study.

Chemically, experimental phases differ from naturally occurring phases to varying degrees. Plagioclase crystals from these experiments are in agreement with maskelynite core analyses from [2]. Modal percentages of pigeonite and augite differ greatly for the experiments and the natural sample. Pigeonite dominates EETA79001-B according to [2], but was absent from crystallization experiments in this study.

The largest discrepancy between these experiments and the natural sample is the presence of olivine in lower-temperature experiments. The bulk lithology from [4] was chosen over other possible starting compositions because it is the least magnesian option, and therefore least likely to crystallize olivine. The fact that olivine was able to crystallize so readily from this composition indicates that this composition cannot exist as a melt in nature without crystallizing olivine. EETA79001-B shares this bulk composition but lacks olivine and, therefore, could not be a true melt composition.

Another possible explanation for the presence of olivine in experiments 17 and 19 are the use of the wrong starting composition. In our case, the starting composition was specifically chosen to diminish the likelihood of crystallizing olivine, reinforcing the conclusion that this composition cannot exist as a melt in nature without olivine. The persistence of olivine crystals through two experiments of varying duration demonstrates the reproducibility of olivine crystallization.

Conclusions: Results from the crystallization experiments demonstrate that EETA79001-B does not represent a true equilibrium bulk composition. The presence of olivine in the experiments implies that the bulk composition of Lithology B cannot exist in equilibrium conditions at this pressure and temperature without crystallizing olivine, which is not found in the natural sample. Additionally, the presence of pigeonite in EETA79001-B was not successfully reproduced in crystallization experiments. Unfortunately, because Lithology B isn't a true melt, it cannot be used directly to define conditions of the parent material or Martian magmatic conditions. It is beyond the scope of this study to construct a model for the origin of EETA79001-B that would explain the absence of olivine and the crystallization of pigeonite.

References: [1] Longhi J. and Pan V. (1989) *LPS XIX,* 451-464. [2] McSween H. Y. and Jarosewich E. (1983) *Geochimica et Cosmochimica Acta, 47,* 1501-1513. [3] Mittlefehldt et al. (1999) *Meteoritics & Planet. Sci., 34,*357-367. [4] Warren P. and Kallemeyn G. (1997) *Antarctic Meteorite Research, 10,* 61-81. [5] Stolper E. M. and McSween H.Y. (1979) *Geochimica et Cosmochimica Acta, 43,* 1475-1498. [6] Wasylenki L. et al. (1993) *LPSC XXIV*, Abstract #1491.

AUTOMATED CLASSIFICATION OF THE JSC COSMIC DUST CATALOG VOLUME 15. S. W. Bell,[1] J. Lasue,[2] and T. Stepinski.[2] [1]Amherst College, Amherst, MA 01002 (swbell11@amherst.edu), [2]Lunar and Planetary Institute, Houston, TX 77058 (lasue@lpi.usra.edu, tstepinski@lpi.usra.edu).

Introduction: Over the past several decades, NASA has been able to collect thousands of Interplanetary Dust Particles (IDPs) from the stratosphere using high-flying aircraft. Unfortunately, even in the high atmosphere there is a large number of particles of a terrestrial origin, either from natural sources such as volcanoes or from artificial sources such as rocket fuel. To distinguish the origins of the particles, NASA's Johnson Space Center (JSC) defined a preliminary classification system and published the results in the multi-volume "Cosmic Dust Catalog." [1] Each page of the catalog contains a scanning electron microscope (SEM) image of the particle, an Electron Dispersive Spectroscopy (EDS) spectrum, and a number of descriptors, including size, shape, transparency, color, luster, and probable origin. There were seven origin classifications: C (cosmic), C? (probably C), TCN (natural terrestrial contaminant), TCN? (probably TCN), TCA (artificial terrestrial contaminant), TCA? (probably TCA), and AOS (aluminum oxide sphere) [1]. This classification system used several criteria to assess origin: The main indicators of cosmic origin used were similar compositions to meteorite bulk compositions and evidence of atmospheric entry heating (partial melting and the existence of a black fusion crust). The main indicator of terrestrial origin was the existence of significant amounts of cadmium, lead, potassium, sodium, or chlorine. Particles were also classified as terrestrial contaminants if they exhibited any number of unusual EDS bulk compositions, such as pure Si or pure Al [1].

Further subcategories of the C particles were defined in additional works [2,3]: the chrondritic particles and the Fe-Ni-S particles. The chrondritic particles do not actually contain miniature chrondules, but their bulk chemical abundances are very similar to abundances in chrondritic meteorites.

High noble gas content from prolonged exposure to solar wind is a strong indicator of cosmic origin, and subsequent studies with destructive noble gas content analyses in general confirmed that the particles that JSC classified as C were indeed C [4]. However, new results from the Stardust mission, which collected IDPs from the tail of comet Wild 2, indicate that a significant fraction of the particles previously classified as terrestrial contaminants may actually be of cosmic origin [5].

To improve the classification system, we applied data mining techniques to cluster the EDS spectra of the 464 particles in Volume 15 (the largest volume) of the IDP Catalog into groups of similar particles.

Methods: Unfortunately, the digital versions of the original EDS spectra were unavailable, so it was necessary to redigitize the spectra from PDF scans of the actual pages of the catalog. Due to the large number of spectra to be digitized, we built a semi-automated digitization algorithm.

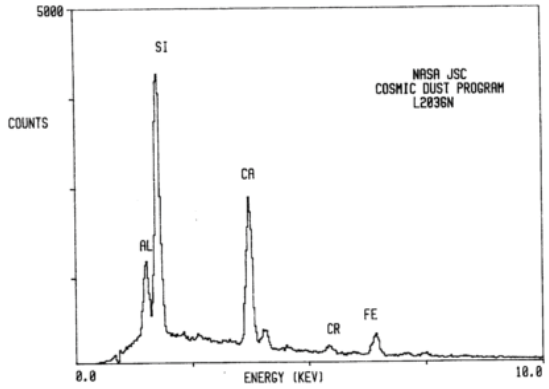

Figure 1: A sample EDS spectrum image for digitization.

Our first step was to read the maximum value on the count axis with a simple optical character recognition algorithm. We assembled a list of standard images of the ten numerals, compared the image of each numeral to be read to each of the standard images, and chose the value of the most similar standard numeral to be the value of the numeral being read. We then separated the image into connected components and extracted the component representing the graph and frame.

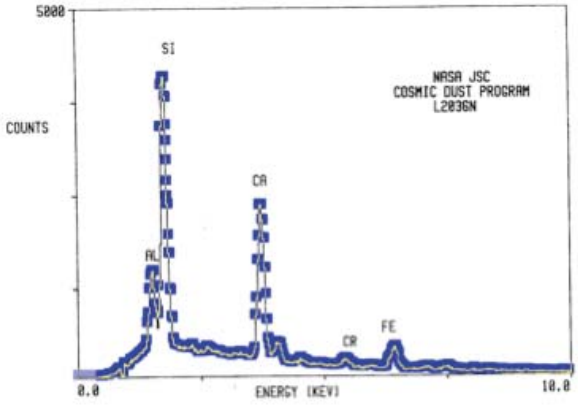

Figure 2: A false color image showing the original graph in yellow and black and the points in the new digitization as blue boxes.

After using the frame to find the locations of the axes and determine the scale of the image, we removed the top and side axes and retrieved the maximum value in each column. These values were then scaled and recorded as the count values for the appropriate energy level. Several issues, such as letters "sticking" to the curve (see Fig. 1) or chunks of the curve missing, simply had to be dealt with manually. However, we succeeded in digitizing the EDS spectra of all 464 particles in Volume 15 and the spectra of the four standards (Allende Bulk Powder, Diopside, Kakanui Hornblende, and San Carlos Olivine) [1] (see Fig. 2).

Because not all of the images had the same width along the energy axis, the digitized spectra were of differing lengths and needed to be rescaled. We used linear interpolation to regenerate each spectrum with 1522 energy values. This allowed us to take each energy channel as a dimension and the corresponding count value as the value in that dimension and consider the spectra as vectors in a 1522-dimensional space. We then used the built-in Agglomerate[] and ClusterSplit[] functions in *Mathematica* to identify clusters of spectra that were close together (in ordinary Euclidean distance). The number of clusters was chosen to best represent a balance between identifying meaningful clusters and keeping large clusters of similar particles together.

To assess how pure the clusters were with respect to the JSC classification labels, we used a standard data mining measure called "entropy." The entropy E_c of a cluster c is calculated by first finding n_{lc}, the number of particles of a particular label l in cluster c, and N_c, the total number of particles in the cluster, and then using Equation (1), where the summation is over all labels found in that particular cluster.

$$E_c = -\sum_l \frac{n_{lc}}{N_c} \log_2 \left(\frac{n_{lc}}{N_c} \right). \quad (1)$$

After we assembled the clusters, we added the standard spectra to the classification scheme by placing each standard in the cluster belonging to the particle nearest to it in the multidimensional space.

To help visualize these clusters, we used a visualization algorithm known as Sammon's Map [6] Sammon's Map is an iterative algorithm that begins with an initial guess two-dimensional plot of multidimensional vectors and rearranges the two-dimensional points so that their interpoint distances better reflect the multidimensional points' interpoint distances. We ran the algorithm for 600 iterations (see Fig. 3 for the results).

Cluster	Type	All	Entropy	C	C?	TCN	TCN?	TCA	TCA?	AOS
1	Chrondritic	69	0.889304	57	7	4	1	0	0	0
2	Chrondritic	27	0	27	0	0	0	0	0	0
3	High Ca	36	2.22924	4	4	15	5	7	1	0
4	Al Si	8	1.75	0	1	4	2	1	0	0
5	High Si	20	0	0	0	20	0	0	0	0
6	Chrondritic	40	1.14989	29	8	2	1	0	0	0
7	Mg Si	30	1.93291	8	10	8	4	0	0	0
8	Low Z	60	1.64326	0	1	26	6	25	2	0
9	Misfits	8	1.40564	0	1	4	0	3	0	0
10	High Cd	20	0	0	0	0	0	20	0	0
11	High Al	21	1.41121	0	1	2	1	15	0	2
12	High Al with S	16	1.0141	0	0	1	3	12	0	0
13	Fe Ni S	27	2.0053	12	5	5	1	4	0	0
14	Fe Ni	27	1.03777	19	7	0	0	1	0	0
15	Pure Al	49	0.888647	0	0	0	0	34	0	15
16	Pure Al	6	0	0	0	0	0	0	0	6
Totals		464	1.16596	156	45	91	24	122	3	23

Table 1: A table showing the clusters and their composition.

Results: We obtained sixteen clusters (see Tab. 1). The IDPs in Clusters 1, 2, and 6 mostly appeared to belong to the chrondritic subclassification. They tended to show strong Si peaks and intermediate amounts of Mg, S, and Fe. The Allende bulk composition powder was placed in Cluster 1 and the San Carlos Olivine was placed in Cluster 6. Cluster 3 consisted of Si-rich particles with high Ca. Most likely due to their high Ca content, the diopside and Kakanui hornblende standards were placed in Cluster 3. Cluster 4 consisted of particles that were mainly composed of Al and Si. Cluster 5 was composed of very-high Si content particles. Cluster 7 contained Mg-rich Si particles. Notably, all Cluster 7 particles were low in S. Cluster 8 contained particles with a high proportion of elements with an atomic number below 10, the "low-Z" particles. They contained a range of detectable element compositions, but they all contained the broad background peak associated with the low-Z elements. Cluster 9 was a diverse collection of eight particles that did not fit well into any of the other clusters. Cluster 10 contained high-Cd particles. Clusters 11 and 12 consisted of Al-rich particles with small amounts of minor elements. Cluster 12 was distinguished from Cluster 11 by larger S contents. Clusters 13 and 14 both contained high-Fe particles, some of which contained significant amounts of Si and Ni, although Cluster 14 had much higher occurrences of S. Clusters 15 and 16 consisted of pure Al particles. They were all classified as artificial terrestrial contaminants or AOS. Of the 55 particles in Clusters 15 and 16, JSC classified 21 as AOS. Twenty of the particles classified as AOS were spherical in shape. However, L2021F14 was irregular and L2036F15 was not classified as AOS but did have a spherical shape.

The Sammon's Map shows a clear rift (along the dotted line in Fig. 2) between the primarily cosmic particles on the right and the terrestrial contaminants on the left. The high-Al particles stream off in a bulge in the upper left, with the Al oxide spheres in the far upper left hand corner.

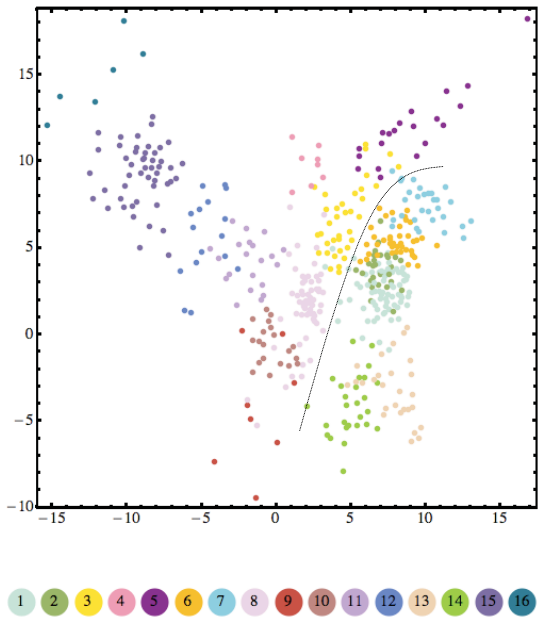

Figure 3: The Sammon's Map visualization of the color-coded clusters. The dashed line separates the contaminant particles on the left from the cosmic particles on the right.

The chrondritic particles group together, as do the high-Fe particles. At the top of the cosmic region are the Mg-Si particles, following the general trend of higher Mg/Fe ratios higher in the cosmic region.

Discussion: The homogeneity of our clusters with respect to the JSC classifications provided a fairly strong validation of both our clustering method and the JSC classification. The grouping on the Sammon's Map into cosmic and terrestrial contaminant particles as well as the grouping of cosmic clusters into chrondritic and high-Fe groups also validated the method. Further validation of the method was obtained by classifying the standard spectra into appropriate clusters. This is a significant result because it shows that this method can be used to generate a good classification without individually inspecting each spectrum manually and without human bias. The spectra can simply be placed into the preexisting clusters.

The close grouping on the Sammon's Map of particles classified by JSC as cosmic also emphasizes the fact that the range of particles classified as cosmic is much narrower than the range of particles classified as terrestrial contaminants. This is most likely due to the fact that all particles classified as cosmic share the essential characteristics of being mafic, Al-poor, and usually S-rich.

Based on our clustering, we identified a number of particles identified as terrestrial contaminants that were clustered in primarily cosmic clusters, indicating that they may actually be of cosmic origin. Since it has been primarily the IDPs classified as cosmic by JSC that have been subjected to destructive analyses, most likely these particles are still kept intact at JSC. We plan to investigate these particles further in hopes of providing more classified and catalogued particles.

From Cluster 7, we also have isolated a group of IDPs that appear significantly distinct from the chrondritic and Fe-Ni-S particles, the Mg-Si particles. Although results from particles identified as C in 1992 describe the ranges of pyroxene and olivine compositions in IDPs as $En_{57\text{-}100}$ and $Fo_{44\text{-}100}$ continua and note that some particles have restricted compositions of $En_{91\text{-}100}$ and $Fo_{90\text{-}100}$ [7], these particles were largely not classified as C in early classifications. However, similar compositions were detected in comet Hale-Bopp during its 1994 approach [8]. Although Stardust results show that pristine Wild 2 dust has a broad range of low-Ca pyroxene compositions ($Fs_{0\text{-}48}$), in keeping with cosmic IDP abundances, it also shows a frequency peak at Fs_5 [9]. Due to these results, we believe that it is probable that many of these particles had been classified as contaminants prior to the Hale Bopp and Wild 2 results but now could be confidently classified as cosmic. This is particularly noteworthy because significant evidence suggests that these particles may represent presolar grains [8], which is consistent with finding stronger evidence for these particles in an Oort Cloud comet like Hale-Bopp than in a Kuiper Belt comet like Wild 2.

Conclusion: Our clustering results have demonstrated the viability of a new technique for IDP classification that involves no human bias. We have succeeded in assembling the largest existing digital catalog of JSC-classified IDP spectra. We have confirmed the overall validity of the JSC classification. We are able to distinguish not only between cosmic particles and terrestrial contaminants, but also between the most important subgroups of both types. This has enabled us to identify a list of particles that may have been misclassified. Finally, this technique will be useful in classifying Stardust particles.

Acknowledgements: We would like to thank M. Zolensky for his assistance in understanding the catalog and fruitful discussion of our results. We would also like to thank the LPI internship program for making this project possible.

References: [1] Clanton, U. S. et al. (Vol. 1, 1982), Warren J. L. et al. (Vol. 15, 1997). *Cosmic Dust Catalog*. [2] MacKinnon I. et al. (1982) *JGR*, 87, A413-A421. [3] Rietmeijer F. Ch. 2 in Papike J. J. *Planetary Materials* (1998). [4] Kehm k. et al. (2002) *Meteoritics & Planet. Sci.,* 37, 1323-1335. [5] Joswiak D. J. et al. (2008) *LPS XXXIX*, Abstract # 2177. [6] Sammon J. W. *IEEE Transactions on Computers*, (1969). [7] Zolensky M. and Barrett R. (1992) *Meteoritics*, 27, 312. [8] Wooden et al. (2000) *Icarus*, 143, 126–137. [9] Zolensky M. et al. (2008) *Meteoritics & Planet. Sci.,* 43, 261-272.

VENUSIAN VOLCANOES AND THE INTERNAL THERMAL STATE OF VENUS. J. Buz[1] and P. McGovern[2], [1]Massachusetts Institute of Technology Department of Earth, Atmospheric, and Planetary Sciences (jbuz@mit.edu), [2]Lunar and Planetary Institute (mcgovern@lpi.usra.edu).

Introduction: Radar imaging and topography data from the Magellan mission to Venus revealed over 150 volcanic edifices with diameters in excess of 100 km [1,2,3]. Most of these edifices exhibit conical or domical topographic profiles, with a surrounding apron of lava flows on very low slopes. However, several volcanic constructs comprise an annular ridge and lava apron, falling into the morphological category "corona" [e.g., 4,5]. Recently, a link has been proposed between volcanic edifice shape and the thickness of the elastic lithosphere (T_e), based on the predicted effects of lithospheric stress on magma ascent [6,7]. Such a link could allow us to place constraints on the thermal evolution of regions on Venus based on the presence of certain edifice shapes and their stratigraphic relations.

Using Magellan radar backscatter images and topography data, we have analyzed the slopes of the edifices and the flow lengths of known volcanoes in the northern hemisphere to isolate the shape characteristics of volcanoes. These constraints can be used for automated detection of class (conical, domical, or annular) based on topographic data. Furthermore, we have used a model for volcano growth that links magma ascent with lithospheric flexural stresses, to create a suite of potential volcanoes influenced by magma source dimensions and supply rate, and T_e. After least squares fitting of model volcano topography with actual volcano topography, a set of parameters are inferred for each volcano. This allows for local determination of T_e, which can be applied to infer variations in thermal history over larger regions of Venus.

Data: We have been using radar backscatter images and topographic data of Venus acquired by Magellan in the 1980s and made available by the USGS online [8]. We have done an analysis on all of the volcanoes in the northern hemisphere . However, some volcanoes had incomplete topographic data and therefore could not be used. We have done some analysis of the flow lengths using USGS maps of Venus prepared from the same Magellan data. In addition to the raw topography data we are also using topography filtered by best-fit planes along 40- and 80-km baselines. These filters help to attenuate asymmetries and anomalous highs on or around the edifices.

Methods: We model volcano growth in a self-consistent manner, calculating the interaction of the lithospheric stress state and magma ascent. In each model, a characteristic magma source radius (r_m) and central height (h_m) are defined, assuming a conical magma distribution in axisymmetric geometry. This magma distribution is subdivided into a number n_{inc} of equal height increments (values adopted: 1, 5, 10, and 20). The n_{inc} parameter reflects a relationship between the magma supply rate and the characteristic flexural response time of the mantle asthenosphere, or Maxwell time τ_M. High n_{inc} corresponds to relatively low magma supply rate and vice versa. For a given stress state, magma ascent at a given location depends on two criteria [6]: favorable horizontal normal stress orientations (horizontal extension [9]) and gradients (extension increasing upward [10]). Our model evaluates these criteria as functions of radius r at a discrete set of points. At points where both ascent criteria are satisfied, the magma height for the current increment is added to the surface load; at points where one or both criteria are violated, the magma is diverted to the closest point where ascent is allowed, and distributed to adjacent points within a characteristic width (here taken to be 25 km). The new load distribution is then applied to the lithosphere, a new stress state calculated, and the cycle is repeated n_{inc} times

We relate the topography of the model edifices to those of actual volcanoes on Venus via least-squares fitting. Although fitting of the entire set of topography and slope data is the most robust, it also includes many unnecessary irregularities. We average a volcano's topography in annular bins to create a smoothed radial topography profile. For each volcano with complete topography data, we cycle through all possible model volcanoes and do a least squares fit of the model volcano's profile with the actual volcano's profile. We reduce the topographic data for the volcano and model to only include 1.5x the edifice radius. Then, those model volcanoes whose topographic and slope profiles have the lowest least squares fit error with the actual volcano data are taken to be the best model to describe the volcano. A best fit is determined for raw Magellan topography and for slopes filtered by best-fit planes along 40- and 80-km baselines. The best case scenario is when all three analyses (topography, 40km filtered slope, and 80km filtered slope) return the same model volcano as the fit with the least squares error, though this is not often the case. Where two analyses return the same model is also favorable. If all three analyses return different best fit models, the information about the slope and/or the topography is still usable as long as all three best fit models are of the same shape of edifice.

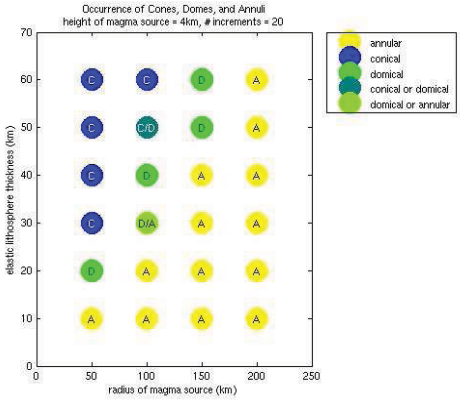

Figure 1
Distribution of conical (C, blue), domical (D, green), and annular (A, yellow) edifices as functions of magma source radius r_m and lithospheric thickness T_e.

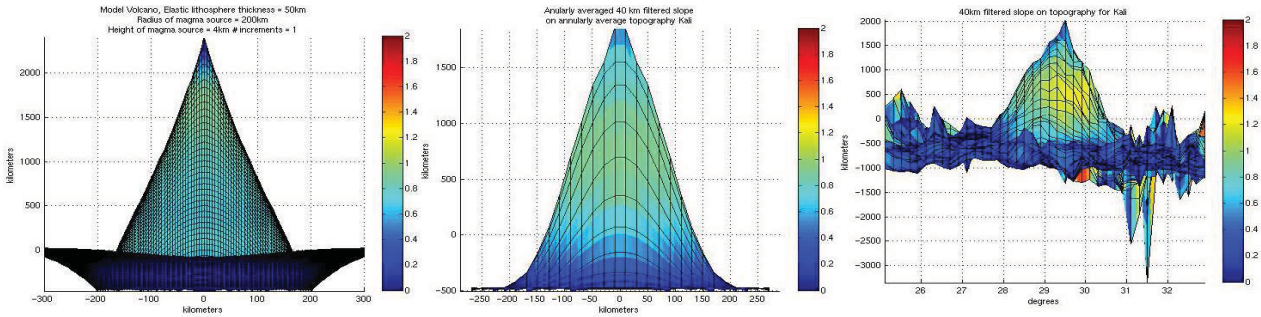

Figure 2. 3-D representations of slope (colorscale) draped over topography (vertical relief) for (a) best-fit model; (b) annularly averaged edifice, and (c) actual edifice, for Kali Mons.

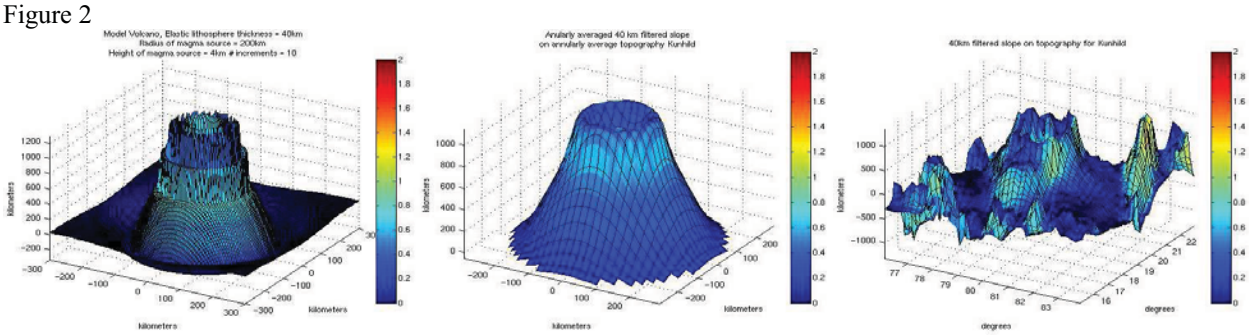

Figure 3. Same as Figure 2, for Kunhild Mons. (Note the colorscales are equivalent in Figs. 2 and 3).

A less robust way to find a good match between the real volcanoes and the model volcanoes is by using the maximum slope and radius of the maximum slope of the annularly averaged topography on the edifice. Using the dataset of annularly averaged slopes, the values are sorted and indexed. The maximum slope and its location are noted and compared. Though the model volcanoes found using this method might not be the best match as deteremined by the least squares fit of the entire topography, the model volcanoes returned usually have the same edifice shape as the actual volcanoes.

Results: A few trends in volcano evolution have been observed. Figure 1 shows variations of final edifice shape as functions of the parameters that appear to exert the strongest effects on edifice shape: elastic lithospheric thickness T_e and magma source radius r_m. In general, lower values of T_e and higher values of r_m favor the generation of annular volcanoes. Cones are found mostly at the lowest value of r_m shown, except at the highest T_e value. Domical shapes are found in a narrow stretch of parameter space between conical and annular regions. Low values of magma source central height h_m and number of increments n_{inc} favors formation of conical edifices; increasing these parameters tends to lead to more domical and then annular edifices. The evolution of individual edifices over many load increments shows that many eventually non-conical edifices have conical shapes in their early stages; at some point, high adverse stresses and stress gradients in the central regions shutoff magma ascent there, leading to favored lava emplacement on the mid flanks. This cutoff causes a transition to domical edifices at first, then annular if the process continues.

Figures 2 and 3 show the best fit model volcanoes for the actual volcano Kali Mons (9.4N 29.75E) and Kunhild Mons (19.3N 80.1E), respectively. The left most images are the model volcanoes best fit for topography and slope, the middle images are the annularly averaged topography for Kali Mons with the colors representing the annularly averaged slope data. The right most imagse are the 40km filtered slope of Kali Mons over the actual topography. The models provides satisfactory fits to the height, width, shape, and slope data for Kali and Kunhild Mons. We conclude that Kali Mons was emplaced on a thick lithosphere (T_e = 50 km), the volume of the magma source was relatively large (r_m = 200km, h_m = 4km), and took place relatively quickly with respect to flexural response (n_{inc} = 1). Kunhild Mons was emplaced on a slightly thinner lithosphere (T_e = 40 km), with an equally large magma source (r_m = 200km, h_m = 4km), but took place over a longer amount of time (n_{inc} = 10).

Discussion: We suggest that the diversity of volcanic edifice shapes on Venus is due to changing stress conditions which cut off magma ascent. Annular edifices arise from weak or thin lithospheres, long emplacement times (coupled with more increments of magma emplacement), and larger magma source widths. Flexural rigidity is proportional to T_e to the third power, for this reason small increases in T_e help to maintain conical edifices. Additionally if the radius of the magma source is large compared to the flexural wavelength of the lithosphere, it is easier for stress to build up in the center. Thus, broader loads (or, magma sources) are more likely to form corona-like structures at a given T_e, as previously predicted [3]. The lithosphere deforms more readily as the radius of the magma source increases and therefore generates more stress for a given amount of magma. The shape of the magma source is conical, hence, the greatest stress state is in the center of the edifice where the most magma is emplaced.

Central ascent cutoff is what drives magma ascent to the outside of the edifice forming domes and eventually annuli (coronae). We speculate that if the center of coronae were to be excavated, instead of finding the remnants of a magma chamber which has been caved in, we would find broad but vertically narrow intrusions: sills. These sills represent the lateral movement of the magma, which when cut off due to high stresses moves to the sides until it reaches an area where ascent is possible. The low number of increments more often yields conical edifices because of a delayed response time of the lithosphere to the stresses. The lithosphere might not be able to flex in the amount of time a few lava eruptions take place, therefore those eruptions are essentially taking place on a straight flat rigid lithosphere. Nijole Mons (44.75N 184.8E) in figure 4 demonstrates this strongly. It is relatively steep-sided and domical/conical, surrounding it is a sort of flexural moat. The lava flows observed in the radar backscatter images show what appear to be lava flows traversing upslope. Our intuition tells us that these topographic rises must post date the flows. Therefore, the volcano (flexurally) subsided after the lavas were erupted.

A look at the regional distribution of domes, cones, and annuli in the northern hemisphere of Venus gives hints as to the regional thickness of the lithosphere. The northern Atla region is remarkably volcanically active, with a even distribution of domes and cones. Based on our results for the requirements for these shapes of edifices we can conclude that this region has either a thick, strong lithosphere or that the volcanoes in this region have a faster supply rate than in other regions. We favor the former hypothesis because of the lack of compressional faults observed. If the volcano was erupted onto the surface in a time shorter than the Maxwell time, and afterwards the lithosphere flexed, there would be more faults than if it were a gradual process [e.g., 11]. The eastern Eistla region contains many domes and annuli. We conclude here that the lithosphere must be thinner, the magma eruption rate must be lower, or both.

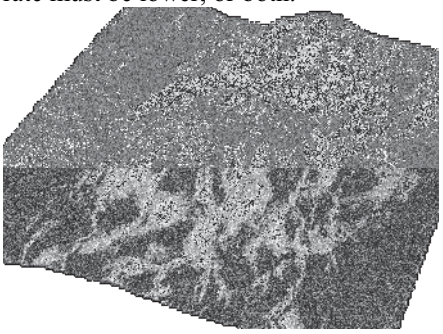

Figure 4
3-D radar backscatter image of Nijole Mons overlayed on topography. Note the flows on the left, right, and upper parts of the image are uphill. Nijole is sitting in a flexural moat.

References:

[1] Head et al., *JGR, 97*, 13, 153, 1992; [2] Crumpler L.S. et al. (1997). *Venus II*, 697–756. [3] P. McGovern and S.C. Solomon (1998) *JGR, 103,* 11,071–11,101. [4] E. R. Stofan et al. (1992), *JGR*, 97, 13,347 [5] S. E. Smrekar and E. R. Stofan (1997) , *Science, 277*, 1289. [6] M.E. Rumpf and P. Mcgovern (2007) *LPSC XXXVIII* [7] P. McGovern and M.E. Rumpf (2007) *Lunar Planet. Sci., 38*, 2387. [8]] USGS: *Map-a-Planet*, http://pdsmaps.wr.usgs.gov/; [9] E. M. Anderson (1936) *Proc. R. Soc. Edinburgh, 56*, 128. [10] A. M. Rubin (1995) *Annu. Rev. Earth Planet. Sci., 23*, 287. [11] P. McGovern and Solomon (1993) *JGR, 98,* 23,553-23,579

Determining the metal/silicate partition coefficient of Germanium: Implications for core and mantle differentiation C. King[1, 2], K. Righter[3], L. Danielson[3], K. Pando[3], C. Lee[4] [1]Department of Geosciences, University of Arizona, Tucson, AZ, 85721 [2]Lunar and Planetary Institute, Houston, TX, 77058 [3]Johnson Space Center, Houston, TX, 77058 [4]Department of Earth Science, Rice University, Houston, TX, 77005

Introduction: Some planetary scientists are focusing their research on determining how the Earth was formed. Currently there are several different hypotheses dealing with the size of the magma ocean that was present on the early Earth. Some scientists hypothesize a shallow magma ocean [1], others a deep magma ocean [2], while some hypothesize heterogeneous accretion which requires no magma ocean at all [3]. In this study, the element Ge is used to observe the way siderophile elements partition into the metallic core [1]. Previous models are still unable to account for Ge depletion in Earth's mantle relative to CI chondrites, such as the model for heterogeneous accretion discussed by Newsom and Sims [3]. The purpose of this research is to provide new data for Ge and to test these models further.

The partition coefficients of siderophile elements can be studied by performing series of high pressure, high temperature experiments. Ge is a moderately siderophile element found in both the mantle and core, and has yet to be studied systematically at high temperatures. Although this study will focus on the effects of temperature, partition coefficients are also functions of oxygen fugacity, and metal and silicate composition [1].

Reported here are results from 16 experiments studying the partitioning of Ge between silicate and metallic liquids. These experimental data focus on adding information to core-mantle separation that occurred in Earth's early stages. The data may also be applicable to other differentiated rocky bodies including Mars, the Moon, or Vesta.

Procedures: The sample used for these experiments was a powder containing 70 wt.% Knippa Basalt, composition described in Lewis et al. [4], and 30 wt.% Fe, Ge mixture. The metal mixture contained 95 wt.% Fe and 5 wt.% Ge. Two different types of capsules were used: MgO and Graphite. All experiments were performed using a piston cylinder apparatus at constant pressure with various times and temperatures. Once the samples were brought to a constant pressure of 10.3 kbars, they were then heated to higher temperatures. Using data from previous studies, samples were brought to temperatures high enough to attain equilibrium and were heated for durations based on diffusion times across capsule distance ([5, 6]). The temperature was measured using Type C thermocouple (W-Re) wires with an accuracy of $\pm$2°C. Samples were quenched by turning off the power and keeping constant pressure until the temperature reached 100°C.

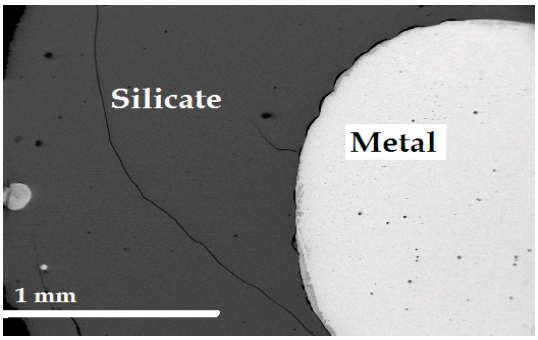

Figure1. BSE image of sample Ge62409b. This sample was run in a graphite capsule at 1800ºC for 15 minutes.

Three different series were performed (Table1)- a time series with graphite capsules and two temperature series each with a different capsule (MgO and graphite). Sixteen successful runs were produced from temperatures between 1500°C and 1800°C. A 1900°C run was performed in an MgO capsule for 10 minutes but was not analyzed in time for this summary.

Analysis: All samples were analyzed for major element composition using a Cameca SX100 for electron microprobe analysis (EMPA) at NASA-JSC. A 10 µm beam was used at 15 kV and 10 nA. Analyses of metal in the graphite capsules resulted in low totals because of carbon saturation in the metal portion of the sample. Carbon content of the metal will be addressed in more detail later in the paper. Figure1 is a back scattered electron (BSE) image from the microprobe of sample Ge62409b.

For all samples, Ge content of the glasses was lower than the detection limit of the EMPA. Therefore, samples were also analyzed for trace element composition using the Laser Ablation Inductively Coupled Mass Spectrometer (LA-ICP-MS) at Rice University. Given time constraints, only the silicate material for most samples was analyzed. Standards used for the laser analysis were BHVO2g, BCR2g, BIR1g glasses. Medium resolution (MR) and

Table1. Summary of successful experiments in this study performed at 10.3kbars.

Run Label	Temperature (°C)	Duration (mins)	Capsule	ΔIW	Ge_{metal} (wt.%)	$Ge_{silicate}$ (ppm)	D(Ge)
Ge60309	1600	30	Graphite	-1.73	4.22	137	307
Ge60209b	1600	60	Graphite	-1.73	4.12	83	494
Ge60409	1600	90	Graphite	-1.72	0.02	0	13864*
Ge60509b	1600	120	Graphite	-1.75	4.47	125	357
Ge61109b	1500	180	Graphite			82	
Ge62509b	1500	180	Graphite	-1.72	3.95	120	328
Ge72409	1600	90	Graphite	-1.77	4.55		
Ge61209b	1700	45	Graphite	-1.73	4.61	280	165
Ge72009	1700	45	Graphite	-1.73	4.10		
Ge62409b	1800	15	Graphite	-1.74	4.20	270	155
Ge61609	1500	180	MgO	-1.92	5.18	33	1572*
Ge72109	1500	180	MgO	-1.97	4.21		
Ge61509	1600	90	MgO	-2.22	4.69	153	307
Ge62409	1700	45	MgO	-2.36	4.33	101	428
Ge61809	1700	45	MgO				
Ge61909	1800	15	MgO	-2.30	4.86	79	617
Ge72309	1900	10	MgO				

*anomalous results – see text for explanation.

Low resolution (LR) analyses were taken and the data was then normalized to ^{25}Mg isotope. Isotopes ^{73}Ge and ^{74}Ge were among the trace elements analyzed and were the only ones specifically studied for the purpose of this research. Data from the analysis of isotope ^{74}Ge at MR was used to calculate Ge in ppm in the silicates.

As mentioned previously, some microprobe analyses performed on the samples containing graphite capsules came up with low totals. An explanation provided by Dasgupta and Walker [7] states that between temperatures of 1300°C and 1800°C, the carbon solubility curve is nearly vertical at roughly 5.5 wt.% C in the Fe metal. This suggests that there is up to 5.5 wt.% C missing from the analyses performed by the microprobe. As a result, the silicate and metal melt compositions should still be constant over the span of temperatures in this study.

Results: Partition coefficients were calculated using the equation:

$$D_{Ge} = c_{metal}/c_{silicate} \quad \text{(eq1)},$$

where D = partition coefficient of Ge and c = concentration of Ge in the metal and silicate respectively. Looking at Table1, two calculated partition coefficients appear far greater than expected. For sample Ge60409, microprobe analysis shows very little Ge in the sample (<1wt.%). Sample Ge61609 contains large quench crystals that made both laser and microprobe analyses of the silicate material difficult to the point where the portions of the sample ablated were either capsule or crystal. These anomalous results were therefore excluded from the discussion.

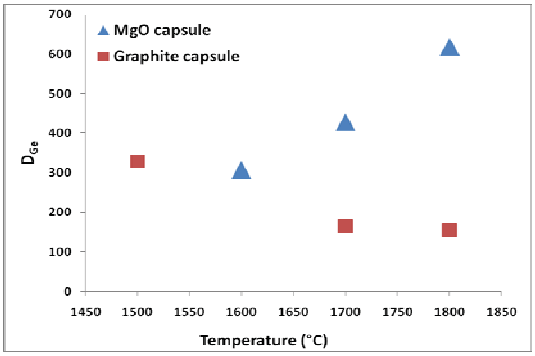

Figure2. This figure is a plot of the two temperature series (graphite and MgO capsules) versus the partition coefficient. MgO capsule samples have variable composition and fO_2 while the graphite capsule samples have constant composition and fO_2.

On average, samples using MgO capsules that were analyzed for major element composition showed a higher Ge content in the metal spheres with 4.2-5.2 wt.% Ge versus 4.0-4.6 wt.% Ge in the samples using graphite capsules. Figure2 shows a plot of the two temperature series. The samples in MgO capsules show a general increase of D_{Ge} as temperature increases while the graphite samples show a decrease of D_{Ge} as temperature increases.

Oxygen fugacity was calculated relative to the Iron-Wüstite buffer (IW) according to $2\log[X_{Fe}/X_{FeO}]$. Figure3 shows the partition coefficient versus ΔIW for the graphite and MgO capsules. Data from Schmitt et al. [8] was included. Originally, the experiments done by Schmitt et al. were to study the effects of oxygen fugacity at 1bar. For this plot, the data from Schmitt et al. was calculated for ΔIW = -1.7 to allow for direct comparison.

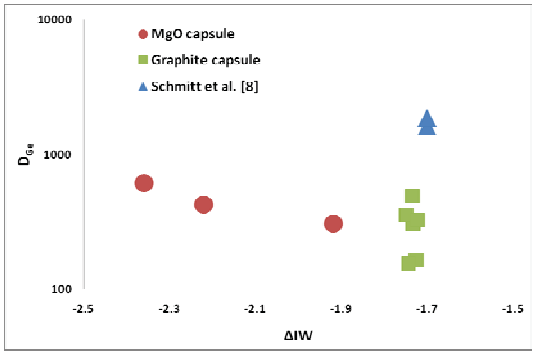

Figure3. Experimental partition coefficents versus the change relative to the Iron- Wüstite buffer for graphite and MgO capsule experiments. Schmitt et al. [8]

Discussion: Comparison to the results obtained by Schmitt et al. [8], our new D_{Ge} are lower by a factor of 10 than the 1bar experiments. Jana and Walker [9] performed experiments at 50 kbars at temperatures of 1800°C and 2200°C attempting to study the effects S has on the partition coefficients of siderophile elements. The data from Schmitt et al. [8] and the Jana and Walker [9] experiments are plotted in Figure4. Only the data for experiments containing 0 wt.% S from Jana and Walker are included and the trend in these data points show a general decrease in D_{Ge} as temperature increases.

In order to calculate the D_{Ge} required for equilibrium (or target D_{Ge}) for early Earth, determining the approximate abundance of Ge in the core is necessary. In order to do this, it will be assumed that the bulk composition of early Earth is roughly the same as CI carbonaceous chondrites (32ppm Ge). However, according to the volatility trend of siderophile elements relative to CIs in McDonough and Sun [11], Ge is depleted by a factor of 5. Jagoutz et al. [12] determined the Ge abundance in the upper mantle is close to 1ppm. If the Earth was made of CI material (32ppm) and the mantle abundance is known to be roughly ~1ppm [12], the core would contain ~18ppm of Ge, thus making a target D_{Ge} = 18. This includes a correction for the volatility of Ge and assumes a 32 wt.% core and 68 wt.% mantle.

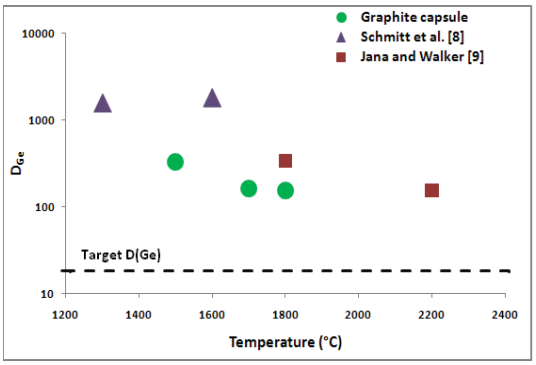

Figure4. Experimental partition coefficients versus temperature. Just the Temperature series runs were included. Data from Schmitt et al. [8] and Jana and Walker [9] are also included.

Conclusions: Based on the evidence presented in this summary, D_{Ge} is affected by temperature, oxygen fugacity, and S concentration. According to Schmitt et al. [8] the lower the oxygen fugacity the greater the D_{Ge}. Comparisons in Figure4 by Jana and Walker [9] and the graphite data suggest temperature causes a minor decrease in D_{Ge}, therefore, target D_{Ge} could be reached at T between 2200°C and 2400°C. Another possibility would be the addition of S. Findings from Jana and Walker [9] show that the presence of S decreases D_{Ge}, consequently, an addition of 5-10 wt.% S could lower the D_{Ge} down to the target value for temperatures between 1500°C and 1800°C.

Evidence suggested here finds Ge possibly consistent with a magma ocean. Based on the data in this summary, extremely high T is not necessary, therefore suggesting a shallow ocean. However, the effects of pressure and silicate melt composition are not completely understood at this time.

References: [1] Righter, K. (2003) *Annu. Rev. of Earth Planet. Sci* 31, 135-74 [2] Li, J., Agee, C., (2001) *Geochim. Cosmochim. Acta* 65(11), 1821-1832. [3] Newsom, H. and Sims, K. (1991) *Science* 252, 926-933 [4] Lewis, R.D. et al. (1993) *Meteorites* 28, 622-28 [5] Righter et al (1997) Physics of the Earth and Planetary Interiors 100, 115-13 [6] Li, J. and Agee, C. (1996) *Nature* 381, 686-689 [7] Dasgupta, R., Walker, D. (2008) *Geochim. Cosmochim. Acta,* 72, 4627-4641 [8] Schmitt, W., et al. (1989) *Geochim. Cosmochim. Acta* 53(1), 173-185. [9] Jana, D., Walker, D. (1997) *Geochim. Cosmochim. Acta,* 61(24), 5255-5277 [10] Jana, D., Walker, D. (1997) *Earth and Planet. Sci. Letters* 150, 463-472 [11] McDonough, W., Sun, S. (1995) *Chemical Geology* 120, 223-253 [12] Jagoutz, E. et al., (1979) *Lunar Planet Sci.*10th, 2031-2050 [13] Jana, D., Walker, D., *Geochim. Cosmochim. Acta* 61(13), 2759-2763.

SHOCK-PETROGRAPHIC STUDY OF IMPACTITES FROM THE CHESAPEAKE BAY CRATER.

L. Malone[1], A. Wittmann[2], and David A. Kring[2] [1]Dept. of Geology, University of New Brunswick, 2 Bailey Drive, Fredericton, NB, E3B 5A3, Canada, lmalone@lpi.usra.edu, [2]Lunar & Planetary Institute, 3600 Bay Area Blvd. Houston, Tx. 77058, wittmann@lpi.usra.edu; kring@lpi.usra.edu

Introduction: The 80-95 km Ø Chesapeake Bay impact structure (CBIS) formed in the late Eocene on the continental margin of what is now Virginia. The oceanic impact involved a target with a water depth of 0-340 m above 400-1500 m of unconsolidated siliciclastic sediments overlying a Neoproterozoic crystalline basement. The ~38 km diameter central crater has a ~12 km wide central uplift surrounded by an annular moat that is bounded by an uplifted escarpment [1]. Polymict impact breccias (PIB) were recovered in drill cores from the central uplift, and the annular moat, 1 and 9 km from the crater center, respectively. Initial petrographic analyses [2, 3, 4] of these PIB raised questions about the amount of impact melt particles in these rocks. A detailed shock petrographic study of these impact breccias aims to elucidate the origin of PIB in the target stratigraphy and the respective cratering processes responsible for their emplacement.

Samples and Methods: Six thin sections from the Eyreville-B drill core in the CBIS's annular moat and two thin sections from the Cape Charles drilling in the central uplift were studied. Scanned, five-fold enlarged images of these thin sections were used for image analysis. Lithological groups were distinguished petrographically and their relative proportions in the clast fraction >1mm determined. A shock-petrographic analysis of each clast >1mm was performed, based on diagnostic features in the rock-forming minerals [5]. Using Energy Dispersive Spectroscopy (EDS) and Scanning Electron Microscopy (SEM), $ZrSiO_4$ grains were located and imaged in each thin section. Raman spectroscopy was performed on thin section E1481.37 to determine if the high pressure polymorph reidite is present. Quantitative analysis of $ZrSiO_4$ phases using the electron microprobe was completed on thin sections E1481.37 and E1505.32.

Results: *Petrography:* The Eyreville-B samples stem from a 5.5 m thick, clast-rich impact melt rock (E1404 m) that is mainly composed of impact melt and variably assimilated lithic clasts [4], whereas samples E1481.37, E1505.32, E1536.1, and E1548.28 m originate from PIB that occur as ~4 to 16 m thick intercalations in-between unshocked schist blocks (P1-P4 of [2, 4]). The PIB samples exhibit the highest area fraction (≥48%) of clasts >1mm. Lithic sedimentary clasts exhibit sedimentary layering instead of metamorphic or igneous fabrics. Igneous clast types contain granitic to pegmatitic types. Less often, mafic igneous clasts were found that appear to be derived from dolorite or basalt precursors. Metamorphic clasts of upper greenschist to upper amphibolite facies are the most common clast type. Sample E1607.45 is from a breccia dike in allochthonous basement blocks. It contains several dark, vesicular graphite clasts that contain abundant angular quartz grains, along with clasts derived from calc-silicates (phlogopite-carbonate-quartz-scapolite-plagioclase) in a fine-grained, particulate matrix. Most Eyreville-samples do not exhibit pervasive secondary alteration. This is in stark contrast to the two samples of the Cape Charles drilling (C783.28 and C771.42) that represent the >79 m thick "Crystalline-clast suevite and crystalline-rock megablocks" unit [6]. Both of these samples exhibit abundant carbonate that locally crystallized in wide fractures and locally replaced mafic clast components. Frequently, clasts with fluidal textures and aphanitic textures occur. Their matrixes are composed of clay minerals that do not exhibit liquidus phase phenocrysts. These samples commonly contain target clasts that sometimes exhibit variable shock metamorphic overprints and conspicuous rounding. Sedimentary clasts comprise fragments of biogenic carbonates with well displayed shell structures as well as quartzitic clasts with relic sedimentary layering and possible fragments of glauconite pellets. Most igneous and metamorphic clast components are strongly altered, which is evidenced by the sericitization of feldspar and chloritization of amphibole.

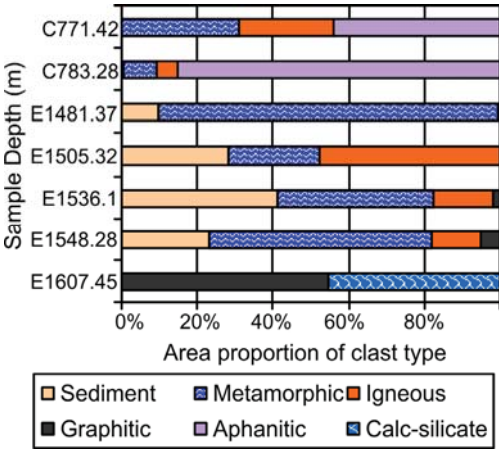

Fig. 1 Proportions of lithological types among clast components >1mm in CBIS-PIB.

The area proportions of clast types displayed in Fig. 1 shows that graphitic clasts are restricted to samples E1536.1, E1548.28 and E1607.45. This may be

due to the proximity to graphite-bearing schists between 1542.78 and 1545.09 m and the nature of the calc-silicate host rock of the breccia dike at 1607 m depth in Eyreville-B. Breccia dike sample E1607.45 did not contain shocked components and appears monomict. Altered mafic clasts are very minor components in the samples studied (<<1%).

Samples E1607.45, C783.28 and C771.42 have the three highest proportions of matrix area: 89.5%, 69.7% and 91.7% respectively, which correlates with also having the smallest average clast sizes: 1.6, 1.3 and 2.2mm, respectively.

Shock petrography: The relative degree of shock metamorphism was related to the occurrence of 1-2 sets of planar deformation features (PDF) in quartz (shock stage 1A, ~10-20 GPa), more than 3 sets of PDF in quartz (shock stage 1B, ~20-35 GPa), diaplectic quartz glass (shock stage II-III~35-60 GPa), and whole rock melts (shock stage IV, >60 GPa). Most clasts in the PIB samples suffered shock stage 1A overprints (Fig. 2) and possible shock stage II-IV clasts >1mm only occur in sample C771.42.

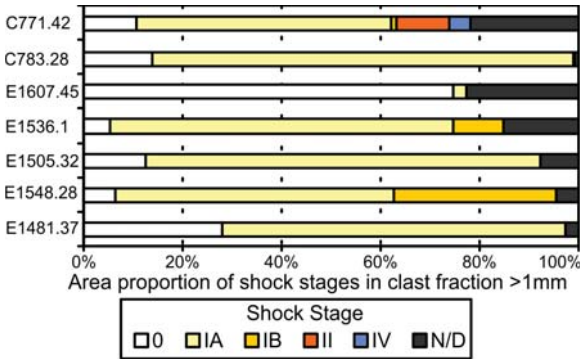

Fig. 2 Area fraction of shocked components >1mm in CBIS-PIB.

Zircon contents: SEM images were taken of 212 zircons >13 µm (Fig. 3 A-D). In the PIB thin sections, 159 zircons were found, of which 88 occur in lithic clasts. An average density of 5 zircons/cm^2 of thin secion area was calculated with 14 % zircon crystals hosted in sedimentary clasts, 4% in igneous clasts, 32% in metamorphic clasts and 50% in the matrix. Shapes in sedimentary clasts are preferentially subhedral (39%), anhedral in metamorphic clasts (39%) and subhedral in igneous clasts (43%). The abundance of zircons with metamict domains in metamorphic hosts is 18%, 29% in igneous hosts and 17% in sedimentary hosts. Of the 53 zircon crystals in melt rock E1404.2, 43 are located in the melt of which 84% exhibit decomposition textures (Fig. 3D).

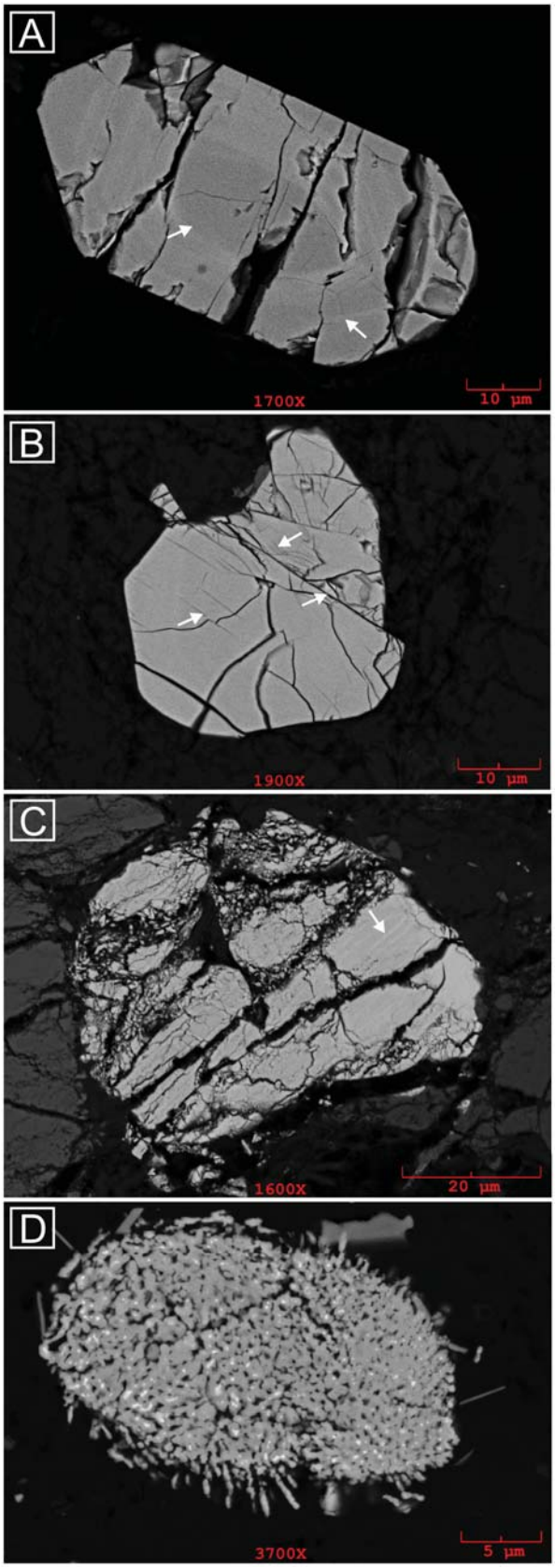

Fig. 3 SEM-backscattered electron (BSE) images of zircons with increased impact-related deformation from top to bottom:

(A) Moderately fragmented zircon grain in a shock stage IA clast showing concentric zoning (arrows) from section E1505.32. (B) Moderately fragmented zircon in a metamorphic clast of shock stage IB in sample E1548.28, showing distinct planar fractures, some of which accomodated displacement (arrows). (C) Stongly fragmented zircon in shock stage II clast in sample E1536.1, showing lamellar features (arrows). (D) Decomposed grain with granular recrystallization texture from sample E1404.2.

Zircon crystals in lithic clasts of E1404.2 exhibit no decomposition textures.

Of the 56 zircon crystals associated with shock stage 1A lithic clasts, 25% exhibit minor fractures (Fig. 3A), 54% exhibit moderate fracture patterns that sometimes are densely spaced planar fractures (Fig. 3B) and 21% exhibit strong fracturing (Fig. 3C). Of the 13 zircons associated with shock stage 1B clasts, 75% are moderately and 25% are strongly fractured.

Raman spectroscopy revealed the occurrence of one zoned zircon-reidite grain that is associated with an aphanitic clast domain in PIB sample E1481.37 (Fig. 4 A-D). Electron microprobe data and Raman spectroscopy indicates an outer domain that is disordered and non-stoichiometric. Curiously, HfO_2 concentrations appear mostly unaffected (Fig. 4C), while ZrO_2 and SiO_2 and trace elements exhibit strong concentration excursions.

Summary: Shock stage IV components in the samples of PIB of the CBIS were found to be very scarce among the clast components >1mm. One sample of a breccia dike at 1607m appears monomict without diagnostic shock features. Two samples from the Cape Charles drilling exhibit flow textures, biogenic carbonate, and possible glauconite fragments. However, no impact melt was positively identified judging from the zircon population therein. This may indicate that the "Crystalline-clast suevite" in the Cape Charles drilling is part of the resurge deposits on top of the central uplift. This study also reports first chemical data on a natural reidite-zircon grain that shows interesting structural and compositional variations in its rim.

References: [1] Horton et al. (2005) *USGS Prof.Pap. 1688,* A7-A24. [2] Horton et al. (in press) *GSA Spec. Pap. 458*. [3] Bartosova et al. (in press) *GSA Spec.l Pap.* 458. [4] Wittmann et al. (in press) GSA Spec. Pap. 458. [5] Stöffler & Grieve (2007) IUGS Subcommission on the Systematics of Metamorphic Rocks, 82-92. [6] Horton et al. (2008) *GSA Spec. Pap*. 437, 73-79.

Acknowledgments: W. U. Reimold (Humboldt-Universität Berlin) & J. W. Horton Jr. (USGS) for providing the samples for this study. G. A. Robinson, A. Peslier & L. Le (NASA-JSC) for all their help with the instrumentation at JSC. The LPI & J. Moses for organizing the intern program.

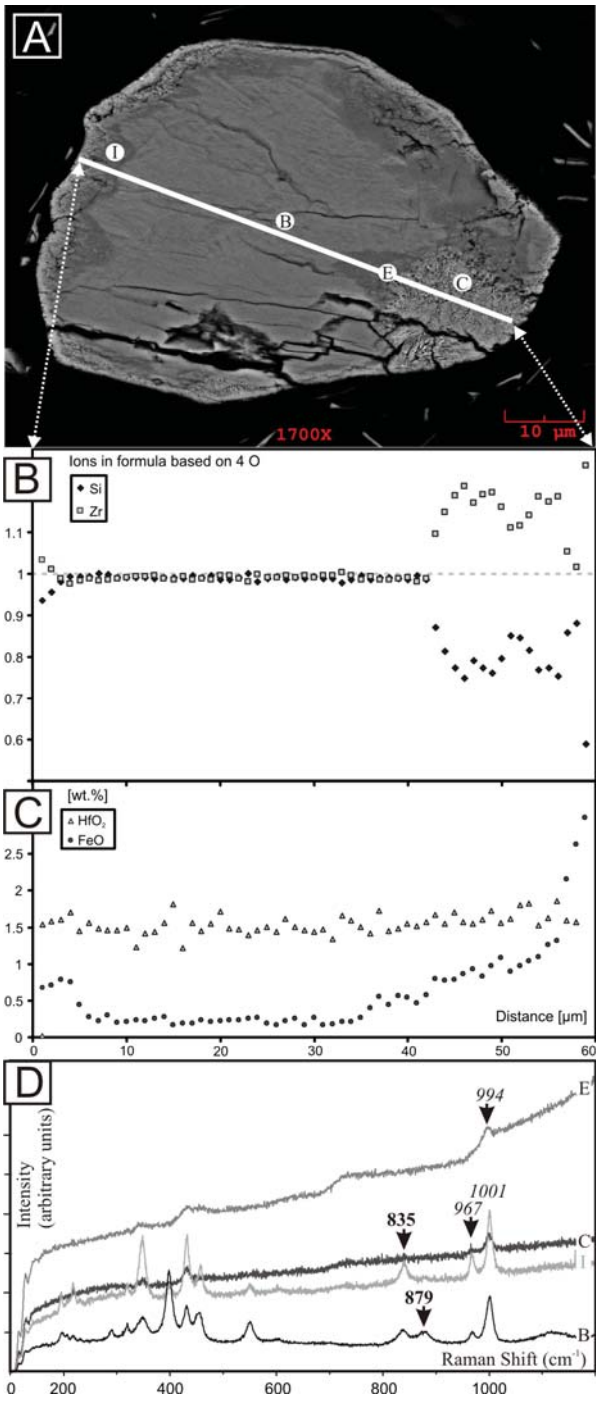

Fig. 4. Zircon-reidite grain in PIB sample E1481.37. (A) SEM-BSE image with EMP measurement traverse of 58 points spaced at 1 µm and Raman-spectroscopy spots. (B) Ratios of Zr and Si formula units based on 4 O atoms. (C) Concentrations of HfO_2 and FeO in measurement traverse. (D) Raman spectra of measurement spots indicated in A). Indicative Raman bands of zircon in italic and reidite in bold numbers.

PROGRESS IN MAPPING DEPTH OF IMPACT CRATERS ON MARS. J. C. McLane[1] and T. F. Stepinski[2]
[1]University of Minnesota, Twin Cities, Dept. of Computer Science, Minneapolis, MN 55455 (mclan011@umn.edu),
[2]Lunar and Planetary Institute, 3600 Bay Area Blvd., Houston, TX 77058, (tom@lpi.usra.edu)

Introduction: Martian craters display great variety and complexity of morphologies because of the wide range of ages on the surfaces on which they are located, and multiplicity of degradational processes to which they are subjected. One morphologic attribute of particular interest is carter's relative depth or its depth/diameter ratio (denoted by *d/D*). Crater depths have been acquired by a variety of methods with different standards of accuracy. The photoclinometric technique was used by [1], [2], and [3]. [4], [5], and [6] used individual altimetric profiles obtained by the Mars Orbiter Laser Altimeter (MOLA). Finally, [7] and [8] calculated crater depths from a MOLA-based digital elevation model (DEM). However, in order to take a full advantage of information contained in the entire Martian crater record, a global map of *d/D* is needed. With this in mind [9] have developed a topography-based crater detection algorithm that automates the process of crater detection and calculation of their depths. Applying this algorithm to the entire 128 pixels/degree MOLA Mission Experiment Gridded Data Record (MEGDR) [10] identified 75,919 craters having diameters $D \geq 3$ km and calculated their relative depths. This catalog [10] (hereafter referred to as Stepinski-Urbach) was used to construct a global map of *d/D* that revealed a pattern consistent with the existence of the cryosphere at depths that decrease toward the poles. However, due to limited quality of the MEGDR and a limited accuracy of the crater detection algorithm, the Stepinski-Urbach catalog is not complete. In particular, certain types of craters common in northern planes, such as, for example pedestal craters, are underrepresented in the catalog. This incompleteness may lead to a skew spatial distribution of dept/diameter ratio. The purpose of this project was to update the Stepinski-Urbach catalog by adding the craters that were not detected by an automatic method.

Compiling updated catalog of craters. We have chosen to update Stepinski-Urbach catalog by cross-referencing it with a recent catalog of Martian craters published by [11] (hereafter referred to as Salamuniccar-Loncaric). The Salamuniccar-Loncaric catalog contains 57,633 craters and was created by merging many previously existing catalogs compiled manually from imagery data. Because the craters in the Salamuniccar-Loncaric catalog have been detected from images, the catalog contains many craters that are just not present in the MEGDR. On the other hand, crater depth cannot be calculated from images, so values of *d/D* are not available in the Salamuniccar-Loncaric catalog. Our procedure was to identify craters that are present in the Salamuniccar-Loncaric catalog but absent from the Stepinski-Urbach catalog. These additional craters were than added to the Stepinski-Urbach catalog after we have calculated their depths.

We created an algorithm, implemented in MATLAB, which for every crater in the Salamuniccar-Loncaric catalog finds a crater in the Stepinski-Urbach catalog that is nearest to it. A combination of two criteria is used to establish whether such a pair constitutes two measurement of the same crater.

Proximity of centers criterion. This criterion calculates a distance between the centers of the pair of craters and compares it to the average size of the two craters. After analyzing the results using different values of a threshold, we decided that the threshold value of 0.5 works well. Choosing such cutoff means that the two craters are deemed to represent the same crater if their centers lie within the area encompassed by their radii.

Proximity of sizes criterion. The second criteria take into consideration diameters of the two craters. The pair of craters may have their centers located near each other, but their diameters may differ; such pair do not represent a single crater. The absolute value of difference between the diameters of the two craters divided by the average diameter constitute a variable that measures proximity of crater sizes. After analyzing result of experimenting with different value of threshold, we decided to use the value of 0.1. This means that two pair of craters represent a single crater if their diameter are within 10% of each other.

Using these two criteria we match the objects in the two catalogs that represent the same craters. We found that 39,466 craters are common to the two catalogs. 36,452 craters are only present in the Stepinski-Urbach catalog; these are predominantly small craters which were not object of manual mappings. Finally, 18,166 craters are found only in the Salamuniccar-Loncaric catalog; these are craters that was either missed by an automatic detection algorithm or had incomplete representation in the MEGDR. After adding those crater, the updated catalog lists 94,084 craters.

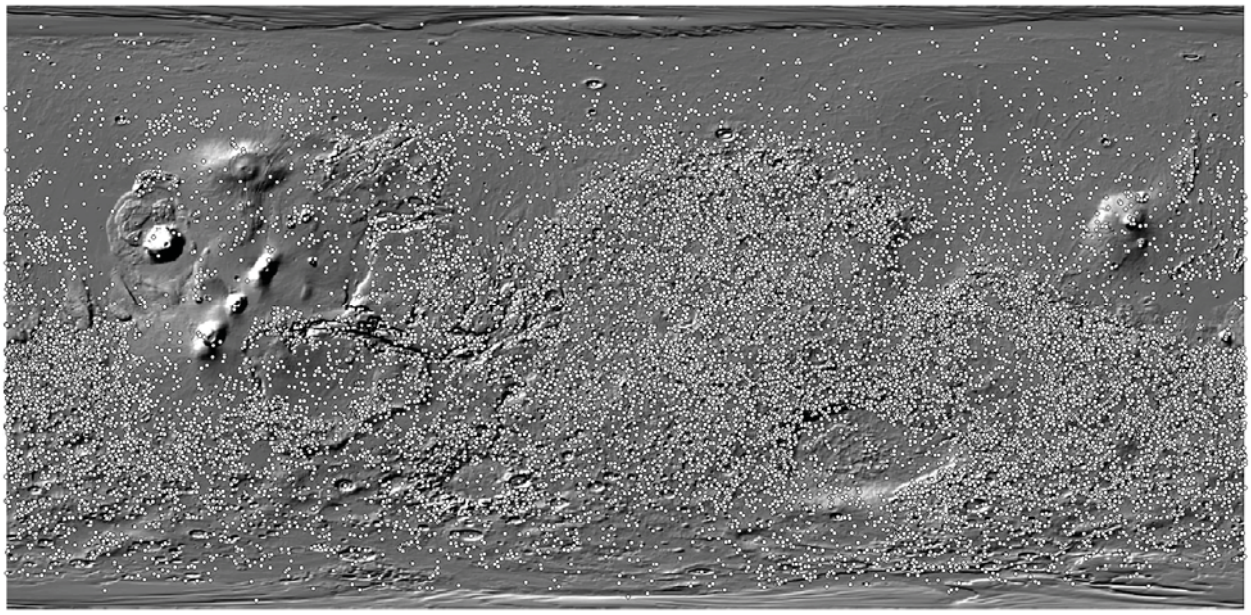

Figure 1. Positions of 18,166 craters added from the Salamuniccar-Loncaric catalog.

Calculating depths of craters. In order to calculate depth of the additional 18,166 carters we first extracted clips of MEGDR around centers of these craters. The positions of the centers and the diameters for these craters are already known from the the Salamuniccar-Loncaric catalog; we use this information to extract small grids of elevation data at the location of each crater from the global raster of MOLA-derived elevations. Each local grid is centered at the center of a corresponding crater and has a linear size twice the size of the carter diameter. We used the ArcGIS software in conjunction with Python script to automate the extraction of the local elevation grids. Once all grids were extracted we use another script to obtain four topographic cross section of each crater along four primary directions (N-S, W-E, NW-SE, SW-NE). These cross sections were analyzed to extract diameters and depths of the craters. Note that diameters are already known, we calculate them to validate our method and for comparison with manual measurements.

Diameter Calculation. For each cross section we first find the locations corresponding to a crater rim. Using existing information on the location of the center and the size of the diameter, two bins are created at the opposite sides of the profile in the probable locations of the rim. The elevations within those bins are analyzed and the locations of maximum elevation in each bin are registered. The profile-specific diameter is the distance between these two locations. The crater diameter is an average of the four cross section specific diameters.

Depth Calculation. The depth is assumed to be a difference between an elevation of the rim and the elevation of the floor. For each profile the elevation of the rim is calculated while calculating a diameter (see above). Using a histogram of elevation levels within a crater, the floor is identified as a level of maximum count and length along that level. If such level does not exist, the floor is assumed to coincide with the minimum elevation level. The depth is an average of the depths calculated from the four different profiles.

Results. Figure 1 shows positions of the 18,166 craters which were added to the Stepinski-Urbach catalog from the Salamuniccar-Loncaric catalog. The distribution of the additional craters follows the overall density of craters on Mars; this means that Stepinski-Urbach catalog is not biased to any particular surface and that global maps of d/D produced on its basis reflect well the actual distribution of crater depths on Mars. However, the additional craters improve the completeness of the catalog. Our calculations of crater diameter yield values that are on average 16% larger than manual measurements. We were able to calculate depth only for 14,035 craters, for the remaining craters the quality of MEGDR was too poor to allow depth calculation. Depth and diameter calculations were only recorded if at least 2 cross sections were of sound quality. In general the calculated values of *d/D* tend to be somewhat lower than those in the Stepinski-Urbach

catalog. Figure 2 shows a comparison of the *d/D* maps created for craters with diameters <= 5 km from the entire Stepinski-Urbach catalog and from the newly added craters.

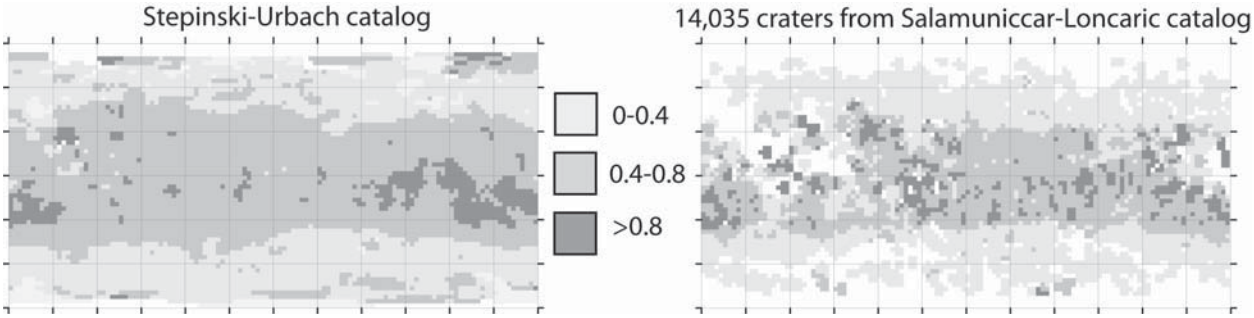

Figure 2. Comparison of crater depth map between craters in the Stepinski-Urbach catalog (left) and the 14,035 craters added from the Salamuniccar-Loncaric catalog (right). Only craters <= 5 km in diameter were used to construct the maps. Maps based on larger craters look different; they are not shown here do to lack of space.

In general, the two maps follow the same pattern - craters are deeper near the equator and shallower near the poles. However, the maps differ in details; the differences are larger for larger craters (not shown here).

Future work. To continue this project we plan on extracting topographic profiles for all craters in the expanded Stepinski-Urbach catalog, so all depths are calculated in the same, consistent manner. In order to assure the best possible result we need to develop a procedure for checking the quality of automatically calculated diameters and depths. Our method not only extracts local elevation grid for each crater in the expanded catalog, it also extracts a local MDIM 2.1 image of each crater and its neighborhood, and an image of relief based on a hillshade representation of the topography. These extensive databases will be used in the future to automate extraction of craters' morphological attributes other than their depths, for example, existence of ejecta, presence of central peak etc.

The major challenge is to develop a reliable algorithm for calculating the depths. Martian craters have variable and complicated morphologies, and their floors and rims are often poorly defined. The current algorithm identifies the rims and the floors on the basis of certain, rather simple assumptions. These assumptions need to be evaluated given the results, and an algorithm may be revised to make better estimates of the depth.

References: [1] Pike R.J. and Davis P.A. (1984) *LPS XV*, 645-646. [2] Mouginis-Mark P.J. and Hayashi J.N. (1993) *Earth Moon Planets 61(1)*, 1-20. [3] Craddock et al. (1997) *J. Geophys. Res 102(E6)*, 13321-13340. [4] Garvin J.B. and Frawley J.J. (1998) *Geophys. Res Lett. 25*, 4405-4408. [5] Garvin J.B. et al. (2000) *Icarus 144*, 329-352. [6] Forsberg-Taylor N.K. et al. (2004) *J. Geophys. Res. 109(E5)*, 1-4. [7] Mouginis-Mark et al. (2004) *J. Geophys. Res. 109(E8),* 6. [8] Stewart S.T. and Valiant G.J. (2006) *Meteoritics Planet. Sci. 41(10)*, 1509-1537. [9] Stepinski T.F. et al. (2009) *Icarus*. [10] Stepinski T.F. and Urbach E.R. (2009) *LPSC XL, abs.1338*. [11] Salamuniccar G. and Loncaric S. (2008) *Planet. Space Sci. 56*, 1992-2008.

SCATTERING PROPERTIES OF LUNAR GEOLOGICAL UNITS REVEALED BY THE MINI-SAR IMAGING RADAR, CHANDRAYAAN-1 MISSION. Chelsea J. Payne[1] and Paul D. Spudis[2], [1]University of Wisconsin-River Falls Department of Geology, 410 S. Third St., River Falls, WI 54022 (chelsea.payne@uwrf.edu), [2]Lunar and Planetary Institute, 3600 Bay Area Blvd., Houston, TX 77058.

Introduction: Understanding the radar backscattering properties of non-polar areas of the lunar surface is critical to a better understanding of the lunar poles and their deposits. The lunar surface is covered with fine-grained unconsolidated debris, called regolith, that overlies bedrock. Some of this debris is coarse-grained, including larger blocks and boulders. Surface roughness affects the manner in which radio waves are reflected from planetary surfaces. Understanding how different terrains diffusely reflect radio frequency (RF) energy was the task of this study.

An imaging radar (the Miniature Synthetic Aperture Radar/ Mini-SAR) aboard India's lunar orbiter, Chandrayaan-1, has recorded S-band (λ=12.6 cm) SAR images of both poles and several non-polar areas [1]. One important parameter to characterize surface backscatter is the circular polarization ratio, the ratio of the power of the received signal in terms of the same sense transmitted v. the opposite sense [2]. Circular Polarization Ratio (CPR) values were obtained from a variety of locations on the lunar surface. These data can be collected from mapped lunar geological units, allowing us to determine typical and unusual reflection properties for each terrain. Utilizing this knowledge of radar backscatter from the well studied non-polar units will help us infer the geological make-up and surface properties of the less studied and more poorly known polar units of the Moon.

Methods: SAR image strips were registered to regional basemaps of Lunar Orbiter IV or Clementine images. Other resources, including high resolution digitized Apollo rectified pan frames, Lunar Topographic Orthophotomaps and USGS lunar geologic maps were compiled and co-registered with both the respective uncalibrated SAR data and regional basemaps, using Adobe Photoshop CS3. With each resource on a separate layer, the areas of previously defined geologic units underneath the SAR strip were re-mapped in higher resolution and redefined, as necessary (Figure 1.).

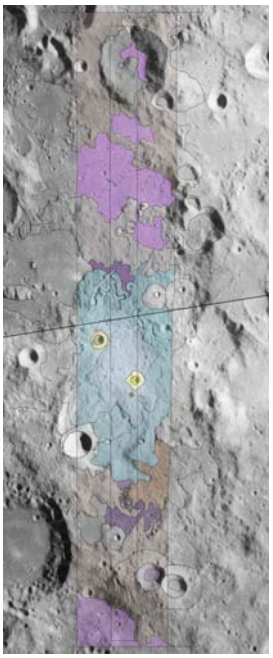

Fig. 1. Adobe Photoshop compilation of Apollo 16 landing site resources.

Calibrated SAR CPR strips were then overlain on the geological maps. Small areas, on the order of hundreds of pixels to a few thousand pixels, were selected to represent each geologic unit present under the SAR CPR coverage. Information about the selected area was collected in the form of a histogram generated in Photoshop. The histogram records the brightness of each pixel in the selected area using a DN scale of 0 (black) to 255

(white). The histogram also records statistical information for each area studied, including the mean, standard deviation, median, and number of pixels selected to create the graph (Fig. 2). The 8-bit data number (DN) values were converted to floating point 32-bit CPR values using the following relation [3]:

CPR (32-bit) = 8-bit DN * (max DN/255)

From this relation, it is noted that the recovered CPR values are not exact due to loss on conversion to floating point values.

Averaged mean CPR values of each geological unit were derived from the individual mean CPR measurements. This value was then plotted against its respective geologic unit, with the geologic units organized by relative age, from oldest to youngest. Finally, the graphs were analyzed for systematic trends associated with the scattering behavior based on the geological unit.

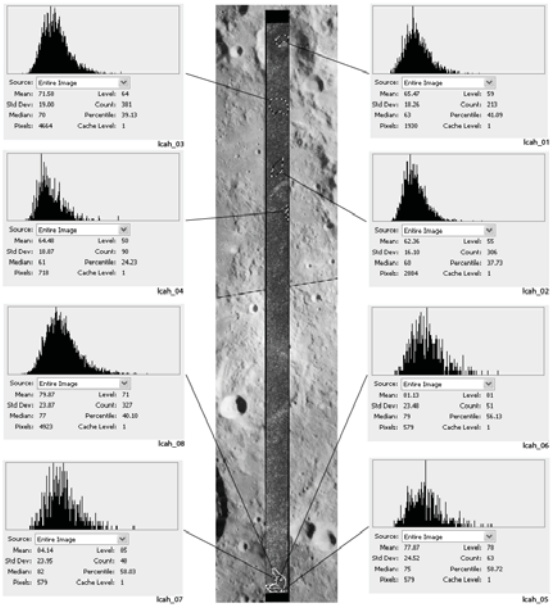

Fig. 2. Data collection on CPR images using Photoshop

Discussion: High CPR values are found to be associated with rougher and/or steeper surfaces, such as basin massifs, with the highest values usually assigned to fresh crater rim material. Young, fresh craters overall have a high average CPR value. Low CPR values are found to be associated with relatively smooth surfaces such as the maria (Table 1.). Generally, older geologic units are more subdued and therefore have a lower CPR value overall than younger units.

CPR values collected and represented here were compared to values measured from Arecibo Earth-based radiotelescopic data [4] and found to be in general agreement. Figure 3 shows an example of collected Mini-SAR CPR data.

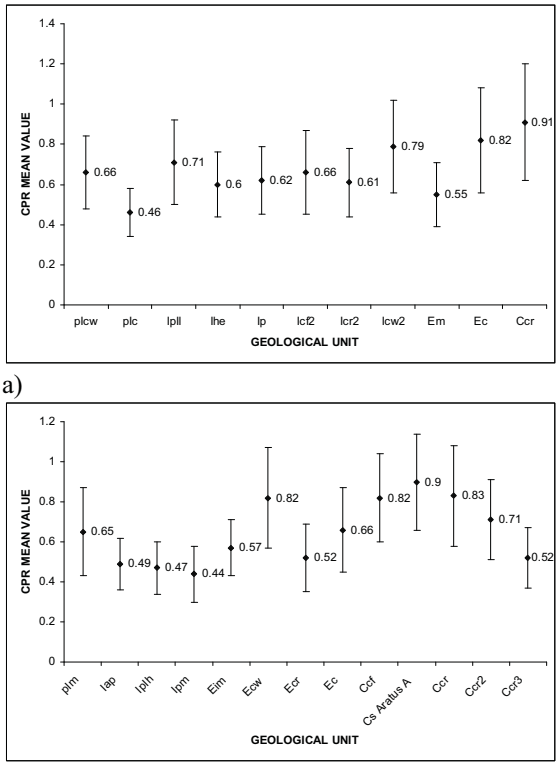

Fig. 3. a) CPR data collected for the area surrounding the Apollo 15 landing site. b) CPR data for the area surrounding the crater, Byrgius.

CPR values are affected by the size of the area from which data are collected. Increasing the area causes higher homogenity by including, for instance, rougher areas such as small

craters and other ejecta material, thereby increasing the overall CPR value. However, collecting too small of a sample could also mean a shift in datum representation, so small samples were taken in the range of about 500 pixels to 1200 pixels. Large samples of these same areas were taken in the range of the upper thousands and ten thousands.

Conclusions: CPR values vary according to geological unit and to the relative degree of unit freshness. Although a general increase in mean CPR is observed with increasing geological youth, this trend is not strong and several areas have been identified where values are lower than expected. This could mean that the units are incorrectly mapped or it could mean that initial conditions of units are not all identical. The averaged mean CPR for all the areas studied is 0.58 ± 0.17. Such a value is slightly higher than the mean CPR suggested by Earth-based radar for the bulk Moon, ~0.2 [4], but corresponds to measurements of individual terrains from the Arecibo S-band radar [5]. Future work will include gathering more CPR data for more terrains around the Moon, examining these areas in the new high-resoloution images from LRO, and correlating them with estimates of surface roughness and maturity derived optically. Finally, these results allow us to better interpret and understand CPR variations in polar deposits, including the possible identification of ice deposits.

References:

[1] Spudis P.D. et al. (2009) Current Science (India) v.96, no. 4, 533-539.
[2] Spudis P.D. (2006) Ice on the Moon. The Space Review.
http://www.thespacereview.com/article/740/1
[3] Thomson, B. (2009) personal communication.
[4] Ostro, S.J., (2001) "Planetary radar astronomy," in The Encyclopedia of Physical Science and Technology, 3rd Edition, vol. 12, R. A. Meyers, Ed.: Academic Press, 2002, pp. 295-328.
[5] Carter, L., (2009) personal communication.

AREA	Avg CPR	Low CPR (Unit)	High CPR (Unit)
Aristarchus	0.47 ± 0.12	0.40 (If)	0.60 (Ccr)
AS15	0.65 ± 0.19	0.44 (Ipm)	0.83 (Ccr)
AS16	0.47 ± 0.14	0.41 (Icah)	0.59 (Ccr)
Byrgius	0.67 ± 0.20	0.46 (pIc)	0.91 (Ccr)
EqW	0.55 ± 0.16	0.47 (dkmantl?)	0.66 (Cs)
Kopff	0.60 ± 0.20	0.40 (Elm)	0.83 (Cs)
Maunder	0.64 ± 0.19	0.48 (Elm)	0.77 (Ecw)

Table 1. Average CPR of each of the areas studied is shown, as well as the local unit low and high CPR values.

Mineral Chemistry and Origin of Mare Basalt Fragments in Lunar Highland Meteorites. K.L. Robinson[1] and A.H. Treiman[2], [1]Dept. of Geophysical Sciences, University of Chicago, 5734 S. Ellis Ave., Chicago, IL 60637 [2]Lunar and Planetary Institute, 3600 Bay Area Blvd., Houston, TX 77058.

We studied the pyroxene chemistry in basaltic fragments in several different lunar meteorites. We classified the fragments by the Ti content of their pyroxenes and compared them to pyroxene composition trends in Apollo mare basalts. Several of our studied clasts fell between the defined very-low-Ti, low-Ti, and high-Ti basalt classifications. We found that our Ti composition data had a unimodal distribution rather than the bimodal distribution of the Apollo mare basalts.

Introduction: Lunar meteorites are important because it is likely that they represent parts of the Moon that were not directly sampled by the Apollo or Luna missions. In particular, meteorites from the lunar highlands are interesting because they may provide a broader representation of average highlands materials than the Apollo samples [1]. Many of these meteorites are breccias with both highlands and mare material. However, basaltic fragments in highland meteorites have not been well-characterized. Our study focused on basaltic fragments in three highlands meteorites: ALH81005, MAC88105, and QUE93069. Only one basaltic clast in ALH81005 had been previously described [2]. We hypothesize that characterization of basalt fragments in these lunar highland meteorites could allow us to narrow down possible source regions, based on the types of basalt (high, low, or very low titanium) found in each meteorite.

Samples and Methods*:* Six thin sections were analyzed with optical and EMPA techniques. Lunar highlands material included thin sections of the anorthositic regolith breccias ALH81005,9; QUE93069,36; and MAC88105,164. Other samples analyzed included thin sections of: the anorthosite-bearing basaltic regolith breccia QUE94281,7; an anorthosite-bearing basaltic fragmental breccia MET01210,18; and regolith returned by Luna 24 (section 24105,15).

Basaltic fragments were identified and imaged using a Leica polarizing microscope. Chosen clasts had crystalline basaltic (ophitic and subophitic) textures and nearly equal proportions of feldspar and pyroxenes. Partially melted or impact melt clasts were excluded. Chemical analyses were carried out at Johnson Space Center-ARES on the Cameca SX-100 electron microprobe with: accelerating potential of 15kV, beam current of 20 nA, Na and K analyzed first to reduce losses through volatility, and count times of 60 seconds for Ti and Cr, and 20-30 seconds for other elements. Standards were well-characterized natural and synthetic oxide compounds. Raw data was reduced using Cameca PAP software, and further processed with Microsoft Excel.

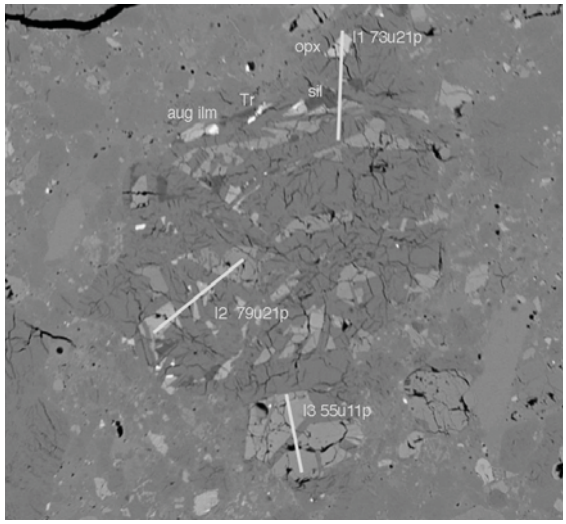

Figure 1. BSE image of ALH81005 LB4. Notable minerals have been labeled: cpx is augite; opx is pigeonite; ilm is ilmenite; Tr is troilite; sil is silica; darker gray is plagioclase. Lines indicate microprobe analysis lines, labeled with length in μm and number of points per line.

Results: We found several basaltic fragments in lunar meteorites of highland and mare origin. We studied many new clasts, as well as some clasts described in the literature. Chemical analyses of pyroxenes in the fragments showed that at least two meteorites contain two or more types of basalt. We found several previously unclassified basalt fragments do not fit into the high-Ti, low-Ti, and very-low-Ti (VLT) classifications, but fall between these categories. However, we also found some of the new clasts do fit into the Apollo classification scheme.

To classify the basalts we use a Fe/(Fe+Mg) (Fe*) vs. Ti/(Cr+Ti) plot after Nielsen and Drake (1978) [3]. This plot shows how less compatible Fe and Ti increase in the melt as more compatible Mg and Cr are incorporated into crystallizing pyroxene. The initial composition of the parent magma determines the evolving pyroxene crystallization trend, and when coupled with the distribution coefficient for Ti, the Ti content of the pyroxene [3, 4].

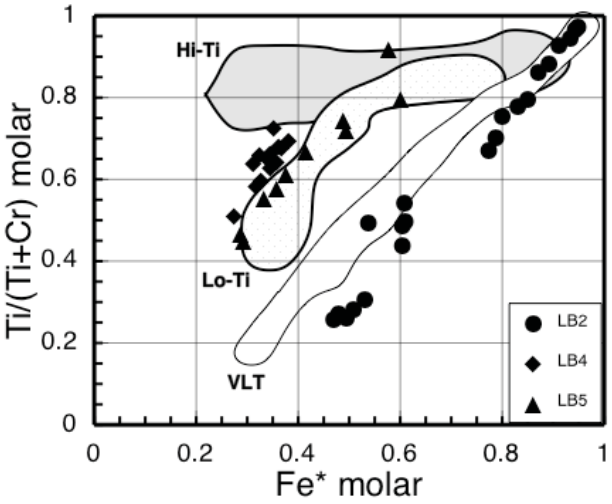

Figure 2. Molar Fe* (Fe/(Fe+Mg)) versus molar Ti/(Ti+Cr) plot of pyroxenes in three different basalt fragments in ALH81005. At least two distinct Ti trends are clear, indicating that there are at least two types of basalt in ALH81005, 9. Apollo data is from [5, 6, 7].

ALH 81005. Treiman and Drake (1983) described a single VLT clast (their clast G) in this thin section [2]. We reanalyzed this clast (here named LB2) and confirm that it is of a VLT basalt. We also analyzed two previously unrecognized basalt fragments, LB4 and LB5. Their pyroxenes contain significantly more Ti than those of LB2. Figure 2 shows Fe* versus Ti/(Ti+Cr) for ALH81005 clasts LB2, LB4, and LB5 and pyroxene composition trends for Apollo mare basalts. LB4 plots between the high- and low- Ti basalt fields.

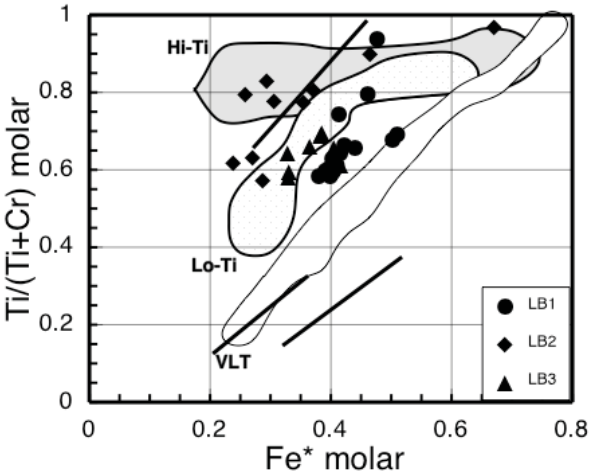

Figure 3. Molar Fe* (Fe/(Fe+Mg)) versus molar Ti/(Ti+Cr) plot of pyroxenes in different basalt fragments in MAC88105. Points are our analyses, while the three fields represent trends from Apollo mare basalts. The lines represent analyses from the literature corresponding to two possible VLTs [9, 10] and a possible high-Ti basalt [8] in MAC88105.

MAC88105. We found three basalt fragments in MAC88105 (figure 3). One appears to fall in the high-Ti field, while the other two plot between the high and low Ti fields. Interestingly, other basalt fragments with possible high-Ti and VLT composition in MAC88105 have been described [8, 9, 10]; see lines on Figure 3. MAC88105 could thus contain the entire range of mare basalt compositions.

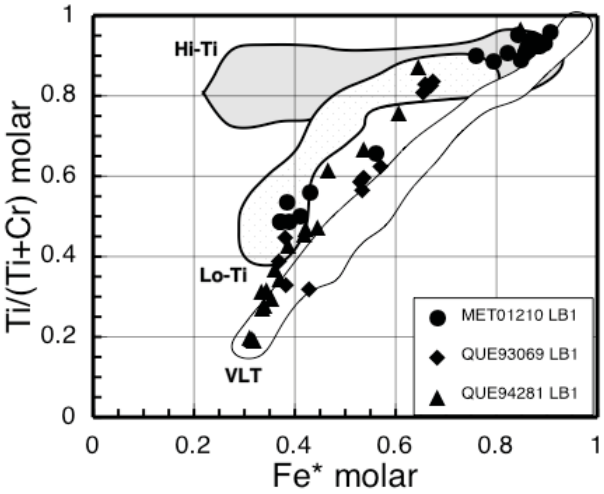

Figure 4. Molar Fe* (Fe/(Fe+Mg)) versus molar Ti/(Ti+Cr) plot of pyroxenes in basalt fragments from MET0210, QUE93063, and QUE94281. Points represent our analyses; fields represent trends from Apollo mare basalts. MET01210 is firmly in the low-Ti field, while QUE93069 and QUE94281 tend to plot between the VLT and low-Ti field.

Other meteorites. Pyroxene compositions from the single analyzed basalt fragment in QUE93069 plot between the low and very low Ti basalt fields (figure 4). We also analyzed basaltic fragments in two regolith breccias of mare origin. Zoned pyroxenes in the largest clast in MET01210 have Ti compositions consistent with Apollo low-Ti basalts [11]. Pyroxene compositions from a basalt fragment in QUE94281 plotted between the low-Ti and VLT fields. These data are shown on figure 4.

Parent Magma Compositions: Using the pyroxene compositions from these mare basalts, one can calculate the TiO_2 contents of their parental magmas using distribution coefficients. We estimated a distribution coefficient for TiO_2, $D^{TiO2}_{(px/basalt)} \approx 0.25$, based on compositions of Apollo mare basalts and their first-crystallized pyroxenes [5], and on experimental data [12, 13]. Actual D values vary from 0.15-0.35, with the variation ascribed to Ca content of the pyroxenes and cooling rate [14, 15]. Figure 5a shows the calculated TiO_2 contents for the clasts' parental magmas at a constant pyroxene Fe* ≈ 0.35.

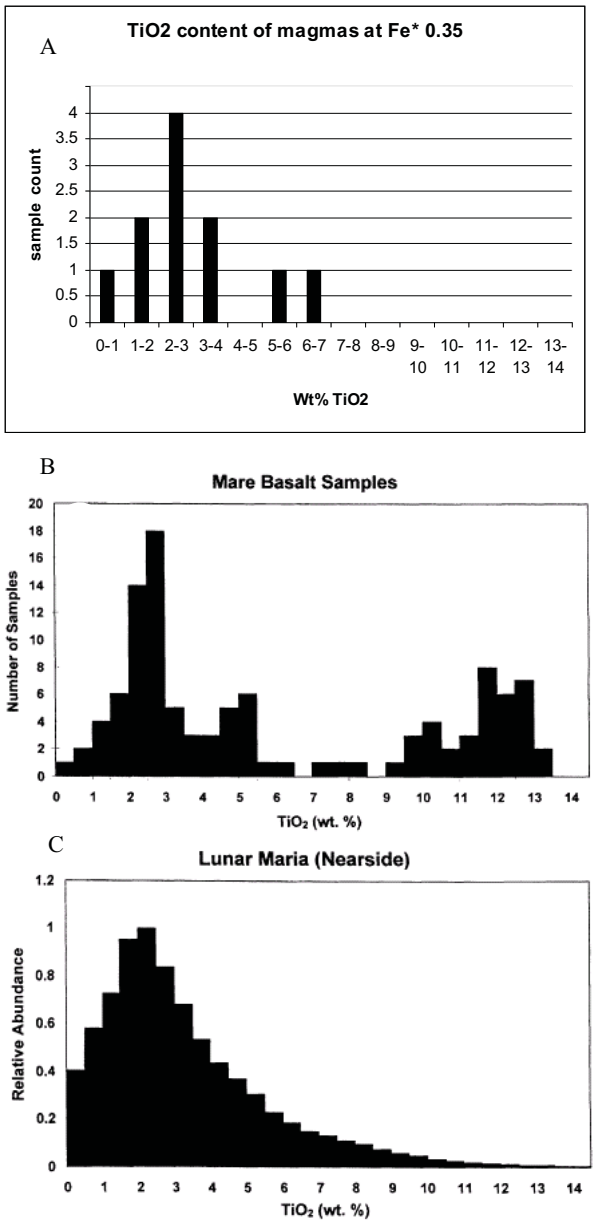

Figure 5. Histograms of TiO_2 contents of mare basalts. A) Magmas modeled from our basalt clasts, calculated for a pyroxene Fe* ≈ 0.35. One basalt glass point from [18]. B) Apollo and Lunar samples of mare basalts, from [16]. The distribution is clearly bimodal. C) From [16]. Histogram of Inferred TiO_2 abundances in lunar mare basalts, based on orbital reflectance data; from [16] The distribution is unimodal and shows a continuum of TiO_2 values.

Conclusion: The range of magma Ti contents inferred from our basalt fragments (Figure 5a) does not resemble the bimodal distribution of Ti abundance in the Apollo mare basalts (Figure 5b). Instead, the distribution of inferred magma composition resembles the unimodal continuum of Ti abundances inferred from orbital remote-sensing data (Figure 5c; [16, 17]). Thus, our observations confirm the remote sensing data with sample analyses, and show again that the high-Ti basalts are over-represented in the Apollo collections.

The current classification scheme for mare basalts does not fit the distribution of Ti abundances in our data and in the remote sensing interpretations. We propose a new group, moderate-Ti basalt, which would be defined as basalt with TiO_2 between 5-9%. The new classifications would then be: VLT < 1.5% TiO_2; low-Ti from 1.5-5% TiO_2, moderate-Ti from 5-9%, and high-Ti >9% TiO_2.

The identification of different types of mare basalts in individual meteorites may also help constrain their possible source craters. TiO_2 maps of the Moon are available [16, 17]. If several types of basalt can be identified in a particular meteorite, a fresh crater with nearby basalt deposits of those compositions could theoretically be found. This would help determine which parts of the Moon have and have not been sampled.

References: [1] Bischoff, A. (1996*) Meteoritics & Planet. Sci., 31,* 849-855. [2] Treiman A. H. and Drake M.J. (1983) GRL, *10,* 783-786. [3] Nielsen R.L. and Drake M.J. (1978) *Mare Crisium: the view from Luna 24,* 419-428, Pergamon. [4] Arai T. et al. (1996) Meteorics *and Planet. Sci.*, *31*, 877-892. [5] Bence A.E. and Papike J.J. (1972). *Proc. 3rd LSC 1*, 431-469. [6] Dymek R.F. et al. (1975) *Proc. Lunar Sci. Conf. 6th*, 49-77. [7] Vaniman D.T. and Papike J.J. (1977) *Proc. Lunar Sci. Conf. 8th,* 1443-1471. [8] Jolliff B.L. et al. (1991) *GCA* 55, 3051-3071. [9] Koeberl C. et al. (1991) *GCA* 55, 3073-3087. [10] Takeda H. et al. (1991) *GCA* 55, 3009-3017. [11] Day J.M.D. et al. (2006) *GCA* 70, 5957–5989. [12] Duke J.M. (1976) *Journal of Petrology, 17,* 499-521. [13] Jones J.H. (1995) *Rock Physics and Phase Relations,* 73-104. AGU Press. [14] McKay G. et al. (1986) GCA *50,* 927-937. [15] Lindstrom D.J. (1983) *GCA 47*, 617-622. [16] Giguere et al. (2000) *Meteorics and Planet. Sci., 35,* 193-200. [17] Gillis J.J. and Jolliff B.L. (2003) *JGR,* 108, No. E2, 5009. [18] Delano J.W. (1990) *LPSC XXI*, 276-277.

The deep water abundance on Jupiter as derived from thermochemical kinetic modeling

S. Saslow[1], C. Visscher[2], and J. Moses[2]
[1]University of Maryland, College Park, MD, [2]Lunar and Planetary Institute, Houston, TX.

Introduction: The deep water abundance of the Jovian atmosphere provides helpful clues to solar system formation, its evolution, and the conditions of the solar nebula at the time of giant planet formation [1]. However, current remote sensing techniques are unable to probe the deep atmosphere due to cloud and opacity sources that reside at higher altitudes. The Galileo entry probe provided direct measurement of Jupiter's atmospheric composition; but only obtained data to 20 bars into the atmosphere before the probe's destruction. At this depth the deep water abundance may not have been obtained, as the probe entered an anomalous hot spot that was meteorologically different from the bulk of the planet.

Attempts to obtain data representative of the bulk Jovian atmosphere are planned with the Juno mission set to arrive at Jupiter in 2016. The onboard microwave radiometer may provide the best opportunity for measuring the Jovian deep-water abundance; however, the data analysis will be limited by the multiple microwave opacity sources in the Jovian troposphere (i.e ammonia, hydrogen sulfide, and phosphine).

Since H_2O and CO are intimately related through chemical processes, we use a unique thermochemical kinetics and transport model to derive the H_2O abundance in the Jovian troposphere from infrared observations reported for CO [2].

Background: In planetary atmospheres several processes drive the atmosphere out of equilibrium, including photochemistry and atmospheric transport/ mixing. Photochemical interactions are disregarded in our model since the region under consideration is too deep for the UV photons to penetrate; disequilibrium due to rapid transport will be the central focus of our model. In the deep atmosphere, at temperatures greater than ~1000 K, thermochemical equilibrium governs the composition, since energy barriers for chemical reactions are easily overcome at such high temperatures. If gas parcels are transported to higher, colder altitudes these chemical reactions become slower and transport/mixing disequilibrium can occur.

Prinn and Barshay [3] were the first to model the overabundance of certain species in the troposphere due to strong convective motions. When these species are vertically mixed to higher, colder altitudes, the mixing rate can eventually surpass the chemical kinetic destruction rate, quenching the species' abundance. Based on this notion of quenched values, several investigators [2-5] have used chemical kinetics and transport time scale arguments to calculate the predicted CO abundance in the upper troposphere dependent on the deep water enrichment. However, it is now known that the rate coefficient used in the scheme originally proposed by Prinn and Barshay is incorrect [2, 6-8], requiring revision of all models that use the Prinn and Barshay scheme.

In our model we will test the validity of the time scale arguments by developing a complete chemical kinetics and transport model to form a theoretical representation of the transition from thermochemical equilibrium to the quenched equilibrium in the upper troposphere. CO abundances calculated at varying water enrichment levels will be acquired from our model and will be compared to the observed CO abundance. The tropospheric water content can then be determined from the chemical behavior of CO.

Methods: Our model uses the Caltech/JPL KINETICS code [9] to calculate abundances as a function of altitude in Jupiter's troposphere. The KINETICS code uses finite-difference techniques to solve coupled continuity equations for all chemical constituents in the atmosphere. The pressure-temperature profile is fixed using data collected from the Galileo probe ASI data [10] and has been extended to deeper pressures and temperatures using an assumed adiabatic profile. Abundances are calculated for 144 different pressure levels between 1.265×10^4 and 17.9 bars, with a resolution of at least 20 levels per atmospheric scale height. A zero flux boundary condition is maintained at the top and bottom of the model.

The model includes 91 hydrogen, carbon, oxygen, and nitrogen species. Elemental abundances for H, He, C, and N are set using data acquired from the Galileo mission [11-13]. The oxygen abundance in the form of water is a free parameter, and a wide range of O/H ratios is considered to test its affect on the modeled CO abundance. The eddy diffusion coefficient (K_{eddy}) is our second free parameter; constraints are provided by free convection and mixing length theories described in [14].

The model contains 1800 reactions. All reactions are reversed using rate coefficients and the equilibrium constant by means of equation (1),

$$k_{for}/k_{rev}=K_{eq} \qquad (1)$$

Table 1. Predicted CO mole fractions using the Prinn and Barshay Model and this work ^.

H_2O Enrichment	**Prinn and Barshay[a]** $H_2 + H_2CO \rightarrow CH_3 + OH$ (Old Rate Coefficient)	**Prinn and Barshay[b]** $H_2 + H_2CO \rightarrow CH_3 + OH$ (New Rate Coefficient)	**This Work[c]** $CH_3O + H_2 \rightarrow CH_3OH + H$
4x Solar	12.6 ppb	240 ppb	3.0 ppb
2x Solar	6.3 ppb	120 ppb	1.5 ppb
1x Solar	3.1 ppb	59 ppb	0.8 ppb
0.55x Solar	1.7 ppb	32 ppb	0.5 ppb

^ Calculated for an eddy coefficient value of $4x10^8$ cm^2 s^{-1}. The actual observed CO abundance is 1 ± 0.2 ppb [2].
[a] Time constant approach, vertical mixing length (L) = H, k_{rxn}= $2.3x10^{-10}$ $exp^{(-36200/T)}$ cm^3 $molecule^{-1}$ s^{-1}.
[b] Time constant approach, vertical mixing length (L) = H, k_{rxn}= $(6.283x10^{-10})$ $T^{-0.694}$ $exp^{(-40761.20/T)}$ cm^3 $molecule^{-1}$ s^{-1}. Reaction rate calculated from [18] for the forward reaction $OH + CH_3 \rightarrow H_2 + H_2CO$
[c] Chemical kinetic model results, k_{rxn} = $(2.14 \times 10^{-22})T^{3.069}$ $exp^{(-3151.94/T)}$ cm^3 $molecule^{-1}$ s^{-1}.

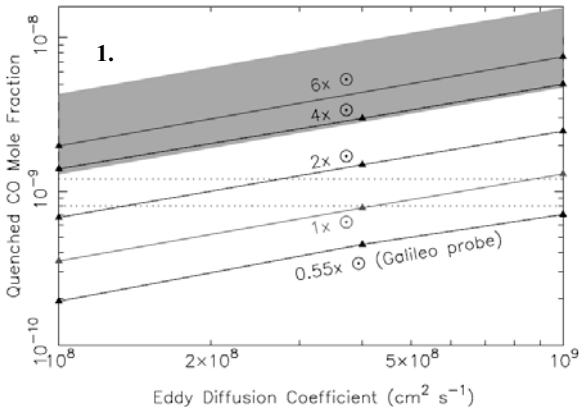

Figure 1. *The quenched CO mole fraction abundance versus the eddy diffusion coefficient (K_{eddy}) for H_2O enrichments of 4, 2, 1, and 0.55x solar; CO mole fractions were evaluated at K_{eddy} values of $1x10^8$, $4x10^8$, and $1x10^9$ cm^2s^{-1} (filled triangles). Higher K_{eddy} values represent more rapid mixing. The gray shaded region for the 6x solar H_2O abundance model represents the error bars due to uncertainties in the rate coefficient for reaction (4).*

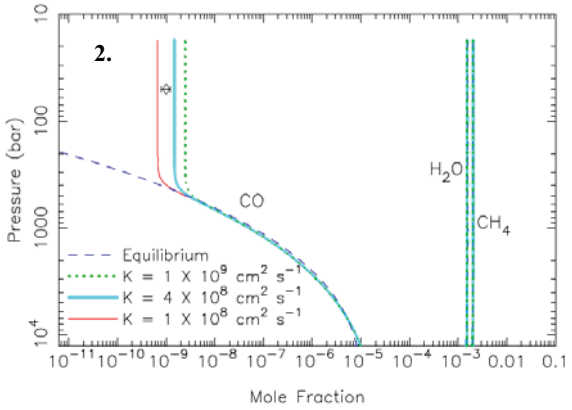

Figure 2. *The CO, H_2O, and CH_4 mole fractions as a function of pressure for an assumed 2x solar H_2O abundance and eddy coefficient values of $1x10^8$, $4x10^8$, and $1x10^9$ cm^2s^{-1}. The graph is oriented so the y axis increases with altitude. The dashed line represents chemical equilibrium, divergence shows where mixing drives CO out of equilibrium. The diamond with error bars represents the observed CO abundance reported by [2]. H_2O and CH_4 are the dominant C- and O- bearing gases, respectively, throughout Jupiter's deep troposphere.*

where k_{for} is the rate coefficient for the forward reaction, k_{rev} is the rate coefficient for the reverse reaction, and K_{eq} is the chemical equilibrium constant. Thermodynamic parameters for calculating K_{eq} are taken from the thermodynamic compilations of [15-17]. The atmospheric levels evaluated in our model extend too deep for ultraviolet photons to penetrate, so photolysis reactions are ignored. Our model is run until a steady state is achieved and results do not change between successive model iterations.

Results and Discussion: Prinn and Barshay [3] originally suggested the rate-limiting reaction that controls the conversion of CO to CH_4 is

$$H_2 + H_2CO \rightarrow OH + CH_3, \qquad (2)$$

and they estimated that this reaction has a rate coefficient of $2.3x10^{-10}exp^{(-36200/T)}$ cm^3s^{-1}. Using chemical kinetic and mixing time scale arguments, and assuming that the equilibrium abundance is quenched when the mixing time scale becomes less than or equal to the kinetic timescale for reaction (2), Prinn and Barshay [3] were able to predict the CO abundance on Jupiter. However, the reverse of reaction (2) has now been measured [18], and the forward rate coefficient estimated by [3] is several orders of magnitude too large [see also 6]. Table 1 shows how the original estimate of the CO abundance changes when the new rate coefficients are adopted.

Yung et al. [7], suggest that reaction (2) proposed by Prinn and Barshay is "kinetically too ambitious" because of the abrupt breaking of the strong CO

double bond. Yung et al. propose an alternative scheme to reduce carbon:

$$H + H_2CO + M \rightarrow CH_3O + M \quad (3)$$

$$CH_3O + H_2 \rightarrow CH_3OH + H \quad (4)$$

$$CH_3OH + H \rightarrow CH_3 + H_2O \quad (5)$$

where reaction (3) is assumed to be the rate limiting step. Bézard et al. [2] use the Yung et al. scheme when determining their predicted CO abundance based on the time constant arguments. However, using the theoretical arguments of Smith [8], Bézard et al. also point out that for CO mixing on Jupiter, the vertical length scale *L* that should be used in the time constant calculations is not the pressure scale height *H* (as assumed by [3]), but a smaller length scale that amounts to ~10% of the pressure scale height. Using reaction (3) as the rate limiting step, Bézard et al. [2] calculate a range of 0.2-9x solar for the deep water enrichment.

Based on our full kinetic/transport model, we agree that carbon is reduced by Yung et al.'s proposed scheme; however, our results indicate that reaction (4) is the rate limiting step. Using a fixed eddy diffusion coefficient of $4x10^8 cm^2s^{-1}$ for our nominal model, we find that an H_2O abundance of ~1.3x solar (where solar $H_2O/H_2=8.96x10^{-4}$) best reproduces the observed CO abundance [2]. When we consider a possible range of 10^8-$10^9 cm^2s^{-1}$ for K_{eddy}, our results expand to 0.55-4x solar for the deep H_2O abundance, as illustrated in Figure 1. An increase in the eddy diffusion coefficient increases the observed CO abundance because quenching occurs at higher temperatures, deeper in the atmosphere where there is a greater CO abundance. The CO abundance is also dependent on the H_2O abundance, with an increase in the H_2O abundance leading to an increase in the quenched CO abundance.

The rate coefficient for the reverse of reaction (4) has been calculated by Jodkowski et al. [19] using transition-state theory. No uncertainties were given by [19]. Based on theory- data comparison for similar reactions, we estimate that the rate coefficient of reaction (4) is uncertain by a factor of ~5, which expands our prospective range for the H_2O enrichment to 0.55-6x solar, with the lower limit being fixed by the Galileo probe data [13]. Rate coefficients affect the CO abundance because slower rates cause quenching to occur deeper in the atmosphere where the CO abundance is larger. Our proposed range falls within the water enrichment range of 0.2-9x solar put forward by [2] and includes the H_2O abundance measured by the Galileo entry probe [13].

Our model results in Figure 2 demonstrate the pressure at which the CO equilibrium abundance is quenched. At pressures greater than the quench level, our model provides a reasonably consistent representation of equilibrium.

Conclusion: In this novel chemical kinetic modeling approach, we are able to model the CO abundance in the Jovian deep atmosphere using plausible assumptions about the eddy diffusion coefficient. Based on observed CO as reported in Bézard et al. (2002) and taking into account uncertainties in the eddy diffusion coefficient and rate coefficients of the rate limiting reaction, we find that the deep water abundance must have a range of 0.55-6x solar in order to reproduce the observed CO abundance. This range better constrains the deep water enrichment from the previously published values [2] and encompasses the Galileo probe value. With these values the clathrate hydrate hypothesis initially proposed by [20] is invalidated. We also find that the time-constant estimation method is valid when using the vertical mixing length advocated by Smith [8] and reaction (4) as the rate limiting step.

References:

[1] Lunine, J.I., et al. (2004) *Jupiter: The Planet, Satellites, and Magnetosphere.* 19-34. [2] Bézard, B., et al. (2002) *Icarus, 159,* 95-111. [3] Prinn, R.G., Barshay, S.S. (1977). *Science, 198,* 1031-1034. [4] Fegley, B., Jr., Prinn, R.G. (1988) *Astrophys. J., 324*, 621. [5] Fegley, B., Jr., Lodders, K. (1994) *Icarus, 110*, 117- 154. [6] Griffith, C.A., Yelle, R.V. (1999) *Astrophys. J. 519*, L85-L88. [7] Yung, Y.L., et al. (1988) *Icarus, 73,* 516-526. [8] Smith, M.D. (1998) *Icarus, 132,* 176-184. [9] Allen, M., et al. (1981) *JGR, 86,* 3617–3627. [10] Seiff, A., et al. (1998) *J. Geophys. Res., 103,* 22,857-22,889. [11] Niemann, H.B., et al. (1998) *J. Geophys. Res., 103,* 22831. [12] von Zahn, U., et al. (1998) *J. Geophys. Res., 103,* 22815 [13] Wong, M.H., et al. (2004) *Icarus, 171,* 153. [14] Stone, P.H. (1976) In: Gehrels, T., Mathews, M.S., (Eds.), Jupiter. Unive. Arizona Press, 586-618. [15] Gurvich, L.V., et al. (1989-1994) *Thermodynamics Properties of Individual Substances 4th ed., 3 vols.* Hemisphere Publishing, New York, 4th edition. [16] Burcat, A. and Ruscic B. (2005) *Third Millenium Ideal Gas and Condensed Phase Thermochemical Database for Combustion with updates from Active Thermochemical Tables, ANL - 05/20 and TAE960.* [17] Chase M. W. (1998) *J. Phys. Chem. Ref. Data, 28,* monograph #9. [18] Dean, A. M., & Westmoreland, P. R. (1987) *Int. J. Chem. Kinetics, 19,* 207. [19] Jodkowski et al. (1999) *J. Phys. Chem. A., 103,* 3750-3765. [20]Gautier et al. (2001) *Astrophys. J., 550,* L227-L230.

THE MINERALOGY, PETROGRAPHY AND CHEMISTRY OF COMET DUST: SULFIDES.

Chisato Sekigawa[1] and Lindsay P. Keller[2],
[1]Faculty of Science, Kobe University, 1-1, Rokkodai, Nada-ku, Kobe JAPAN 657-8501,
098s415s@stu.kobe-u.ac.jp, [2]ARES, Mail Code KR, NASA Johnson Space Center, Houston, TX 77058

Introduction: Interplanetary dust particles (IDPs) are among the most chemically and mineralogically primitive meteoritic materials currently available for laboratory investigation, with components that formed in the early solar nebula and presolar environments [e.g. 1, 2]. IDPs contain some of the fundamental 'building blocks' of our solar system, and their study can provide insights into early solar system processes.

Advances in analysis techniques have allowed us to obtain ancient solar system information from such comet dust samples. The particles are typically 5-15 μm in diameter, 10^{-12} – 10^{-9} grams in the mass and collected in the stratosphere at 20-25 km altitude using high-flying NASA aircraft.

There are two major types of chondritic IDPs, chondritic porous (CP) IDPs and chodritic smooth (CS) IDPs and the former are anhydrous and the latter are hydrous CP IDPs are composed predominantly of loose fluffy aggregates of submicrometer silicates (En, Fo), FeNi sulfides, GEMS (glass with embedded metal and sulfides), and carbonaceous material [1].

The mineralogy and petrography of CP IDPs have been studies for over 2 decades, yet few systematic studies have been reported. One of the goals of this study was to determine the mineralogy, mineral compositions and grain sizes for several CP IDPs in order to provide a database for comparison with other primitive meteoritic materials such as carbonaceous chondrites and Stardust samples (comet Wild-2 particles). Our initial measurements focused on the sulfide grains within these particles.

Sulfur is an abundant rock-forming element in meteoritic materials and is one of two major elements that are strongly fractionated among the various classes of chondritic meteorites. Although sulfides are a common mineral in IDPs, details of their composition (and crystal structures) have remained elusive. Most of the sulfur in primitive meteoritic materials resides in Fe,Ni-sulfide grains in the form of troilite (FeS)), pyrrhotite ($Fe_{1-x}S$), and pentlandite ($[Fe,Ni]_9S_8$) [1]. In this study, we analyzed the sulfide mineralogy of the particles and compared our data to other primitive materials such as carbonaceous chondrites and comet Wild 2 samples.

Sample and methods: Three individual CP IDPs (W7190C28, L2005AL5 and L2001B10) and matrix fragments from a meteorite (Acfer 094) were embedded in low viscosity epoxy or elemental sulfur and microtome thin sections (~70 nm) were prepared by ultramicrotomy. The IDP samples are typical CP IDPs, while the Acfer 094 matrix samples were selected because this meteorite is among the most primitive carbonaceous chondrites in terms of its content of presolar grains [3]. The thin sections were placed on TEM grids with continuous carbon films and analyzed using the JSC JEOL 2500SE scanning-transmission electron microscope (STEM). Brightfield and darkfield images of the thin sections were taken at 100KX magnification and were used to aide in the identification of the individual grains. We obtained quantitative elemental maps (spectrum images) of the samples using a Noran thin-window energy dispersive X-ray spectrometer (EDX) to determine the chemical composition of the mineral phases (Fig. 1). We also measured particle size sizes of the different minerals by image processing of the elemental images using a publicly available software packge (Image J, from the NIH)(Fig.1).

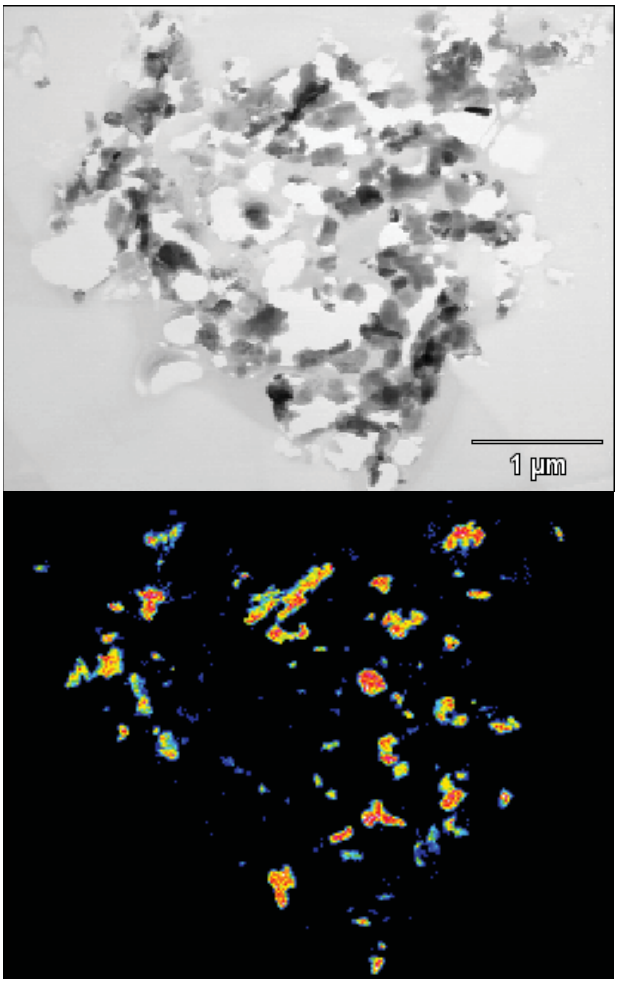

Fig. 1: upper: BF (bright field) image of W7190C28 thin section, lower: X-ray map of sulfur in W7190C28

Results: Each IDP shows somewhat different characteristics; **W7190C28**: This is ~4 um porous particle that contains abundant Mg-rich crystalline silicates and sulfide grains, carbonaceous materials and rare GEMS grains. We identified 115 sulfide grains in the X-ray maps of one complete thin section. The sulfides grains range in size from 5 nm up to 360 nm. The sulfide compositions are consistent with low-Ni pyrrhotite with typical Ni contents of ~5 at. %. Several of the sulfide grains in the thin section are aggregates of 2-5 individual crystals. **L2011B10**: This is another ~4 um porous particle and also contains Mg-silicate grains and sulfides and carbonaceous materials. In contrast to W7190C28, B10 contains abundant GEMS grains. We observed 486 sulfide grains ranging in size from ~5 to 400 nm. The sulfide grains are very similar to those in W7190C28 although the pyrrhotite grains tend to be Ni-poor compared to W7190C28. **L2005AL5**: This is the largest IDP in this study ~8 um. AL5 contains abundant GEMS, Mg-rich silicate, and sulfide grains dispersed in a carbonaceous matrix. The sulfides show a wider range in sizes compared to the other IDPs in this study. We identified 513 sulfide grains and they contains highest % of Ni (~15 at. %) among these three IDP samples. In addition, AL5 also contains tiny Fe metal (kamacite) Grains. **Acfer 094**: We analyzed an ~10 um sized fragment of the fine grained matrix. This sample contains abundant amorphous Mg-Fe silicates, tiny enstatite and forsterite grains along with numerous sulfide grains (carbonaceous materials is rare) [4]. We identified 274 sulfide grains in this sample with size ranges up to ~500 nm. Unlike the IDP samples, Acfer 094 matrix contains Ni-rich sulfides (pentlandite) in addition to pyrrhotites.

Figure 2 shows the size distribution of sulfide grains for each sample. L2011B10, L2005AL5 and Acfer 094 all show similar trends. These samples show an approximately log-normal size distribution with a maximum peak at 10 nm. W7190C28 shows a much different distribution with a much wider distribution of sizes with few small grains and more grains in the larger size fraction.

Figure 3 shows Fe-Ni-S atomic % ternary diagram. We analyzed mineral composition for 20, 20, 19 and 50 sulfide grains for W7190C28, L2011B10, L2005AL5 and Acfer 094, respectively. The three IDP samples contain pyrrohtite which is the usual trend for anhydrous IDPs [5,6]. Sulfide grains in W7190C28 and L2011B10 are generally Ni-poor (<5 at. %) and these data plot close to the S-Fe binary join. L2005AL5 contains more Ni-rich (~15 at. %) grains compared to the other two IDP samples. The data show that there are also some Fe metal grains (kamacite) in AL5. Acfer 094 shows broader compositional range compared to all IDP samples. This meteorite sample includes much more sulfide grains that contain higher component of Ni (~20 at. %) than the other three samples.

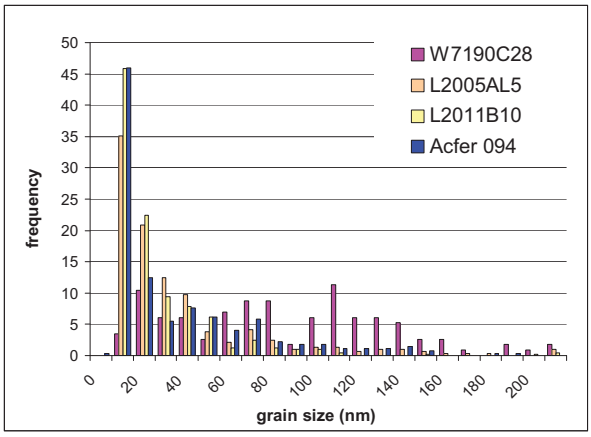

Fig. 2: Size distributions for the three IDP samples and one meteorite sample.

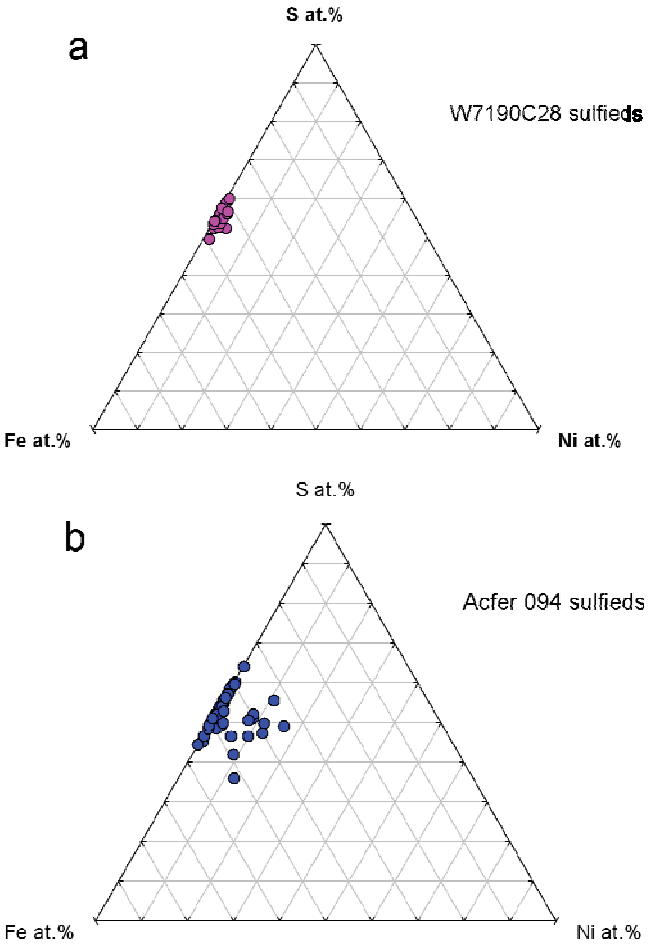

Fig.3: Fe-Ni-S atomic % ternary diagram a) W7190C28 (anhydrous IDP), b) Acfer 094 matrix (meteorite).

Discussion: Our grain size distributions are consistent with earlier results by [4]. However, there is an obvious difference between W7190C28 and other three samples. The larger grains sizes and abundance of polycrystalline sulfide aggregates in W7190C28 could be caused by annealing and growth of sulfide grains in solar nebula. Coagulation and grain growth has modified the mineralogy and grain size of the silicate aggregates in W7190C28 [3].

Mineral composition of sulfide grains

The compositions of the sulfide grains analyzed in this study are in excellent agreement with a previous study of IDP sulfide grain compositions [1, 4]. Zolensky and Thomas [5] analyzed anhydrous (CP) and hydrous (CS) IDPs and their Fe-Ni-S atomic % ternary diagram show that anhydrous IDPs contain mainly low-Ni (<2 at.%) pyrrhotite. In contrast, their hydrated IDPs contained mainly pyrrhotite plus more Ni-rich varieties including pentlandite. In this study, we found that Acfer 094 matrix sulfides show the same trends as the hydrous IDPs from [5]. Zolensky and Thomas [5] proposed that the Ni-rich sulfides in CS IDPs were produced during an aqueous alteration event on the parent body, while the CP IDPs sulfides reflect an origin in the early nebula. Although the range of aqueous alteration in Acfer 094 is not as pronounced as in the CS IDPs, the sulfide compositions reflect a similar elemental redistribution.

Comparison to comet Wild 2 sample

Zolensky at al. [6] plotted Fe-Ni-S atomic % ternary diagram of comet Wild 2 samples. A plot of analyses of its Fe-Ni sulfides shows that many have composition close to that of FeS, with less than 2 atom % Ni (two pentlandite grains are exceptions). Basically, most Wild 2 sulfides are mixture of troilite and pyrrhotite. The Fe-Ni sulfide compositional range of Wild 2 grains is the same as that of anhydrous chondritic IDPs in this study.

Conclusions: Detailed analyses of the sulfide grain compositions and their size distribution within a set of IDPs and one primitive carbonaceous chondrite reveals evidence for thermal processing in the early solar nebula and aqueous alteration on parent bodies. Thermal annealing of tiny individual sulfide crystals resulted in the coarse-grained polycrystalline sulfide grains now observed within IDP W7190C28. The Ni-rich sulfides observed in Acfer 094 matrix likely have a similar origin as those in CS IDPs that formed in response to aqueous activity on their parent bodies.

Acknowledgements: I would like to thank Lindsay Keller for giving me this opportunity and working with and helping me through this summer. I also want to thank Keiko Nakamura-Messenger for all her support. And I appreciate Scott Messenger, Roy Christofferson, George-Anne Robinson, Kent Ross and Motoo Ito to provide me with great life in JSC, and thank you for all LPI interns 2009 to share the time.

References: [1] Dai, Z. and Bradley, J. P. (2001) *GCA* 65, 3601-3612. [2] Keller, L. and Messenger, S. (2007) *MAPS* 42, #5297. [3] Nguyen, A. et al. (2007) *Ap.J.*, 656, 1223. [4] Keller, L. et al. (2009) *LPSC* 40, #5371. [5] Zolensky, M. and Thomas, K. (1995) *GCA* 59, 4707-4712. [6] Zolensky, M. et al. (2008) *MAPS* 43, 261-272.

Assessment of a Handheld Forward Looking Infrared Camera as a Potential Lunar Field Geology Tool. K. Shimizu[1],W.L. Stefanov[2], C.A. Evans[2] [1]Department of Geosciences, Stony Brook University, Stony Brook, NY 11794 (keshimiz@ic.sunysb.edu), [2]Astromaterials Research and Exploration Science Directorate, NASA Johnson Space Center, Houston, TX 77058 (william.l.stefanov@nasa.gov; cindy.evans-1@nasa.gov).

Introduction: The Bush Vision for NASA included human missions to the moon by 2020. [1] NASA currently plans to construct a lunar outpost by 2024. Such an effort will require astronaut and robotic tools for rapid surface assessment relevant to base construction and field activities. In particular, mapping of rock and regolith abundance at the field scale will augment and validate orbital image data of the lunar surface.

Thermophysical measurements of surface materials have been used to map rock abundance on both the lunar surface and Mars, taking advantage of the differences in thermal inertia resulting from particle size variations in similar rock and soil compositions. [2, 3] The majority of lunar soil samples fall in a fairly narrow range of particle size distribution. In general soil is well graded, silty sand to sandy silt. The median particle size is 40 to 130 microns with an average of 70 microns. In contrast there are sites that have a high block concentration for example the rim of fresh craters such as South Ray Crater visited during the Apollo 15 mission. [4] By recording the temperature of materials on the lunar surface at appropriate times to maximize thermal contrast in differing particle sizes, it should be possible to rapidly map the geological environment at a site.

Forward Looking Infrared (FLIR) cameras are a class of commercial off-the-shelf instrument that suits this purpose while having a broad range of potential discovery and operational applications. FLIR cameras record surface temperature in both still and video formats, with certain models able to simultaneously take visible image data. Fusion of the thermal infrared (TIR) and visible wavelength data provides the potential to develop classification algorithms for dust/regolith/rock abundance characterization. The technology also has potential for engineering purposes, such as habitat damage and leak assessment.

There have been extensive TIR studies done on Earth, Moon, and Mars from orbit, however there are few high resolution field studies using FLIR cameras. [5-7] Most of these field studies have focused on the use of diurnal thermal inertia measurements to obtain particle size and compositional information, but such an approach during lunar field operations is impractical due to the length of the lunar diurnal cycle. Understanding of field scale thermal measurements will be useful to validation and enhancement of expected LRO Diviner surface temperature, rock abundance, and mineralogical maps.

The primary goal of this study is to assess the usefulness of FLIR cameras in determining rock abundance for geologic hazard assessment, and to develop data collection procedures appropriate to lunar surface sorties. To this end, design and testing of classification algorithms for fused visible and thermal infrared wavelength images were performed. FLIR thermal infrared and visible camera data were collected from two Lunar/Martian analog field sites: a basaltic boulder field at the "rock yard" at Johnson Space Center in Houston, TX; and Colton Crater, a basaltic maar crater in the San Francisco volcanic field north of Flagstaff, AZ.

Methodology: The instrument used for field data collection is a 640x480 pixel microbolometer thermal infrared camera model P660 manufactured by FLIR systems. This model camera is also equipped with a coregistered 3 megapixel visible wavelength (RGB) digital camera. The camera was mounted on a stable tripod on the ground at each site location. Environmental conditions, camera angle from horizontal, height above the ground, and distance to the target surface was recorded. The thermal measurement of materials in the FLIR field of view (FOV) were confirmed by independent measurement of selected surfaces using a FLUKE hand held infrared spot radiometer.

Simultaneous visible and TIR images were acquired for each site at 5 minute intervals from roughly 8:30AM until noon. This time interval was chosen because the predawn-to-midday variations of surface temperature can be interpreted in terms of apparent thermal inertia of materials in the scene, which are, in turn, a function of the thermal conductivity, bulk density, and specific heat of the surface material. [3] The appropriateness of morning data collection was also indicated by observations of apparent thermal inertia during timed illumination of simulated lunar surfaces under laboratory conditions performed at JSC. [8]

The visible (VIS) and TIR data were fused together as a stacked 4–band image within the ENVI software environment following coregistration of the two datasets. Principle component (PC) analysis was performed for the VIS and stacked (VIS+TIR) images in order to obtain the most correlated data and reduce the noise, and to assess the benefit of using PC analysis results for classification. This resulted in five different image sets for each site: VIS, PC VIS, TIR, VIS+TIR, PC VIS+TIR.

Image sets for the field sites were classified using unsupervised K-means and supervised maximum likelihood classification methods. [9, 10] While classifications using different numbers of classes for each site were performed, we report only the 5-class results here as representing the limits of the approach for the FLIR data. The accuracy of classification results were assessed using 20 reference points for each class selected by a stratified random approach. The "true" class identity of each reference point was determined using the visible data for each site. Error matrices were then constructed for the field site classifications using the appropriate reference dataset.

Results: *Unsupervised classification.* For the JSC basalt boulder field (JSC-S1) the overall accuracy of the unsupervised classifications (five classes) ranged from 35.00% to 59.00%. Producer accuracy is the probability that a pixel in the classification image is put into a given class given the ground truth class is the same. User accuracy is the probability that the ground truth class is the same as a given pixel in classification image. [10] For the dark basalt class the producer accuracy ranged from 22.22% to 94.44% and the user accuracy ranged from 26.67% to 80.00%. The accuracy of the unsupervised classifications of the Colton Crater basalt boulder/gravel subsite (CC-S1) ranged from 43.00% to 80.00%. For the basalt boulders class the producer accuracy ranged from 66.67% to 100% and the user accuracy ranged from 50.00% to 85.00%. The accuracy of the unsupervised classifications of the Colton Crater basaltic agglutinate outcrop subsite (CC-S2) ranged from 33.00% to 77.00%. For the dark basalt/agglutinate class the producer accuracy ranged from 38.10 % to 85.71% and the user accuracy ranged from 21.05% to 85.71%.

Supervised Classification. For JSC-S1 the overall accuracy of the supervised classifications ranged from 40% to 85%. For the dark basalt class the producer accuracy ranged from 33.33% to 95.24% and the user accuracy ranged from 87.50% to 100%. The accuracy of the supervised classifications of CC-S2 ranged from 47.00% to 84.00%. For the black rock class the producer accuracy ranged from 36.36% to 86.36% and the user accuracy ranged from 29.63% to 95.00%. For the fine soil class the producer accuracy ranged from 46.15 % to 69.23% and the user accuracy ranged from 50.00% to 85.71%. We present the full accuracy results for supervised classifications of CC-S1 in Table 1 as being representative of results for all three sites. A representative classification result for CC-S1 is presented in Fig. 1.

Discussion: In terms of overall differentiation of rocks and regolith both classification methods (raw data and PC data) perform well. However, classification of materials of different compositions of rock or soil is less effective. At JSC-S1sub-pixel mixing in the VIS data of high albedo granitic gravel (white feldspar and gray quartz) with shadows resulting in effectively gray pixels that were confused with, and misclassified as, underlying fine soil. Thermal variations in the TIR confirmed this misclassification. Since the reference dataset was constructed using the VIS image, the classification accuracy was low for the fused VIS+TIR data as well, despite a seemingly high qualitative accuracy of soil classification.

Both unsupervised and supervised classifications for JSC-S1 differentiated between basaltic boulders and other classes well using the VIS data. This is due to high color contrast between black basalt and light-colored gravels and soil. User accuracy of su-

	Rock Basalt	Gravel	Shadow	Welded Material	High Albedo Material
VIS OA = 87	90/90	79/95	100/ 100	87/65	81/85
VIS PC OA = 87	90/90	79/95	100/ 100	87/65	81/85
TIR OA = 35	25/50	46/ 31	40/100	13/22	43/24
VIS+TIR OA = 55	35/100	79/ 59	65/100	13/50	67/32
VIS+TIR PC OA = 55	35/100	79/59	65/100	13/50	67/32

Table 1. Accuracy assessment results for CC-S1 supervised classifications. Raw data were classified as recorded by the FLIR camera; PC indicates that principle components of the raw data were used for classification. Individual class results are reported as producer/user accuracy. OA is overall accuracy. All values are percentage correct.

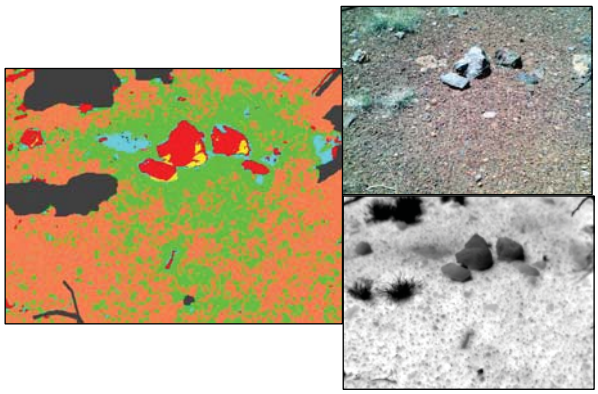

Figure 1. Result of maximum likelihood classification using VIS+TIR base data for CC-S1. Red – Rock Basalt; Pink – Gravel; Yellow – Shadow; Green – Welded Material; Blue – High Albedo Material. Gray regions are masked vegetation. The VIS (upper right) and TIR (lower right) data are provided for comparison.

pervised TIR and VIS+TIR classifications are relatively high (87% - 100%) in discriminating basaltic boulders from other materials at the site, suggesting that this classification approach would be useful in exploration of lunar sites with significant color contrast.

In contrast to JSC-S1, the primary variation at CC-S1 (Fig. 1) was due to particle size and is perhaps more representative of a lunar surface. This is the only site where the accuracy of unsupervised classification based on the TIR data alone was higher than that based on the VIS or VIS+TIR. The cause of this high accuracy is to some extent due to the high contrast in the thermal data between basaltic boulders, gravel, and associated soil, but also because of the method of accuracy assessment. Basaltic gravels have same albedo as basalt boulders but lower thermal inertia, thus they have higher temperature. This resulted in the opposite accuracy of basalt rock classification in the supervised runs, as a reference dataset based on visible information only was used.

The supervised classification results using the VIS+TIR data did not have good overall accuracy, but user accuracies of 100% for basaltic rock were obtained. While this would seem to be an excellent result, the low performance of other classes suggests that more sophisticated classification and assessment approaches may be needed. The basaltic boulder abundance in the camera FOV was estimated to be ~6% in the field, and the percentage obtained from classification results was 5.197%. This does not prove the accuracy of the classification, but supports the core assumption that FLIR cameras can provide useful field information for lunar site assessment.

Site CC-S2 had relatively low contrast in albedo, while the thermal data had a high contrast ranging from fine soil (relatively hot) to bedded dark basalt agglutinates (relatively cool). This is the only data set that had an increased accuracy of unsupervised classification by fusing the VIS and TIR data. Fusion of the thermal data is a simple stacking of images, essentially adding a fourth grayscale band to the visible data. Ideally the spectral contrast between all materials would be enhanced by fusing the VIS with the TIR data. This was generally not the case at our sites as the albedo and thermal inertia are not strongly correlated with each other. In the case CC-S2, the rock outcrop had low temperature while the relatively high albedo fine soil had high temperature. Thus the fusion of the VIS+TIR data resulted in a high contrast between the rock outcrop and adjacent fine soil. Depending on the training region selected for supervised classification, fusing the TIR and VIS images can either help or worsen the classification accuracy. Training regions should be selected so the contrast is maximized between classes.

The FLIR camera has only four bands and the spectral quality of these bands is not ideal. The visible camera bands likely have significant bandpass overlap (based on other off the shelf visible cameras), and the thermal information is broadband (7.5-13 microns). A multispectral VIS/TIR instrument with narrower bandwidths would undoubtedly improve the capacity for fine discrimination of materials. More sophisticated classification methods may help alleviate some of the limitations of the current FLIR instrument. For example, classification results can be segmented to exclude well-classified results and reduce variability for further iterative classification of other classes. Decision trees could also be used by incorporating data such as textural analysis of visual data using co-occurrence measures, digital elevation data, or geologic maps [10].

Conclusion: Our initial assessment indicates that while current FLIR microbolometer cameras show strong potential in obtaining useful information for lunar field studies and hazard assessment - rock abundance determination in particular - the accuracy of identification for other geological materials can be improved significantly. The best overall accuracy of classification was higher than 80%, however individual class accuracies were highly variable and generally lower. Unsupervised classifications performed fairly well, but operationally this would require data transmission to a "back room" for analysis. In order to improve the potential for this class of instrument 1) more complex classification methods should be explored, 2) true coregistration of the visible and thermal data streams is necessary, and 3) an increase in the number of thermal bands, and use of narrow bandwidth visible data would improve material discrimination capability.

References: [1] G.W. Bush, A Renewed Spirit of Discovery: The President's Vision for U.S. Space Exploration (2004). [2] H. H. Kieffer *et al.*, *J. Geophys. Res.* 82, 4249 (1977). [3] Edgett, K. S., and P. R. Christensen, *J. Geophys. Res.*, *96*, 22,765–22,776, (1991). [4] G. Heiken, D. Vaniman, B. French, Lunar Sourcebook: A User's Guide to the Moon. (Cambridge University Press, 1991), p. 478. [5] Moersch. J.E. (2008) *International Conference on Mars,* Abstract #3355. [6] Byrnes. J.M, Ramsey. M.S. Anderson. S.W, Prade. K.C, Finnegan. D.C., (2008) *LPS XXXIX,* Abstract #1988. [7] Hardgrove. C, Whisner. S.C, Moersch, J.E., (2008) *LPS XXXIX,* Abstract #1226. [8] W.L. Stefanov, personal communication (2009). [9] Tou J.T. and R.C. Gonzalez, Pattern Recognition Principles (Addison-Wesley Publishing Company, 1974). [10] J.R. Jensen, Introductory Digital Image Processing: A Remote Sensing Perspective 2nd Ed. (Prentice Hall, 1996).

MAPPING THE MAGMATIC PLUMBING SYSTEM IN THE MARIUS HILLS

Nattavadee Srisutthiyakorn[1], Walter S. Kiefer[2], and Michelle Kirchoff[2]; [1]Dept. of Geological Sciences, University of Michigan, 1100 North University Ave., Ann Arbor MI 48104, (natts@umich.edu) , [2]Lunar and Planetary Institute, 3600 Bay Area Blvd., Houston TX 77058, (kiefer@lpi.usra.edu, kirchoff@lpi.usra.edu).

Introduction: The Marius Hills stand out as it is the most unique volcanic field plateau on the Moon. The plateau is located in the south-central part of the Oceanus Procellarum region and appears to be Eratosthenian in age. In a region 250 km across, the Marius Hills contain about 300 volcanic domes and cones [1], which is about half of the total number of volcanic domes on the entire Moon [2]. In comparison, the Rumker Hills, which has the second largest abundance of volcanic domes on the moon, contains only 30 domes within an 80 km diameter [3]. Clementine multispectral imaging shows that the Marius Hills volcanoes are basaltic, similar in composition to the surrounding mare plains [4,5]

In this study, physical measurements including diameter and location of volcanic domes were collected. These measurements were used to make a spatial analysis for the distribution of volcanic domes in the study region. The results were compared with a recent gravity study [6], which suggests that the Marius Hills were fed by two magma chambers, located near 13 North, 307 East and 8 North, 309 East. The overall goal of the combined geological and geophysical analysis is a better understanding of the magmatic plumbing system that supplied this volcanic complex. We also compare out results with measurements of six large volcanic dome fields on Venus, selected from the fields studied by *Addington E. A.* [7].

Methodology: For Marius Hills, the initial data gathering was done on Lunar Orbiter images by utilizing ISIS, the image processing software package by USGS. For better visualization and more accurate measurements, some of the images were stretched according to their original brightness and contrast. Because of the irregular morphology of the Marius Hills' volcanoes, we used four lines through the center of each volcano to define the size and location of each volcano. We subsequently used the average length of the four lines as the volcano diameter and the average center of the four lines as the volcano center. The examples for measurements and boundary justification are displayed in figure 1. Because of limits on the resolution of Magellan radar mosaics, the edges of the volcanic domes on Venus are often difficult to define. We therefore measured just the volcano center and not the diameter for these structures.

The boundary of each dome is defined at the clear edge of the volcanic structure. If the structure is not well defined, then a boundary would be drawn at the abrupt change in albedo. This procedure would conserve the size of each dome to the minimum amount. In addition, if there are variations in morphology of the volcanic features, only the one largest feature would be counted. This method of counting, in turn, reduces the number of volcanic domes measured in this study and contributes to the discrepancy in the number of volcanic domes between this study and *Whitford-Stark and Head* [1].

We calculate the concentration of volcanoes as a function of location on the map grid

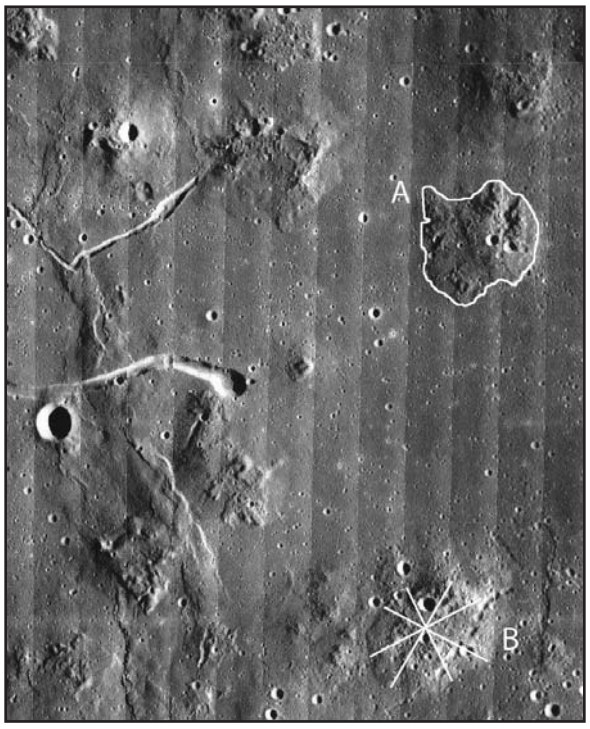

Figure 1. (A) An example of boundary of volcanic dome. (B) An example of measurements obtained from each volcanic dome.

using the kernel method of *Weller J. N. et al* [8]. We use a Gaussian weighting function because it provides the high weight to volcanoes closest to a map point and smoothly decreases the weighting with increasing distance.

In the normal application of this method, volcanoes of all sizes are given equal weight in the calculation. For our lunar work, we have also explored a modified kernel method, in which each volcano is weighted by its area. Ideally, we would use volume rather than area for this calculation, but for most of these domes the heights are not yet well measured. For the Venus study, however, we did not have volcano diameters and thus could not weight volcanoes by size. Therefore we only report the concentration calculated from original Gaussian weighting function for better cross comparison between the Moon and Venus.

The center latitude and longitude were then used to calculate the spatial concentration of the volcanic domes. A grid is set up with the distance so that each point in the grid is equal to half a degree. For each point, the concentration is estimated using the Gaussian kernel. Gaussian equations would yield more weight to the volcanic domes that are adjacent to the grid point. The equation for calculating concentration is as followed:

$$\widehat{\lambda_s}(x,y) = \frac{1}{2\pi N h^2} \sum_{i=1}^{N} \exp\left(-\frac{1}{2}\left[\frac{d_i}{h}\right]^2\right)$$

where $\widehat{\lambda_s}$ is the estimated concentration at the particular grid point, N is the total number of volcanic features in the field, h is the kernel bandwidth, d_i is the distance from ith volcano to the grid in km [8].

Results: A total number of 239 lunar volcanic domes, with diameters ranging from 1 to 12 km, were measured, compared to 321 domes counted by *Whitford-Stark and Head* [1]. The discrepancy in the number of volcanic domes counted between this study and the previous study by *Whitford-Stark and Head* arises because of the differences in the definition of boundaries of the domes and counting procedure. The histogram showing the distribution of the volcanic domes' diameter is plotted in figure 2. The histogram is left-skewed with the mean of 4.16 km and the median of 3.91 km.

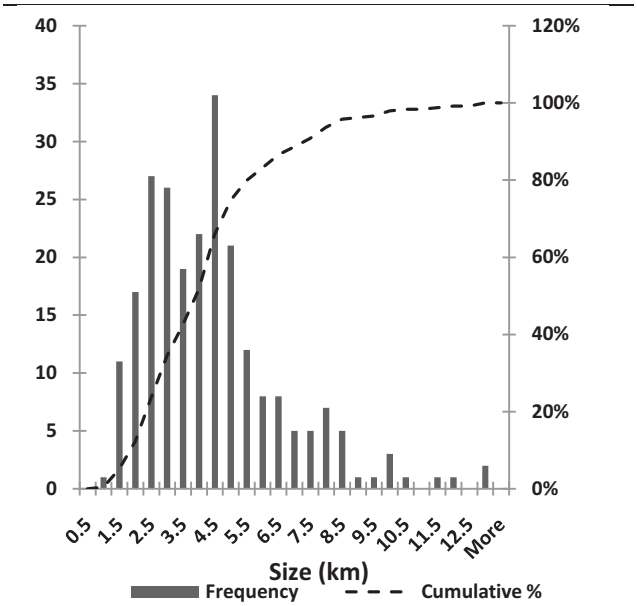

Figure 2. The distribution of sizes of volcanic domes in the Marius Hills. The mean is 4.16 km. The median is 3.91 km

The spatial concentration map of the Marius Hills volcanoes was plotted. When the concentration map is overlaid on the gravity map, two of the three local maximum concentation matches with gravity maxima. We speculate that utilizing the Gaussian kernel may not accurately represent the concentration of volcanic fields since it treats the small domes the same weight as the bigger one. This speculation leads to the following equation that will add the weight to the size of volcanic dome:

$$\widehat{\lambda_s}(x,y) = \frac{1}{2\pi N h^2} \sum_{i=1}^{N} \left(\exp\left(-\frac{1}{2}\left[\frac{d_i}{h}\right]^2\right) * \left(\frac{A_i}{A}\right)\right)$$

where A_i is the area of dome ith and A is the average area of volcanoes in the field.

As the kernel bandwidth corresponds to the search area, changing the kernel bandwidth in the equation would change the number of local maxima, which can be interpreted as the number of clusters (figure 3). The kernel bandwidth shows the inverse relationship with the number of clusters. However, the number of clusters converges to a particular number in some range of kernel bandwidth. The result shown in Tables 1 and 2 all use kernel bandwidth equls to 30 km, which is large enough to encompass the volcanic field and

yet small enough to exclude regions outside the field.

Table 1.
Maximum Concentration of Marius Hills on the Moon

	Latitude	Longitude	Concentration
North Lobe	14	307	3.031
West Lobe	12	305	2.479
South Lobe	7	309	0.484

Table 2.
Maximum Concentration of some volcanic fields on Venus

Latitude	Longitude	Concentration
25.75	318.875	$2.549 \cdot 10^{-5}$
32.875	14.5	7.502
-35	10.875	2.609
44.75	329.875	6.489
45.375	1.125	8.110
-73.25	106.25	8.923

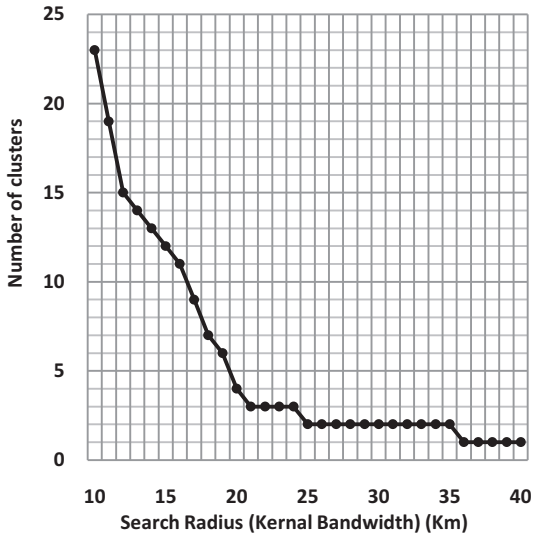

Figure 3. The number of clusters decreases as the search radius increases. The kernel bandwidth range is from 10 to 40. The number of clusters for each kernel bandwidth is defined as the number of local maximum intensity.

Discussion: For better understanding about the concentration of volcanic fields, we have compared our absolute concentration with *Wetmore et al* [9]. The relationship between absolute concentration and actual density of volcanic domes on both Marius Hills and Venus show resemblance with the concentration of volcanic domes on the Snake River Plain. In the Snake River Plain, the concentrations range from $3.0 \cdot 10^{-6}$ to $2.0 \cdot 10^{-4}$ [9]. Future work on the relationship between the concentration and density of volcanic domes could include plotting the countour plot of spatial density estimation with the locations of exposed vent.

For the Marius Hills, three local maximum concentrations show up in our spatial analysis that concur with the locations of topography high in the Marius Hills. However, the gravity data does not display the western lobe. If gravity maxima represents the location of magmatic chambers, it is interesting to question the magmatic system that fed the volcanic domes in the western lobe. This leads to future investigation about the role of dikes that may have fed this volcanic complex especially the western part. In addition, linear alignment analysis can be done to examine possible structural features that may have helped the migration of magma [10].

Reference:

[1] Whitford-Stark J. L. and Head J. W. (1977) *LPSC 8th*, 2705-2724.
[2]Head J. W. and Gifford A. (1980) *The Moon and the Planets*, 22, 235-258.
[3] Smith E. I. (1974) *The Moon*, 10, 175-181.
[4] Weitz C. M. and Head J. W. (1999) *JGR*, 14, 18933-18956.
[5] Heather D. J. et al. (2003) *JGR*, 108, E3.
[6] Kiefer W. S. (2008) *GSA Annual Meeting*, Paper 133-3.
[7] Addington E. A. (2001) *Icarus*, 149 , 16-36.
[8] Weller J. N. et al (2006) *Statistics in Volcanology*, 1, 77-87.
[9] Wetmore P. H. et al (2009) Preprint, 431-453.
[10] Lutz T. M. and Gutmann J. T. (1995) *JGR*, 100, 17659-17670.

The Smallest Lunar Grains: Analysis of the <1 μm Size Fraction of Lunar Mare Soil 10084

M. Thompson[1], and R. Christoffersen[2]
[1]Dept. of Geological Sciences and Engineering, Queen's University, Kingston, ON, Canada K7L 3N6
[1]ESCG, Mail Code KR, NASA Johnson Space Center, Houston, TX 77058

Introduction

The chemical composition, mineralogical type, and morphology of lunar regolith grains changes considerably with decreasing size and the smallest size fractions provide the strongest links to lunar space weathering processes [1]. Based on observed trends for the larger grain size fractions, it can be theorized that the <1 μm size fraction, a specific division which has not yet been systematically investigated, may be unique relative to larger grains. This study focuses on this particular size component of mare regolith sample 10084. Using analytical transmission electron microscopy (TEM) the prevalence of each component grain type within this sample was assessed, and their compositional trends analyzed. This work serves to further knowledge about space weathering processes as well as provide new data on a size fraction relevant to grain toxicity and dust effects on exploration systems.

Sample

Lunar regolith sample 10084 is typical of mare-type soils, and based on Is/FeO analysis it is classified as mature [2]. Prior studies have shown evidence of some mixing with highland material [3]. The main soil components consist of mineral fragments of plagioclase feldspar, ilmenite, olivine, and pyroxene, as well as a predominant amount of diverse glassy grains including pieces of soil agglutinates. As is typically observed in most lunar soil samples, many of the glassy grains in the finest-size fraction of 10084 contain various concentrations of 5-20 nm-sized iron metal (Fe^0) spherules formed as a by-product of micrometeorite impacts and other processes.

Experimental Methods

In order to accumulate grains of the <1 μm size fraction, settling experiments were performed in ethanol using <20 μm sieved material. After 2 hours of gravity induced settling, a droplet was withdrawn, placed on a continuous carbon film copper grid and evaporated. The residual material contained a high concentration of < 1-5 μm grains. Two separate mounts were prepared for the JEOL 2000 Transmission Electron Microscope operating at 200 kV. Using a digital camera, over 200 grains between 0.05 μm and 1 μm were imaged. Each grain was subjected to EDS analysis with conversion of peak intensities to element concentrations using the Cliff-Lorimer method [4].

Results

Of over 200 grains analyzed, more than 80% of these were compositionally and morphologically complex glassy grains, detailed in Table 1. The predominant morphological type of these grains are spherules (45%) shown in Figure 1. In addition, 25% of the glass grains of all shapes contain nanophase Fe^0 as a significant component (Figure 2). The Fe^0 appears more noticeably in smaller grains 200-400 nm in size. Glasses with an Fe^o component are more commonly oblong or irregularly shaped; spherules generally have little to no nanophase Fe^o.

Table 1. Grain types in 10084 glass

Glass Grain Type	Fraction of Glass (%)
HASP (General)	28.0
• Ultra	• 2.3
• Mare	• 5.8
• Highland	• 11.1
• Indeterminate	• 8.7
Volatile Rich Glasses	11.6
• VRAP	• 1.2
• PVRAP	• 8.1
• High Si	• 2.3
Other Glass	60.4
• Agglutinate	• 13.4
• Glass and Mineral	• 2.3
• All Other	• 44.7

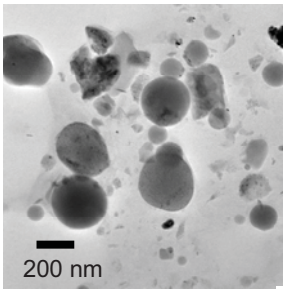

Figure 1. Bright-field TEM images of < 1 um glass spherules in lunar soil 10084.

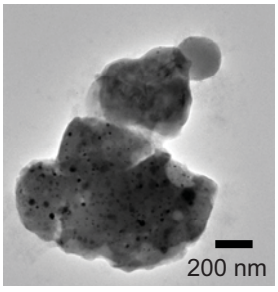

Figure 2. Bright-field TEM images glass grain containing nanophase Fe^o.

The remaining near 20% of non-glass grains are comprised of minerals (Table 2). The average size of the mineral grains, at 374 nm, is much larger than the overall population average of 290 nm. The mineral grains differ in shape and exhibit variable signatures of space weathering consistent with the physical effects of micrometeorite impacts and other processes.

Table 2. Mineral Types in 10084*

Mineral Type	Fraction of Total %	Mineral Fraction %
Plagioclase	12.4	70.3
Ilmenite	2.9	16.2
Pyroxene	1.4	8.1
Olivine	1.0	5.4

*The assessed mineral grains do not include agglutinitic particles or grains attached to glass.

Discussion

When comparing the <1 μm size fraction to the large super-population of < 10 μm grains in terms of chemical composition, grain type and morphology, it is evident this specific population is distinctly different. Over 80% of the material is grain-typed as glass displaying an increase in this component from the previously estimated 45% in the <10 μm soil and <10% in the sub 1 mm size fraction [5]. Regarding morphology, it is observed that the amount of glass spherules present in the sample, at 38% of the total, is much higher than the 5% present at the <10 μm size fraction of the similar Apollo 17 mare regolith [6]. While a portion of these spheres have been interpreted to originate by various degrees of simple impact melting, others may belong to a class of grains significantly affected by volatilization and condensation phenomenon (see below).

The predominance of glass grains within the size fraction investigated raises significant questions about the processes operating on this grain sub-population. These questions can be addressed through compositional trend analysis. There are two broad compositional groups of glassy material; grains with compositions affected predominantly by the process of volatilization, and grains that form exclusively by various degrees of impact melting in a more isochemical manner. Within grains affected by volatilization there is a predictable distribution of glass compositions with respect to volatile content; more Al_2O_3 and CaO indicates greater volatile depletion, as with the HASP (High Aluminum Silica Poor) glasses, and more FeO and SiO_2 is representative of higher volatile element content as in the VRAP grains (Volatile-Rich-Al-Poor) [3]. Compositional variations associated by volatilization operating on these and other compositions can be analyzed using the chemical variation plot in Figure 3. The VRAP and HASP compositions plot at the extremities of the Figure 3 trend.

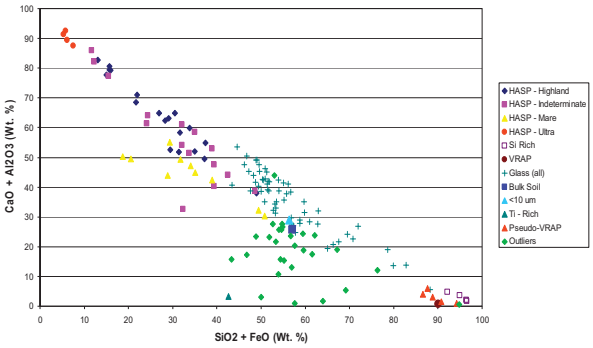

Figure 3. Trend of volatilization displaying particles that do not conform to expected compositions.

VRAP grains form through condensation of the volatile vapours driven off other impact melts and have <5 Wt. % Al_2O_3, 2-5 Wt.% K_2O, and typical concentrations of Na and S [3]. It has been suggested that these vapour condensates would be more prevalent at smaller size fractions due to the high surface area-to-volume ratio necessary to promote vaporization [7]. This is supported by the increased amount of VRAP and Pseudo-VRAP (close in composition to VRAP with <5 Wt. % Al_2O_3) particles found in this sample. At nearly 12% of the total grain population, this finding can be compared to lower amounts in the investigation of a <20 μm size fraction of Apollo 16 lunar soil [3].

The compositional counterparts to VRAP particles are the HASP (High Aluminum Silica Poor) glasses, which concentrate the refractory components not driven off during impact melting and have >16 wt.% Al_2O_3 and <40 wt.% SiO_2 [3]. These glasses can have a highland or mare affinity: highland with <15 wt.% $FeO+MgO+TiO_2$, and CaO/Al_2O_3 >0.7, mare with >15 wt.% $FeO+MgO+TiO_2$ and CaO/Al_2O_3 <0.57 [2],[3]. HASP glasses of indeterminate affinity show poor correlations of the distinguishing components [3],[7]. Similar to reports from studies of <20 μm 10084 soil, highland HASP glasses are nearly twice as common as mare HASP glasses in this study [4]. However, 9% of HASP glasses in this study have an indeterminate affinity based on uncertainty in differentiating highly volatilized mare

from highland grains. This factor makes it difficult to determine their origin with regard to mixing between mare and highland material. As shown in Figure 4, it is evident that both highland- and mare-affinity HASP grains trend towards high Al_2O_3 content, similar to patterns in other samples [3]. In contrast, however, highland- and mare-affinity HASP grains here show different Al_2O_3 enrichment slopes (Figure 4). It is interesting, furthermore, that the indeterminate HASP particles closely mirror the highland-affinity trend. This suggests that most, if not all, of the indeterminate HASP glass compositions could be classified as highland affinity. This would make nearly 20% of all glasses derived from highland soil, over 3 times as much as from mare. This may correspond to an increase in mixing of highland material at this finer size fraction generating the more aluminous melts required for highland affinity HASP formation.

It has been suggested that the volatilized Fe from mare HASP glasses recondenses specifically in High Si glasses as nanophase Fe^o spherules [3]. Whereas I find nanophase Fe^o in High Si glasses, I also observe 75% of *all* volatile rich glasses to contain nanophase Fe^o as well. A possible role for Fe^o droplets as condensation nuclei for volatile glasses has been suggested, supported by their uniform internal distribution within the grains [7]**.** Supporting this mechanism is the evidence that 90% of VRAP glass grains contain through-going Fe^0 spherules.

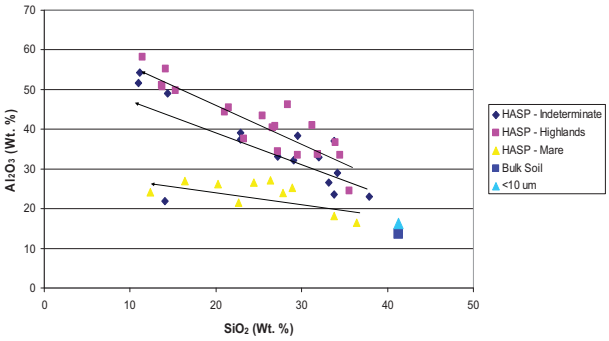

Figure 4. Wt. % Al_2O_3 vs. Wt. % SiO_2 indicating trends towards higher Al_2O_3 content.

Other glass compositions possibly affected by volatilization phenomena are High Ti glasses (Figure 3) that may represent extreme volatile depletion of melts comprised of ilmenite with subordinate silicate material [6].

The remaining compositional groups of grains in the middle of the trend in Figure 3 may be glasses largely unaffected by volatilization. One sub-population in this group falls off the trend line and may be "monomineralic" melts from single mineral grains.

Conclusions

This study documents the properties of the <1 μm grain size fraction of 10084 Apollo 11 lunar regolith. Primary findings of this size fraction investigation include: 1) Significant increase in glass fraction, 2) Increase in VRAP particle occurrence, 3) High concentration of Highland affinity HASP glasses indicating mixing, 4) Correlation between VRAP particle condensation and presence of Fe^0 spherules, 5) Distinct population of glass grains unconformable to volatilization trends.

Acknowledgements

Thanks to Roy Christoffersen for supervisory help, and Kathie Thomas-Keprta, Lindsay Keller, Kent Ross and George-Anne Robinson for technical assistance.

References

[1] Taylor, L.A., Pieters, C., Keller, L.P., Morrison, R.V., McKay, D.S., Patchen, A. and Wentworth, S. (2001) Met. & Planet. Sci., v. 36, 285-299. **[2]** Basu A., Wentworth J.A., McKay D.S. (2001) *Meteoritics and Planetary Science* vol. 36, p. 177 **[3]** Keller L.P., and McKay D.S (1992) *Abstracts Lunar Sci. Conf. 22Nd,* p. 673 **[4]** Cliff, G. and Lorimer, G.W. (1975) J. Microscopy, v. 103, 203.. **[5]** Devine J.M., McKay D.S. and Papike J.J (1982) *Abstracts Lunar Sci. Conf. 13Th*, p. 170-171. **[6]** Norris J.A., Keller L.P. and McKay D.S (1992) *Lunar Science Inst. Workshop on the Geology of the Apollo 17 Landing Site,* p. 44-45 **[7]** Norris J.A., Keller L.P. And McKay D.S (1993). *Lunar and Planetary Institute- 24th LPSC, Part 3,* p.1093-1094.

EXPERIMENTAL CONSTRAINTS ON LOW TEMPERATURE ACID-WEATHERING OF OLIVINE: IMPLICATIONS FOR MARS E. A. Worsham[1], P. B. Niles[2], and M. D. Kraft[3] [1]University of Tennessee (Department of Earth and Planetary Sciences 1412 Circle Drive Knoxville, TN 37996-1410 eps@utk.edu), [2]Astromaterials Research and Exploration Science, NASA/Johnson Space Center (Houston, TX 77058) [3]School of Earth and Space Exploration, Arizona State University (Tempe, AZ)).

Introduction: The Opportunity rover, at Meridiani Planum, Mars, has discovered a large scale sulfate-rich deposit with fine layering, cross bedding, and hematite spherules. Many hypotheses have been proposed to explain the formation of these sediments and each hypothesis has its own implications for the past climate of Mars and the Meridiani Planum region. Leading hypotheses include the Squyres et al.[1] claim that the deposit was formed in a groundwater-fed evaporative playa, suggesting the presence of a substantial amount of acidic groundwater. Other hypotheses suggest that the deposit is a product of either volcanic [2] or impact surge processes [3]. Most recently, it has been suggested that the sediments of Meridiani Planum underwent acid-weathering in a massive dust-ice deposit and were later reworked by aeolian processes [4].

The rate of acid weathering at sub-zero temperatures is poorly understood [4], and sub-zero temperatures are typical on Mars. Additionally, olivine weathering itself has been the subject of many studies which have examined the effects of pH and temperature on weathering at temperatures above 0°C [6, 7, 8]. In particular, it is apparent that the effect of temperature on pH dependence is not well constrained [8].

The goal of this study is to investigate the rate of acid-weathering at very low temperatures (<0°C) in order to test the ice-weathering hypothesis [4]. Under temperatures less than 0°C the weathering rate would necessarily be slower, but the concentration of H_2SO_4 would be higher, possibly mitigating the affect of the cold [4, 5] (Fig. 1). To what degree can we expect weathering to take place in such temperatures, if any at all? Would it be fast enough to create this large deposit? This study will contribute not only to our understanding of possible low temperature weathering on Mars, but also expand our knowledge of olivine weathering to lower temperatures.

Experimental Methods: In these experiments fine grained olivine from Jackson Co., N.C. and coarser grained olivine from San Carlos were exposed to sulfuric acid in batch reactors under different temperature conditions for varying amounts of time. The fine grained olivine had an average grain size of <10 microns to simulate typical size of martian dust grains. The San Carlos olivine was crushed to the 53-124 micron size fraction and cleaned through sonication in ethanol to remove ultra-fine particles adhereing to grain surfaces [6]. The molarities of the H_2SO_4 used were 5M at -52°C and 3M at -20°C and 4°C based on data from Marion [5] (Fig. 1, Table 1). For the room temperature experiments, 3M H_2SO_4 was used for fine grained olivine and 0.1M was used for coarse. Approximately 10 mg of olivine and about 2 ml of H_2SO_4 were measured out for each sample. Separate test tubes containing acid and olivine were put into four different temperature conditions (-52°, -20°, 4°, and 20°C) and allowed to cool. The samples were then removed from their respective temperature conditions and the olivine and acid were quickly combined and returned to their proper temperature. Samples were run

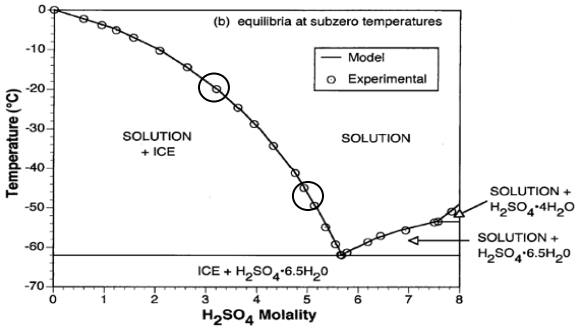

Fig. 1. Phase diagram for the concentration of H_2SO_4 in subzero temperatures. The concentration increases as temperature decreases. The two circles are this study's area of focus. From Marion [5].

Temp. (°C)	H_2SO_4 Molarity	Duration (hrs)
Fine		
-52	5	1-480
-20	3	1-480
4	3	1-480
20	3	1-504
Coarse		
-52	5	1-144
-20	3	1-120
4	3	1-120
20	0.1	1-96

Table 1. The table shows the experimental conditions. The durations shown are what have been analyzed for Mg thus far in the study. The fine grained olivine has an average grain size of < 10 microns and the coarse is between 53 and 124 microns.

for different time periods: 1hr, 5hrs, 24hrs, 48hrs, 5days, 10 days, or 20 days . At the end of the time period, the sample was removed from its environment and 1 ml of the liquid was taken off the top with a 1 ml syringe and a needle (being careful not to get any solid), put into a new test tube, and diluted with 10 ml of DI H_2O. The solid residue was obtained by filtering the remaining liquid with a vacuum filter and letting it dry in an oven for at least 24 hours.

The liquid was analyzed using atomic absorption spectroscopy to obtain the amount of dissolved Mg^{2+} and Fe^{2+}. The samples were diluted with a blank of 0.1% lanthinum chloride and 0.5M H_2SO_4 to varying degrees depending on expected concentration so that they would be within the standards of the machine.

The solid residue was examined using an SEM and the grains were mounted using double sided tape and rubber mat which were then put on an SEM stage with double sided tape. The grains were then carbon coated. Using backscatter electron images and EDS the solid was examined for evidence of weathering.

Results: The atomic absorption spectroscopy of the experimental results for fine and coarse grained olivine weathering shows that the Mg^{2+} and Fe^{2+} concentrations generally increase with temperature and duration, with the coarse concentrations lower than the fine. The fine grained olivine results indicate that the concentrations of Mg^{2+} reach a local maximum of about 0.003 mol/L around 24-48 hrs in the -52°C freezer, and then fall and level off for a time before gradually rising again to about the same concentration between 10 days and 20 days. At 24 hrs, the -20°C Mg concentrations show a maximum and then they steadily increase to about 0.025 mol/L at 336 hrs before leveling off and falling slightly. The 4°C samples' concentrations seem to have a parabolic shape, peaking at about 0.062 mol/L at 144 hrs. The concentrations reach a local maximum around 24 hrs in room temperature and then continue to increase to 0.081 mol/L. The concentrations of Fe^{2+} roughly mirror those of Mg^{2+}, but at lower levels.

The coarse grained concentration results for Mg^{2+} show that the -52°C samples drop from approximately 1.06×10^{-4} to 5.52×10^{-5} mol/L and then rises and falls again. The three other temperature concentrations increase steadily, with the -20°C reaching a plateau, and the 4°C overtaking the 20°C in highest concentrations. These concentrations were converted into rates by using the equation R_{Mg}= (n/(800*m*s), where R_{Mg} is the rate of dissolution of Mg, n is the number of moles of Mg in the solution after the reaction, 800 is the surface area in cm^2/g (from Pokrovsky and Schott [7], whose grain sizes are comparable to this study's coarse grain sizes), m is the original mass of olivine in grams, and s is the duration of the reaction in seconds. The logs of these rates are plotted against experimental duration in Figure 2. The Mg dissolution rate decreases swiftly at first and then becomes fairly stagnant between 5 and 48 hrs for each temperature. Additionally, the rate of dissolution in 4°C goes above that of room temperature.

The results of the SEM analysis are summarized in figures 4 and 5; a representative picture of a grain from the longest duration in the -20° C freezer and the EDS for point 1on figure 4, which indicates an enrichment in Si compared to the abundance of Si in pure olivine.

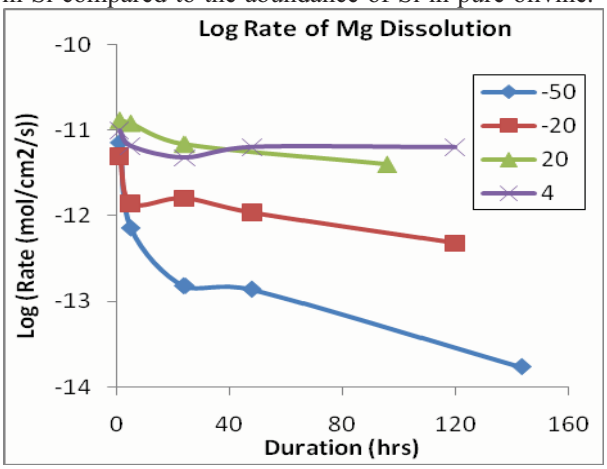

Fig. 2. The log rates of Mg and Fe dissolution in $mol/cm^2/s$ in each different temperature condition for coarse grained olivine versus duration of the reaction.

Discussion: The results of the experiments are comparable to previous work which reported weathering rates for San Carlos olivine in a pH 2.13 solution to be -11.65 [Log (R_{Mg})] after 8 hours [7] (R_{Mg} is the weathering rate in $mol/cm^2/s$). Our results for the room temperature experiment at pH = 1.97 showed an average rate of -11.16 after 24 hours [Log (R_{Mg})].

Initial rates for the low temperature experiments were also comparable to higher temperature experiments indicating that for the initial 24 hours the higher acid concentrations compensate for the lower temperatures (Fig. 2).

The results of the atomic absorption analysis for the coldest temperature experiments show the lowest concentrations in both Mg^{2+} and Fe^{2+}. The average rate of dissolution rapidly decreases as time goes on, showing that temperature plays a very important role in the weathering process. The -52°C samples in all cases show a much more rapid decrease in weathering rate than for the higher temperatures (Fig 2). This could be caused by different rates of diffusion. At the very cold temperatures we might expect a much smaller portion of the acid solution to be accessible to the olivine grain

surfaces due to much slower diffusion rates. Thus the weathering rate rapidly decreases after initial contact between the olivine and the acidic solution due to slow diffusion rates of ions in the solution.

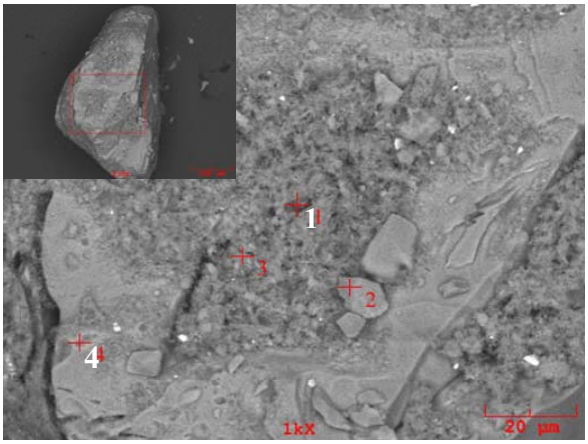

Fig. 3. Backscatter image of sample 14N (-20° C, 20 days). Note different colors of smooth and rough areas. Rough areas of adhereing particles are more weathered than the smooth areas.

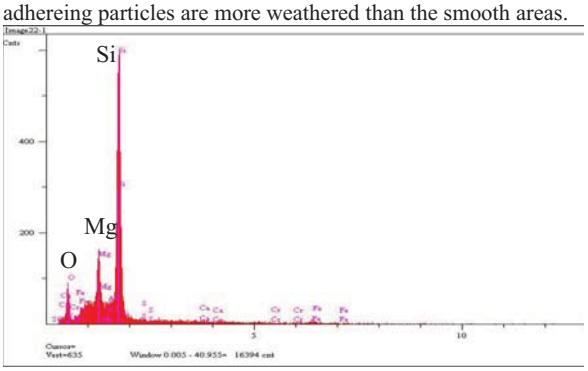

Fig. 4. EDS of a grain from sample 14N (-20° C, 20 days) from point 1 on Figure 4. The Si is much higher than the Mg, presumably because of the dissolution of some Mg as a result of weathering.

SEM analysis: The results of the SEM data show some weathering of the solid in the coldest temperatures. The EDS data for the least weathered sample, which was in the -52° C freezer for one hour, shows that it has a typical forsterite composition and the backscatter image shows no compositional differences. There are also no weathering textures along the edges of the grains or on the smaller adhering particles. Figure 4 shows a grain of the 20 day fine grained sample in the -20°C freezer and a close up of an area of adhering particles. The backscatter image of the whole grain shows that the areas of adhering particles are darker, indicating compositional differences. Upon taking an EDS of the rougher area the Mg to Si ratio is much lower (Fig. 5). Additionally, point 4 may constitute a weathering texture, as it is on an edge of the grain and it is a darker color than the surrounding area. These rougher areas with low Mg:Si may be a magnesian phyllosilicate mineral or simply an amorphous weathering residue.

Conclusions and Future Work: Weathering rates of forsteritic olivine in sulfuric acid solutions at temperatures as low as -52°C are comparable (same magnitude) to weathering rates observed for mildly acidic solutions at room temperature. However, there does seem to be a strong limiting factor, possibly caused by slow diffusion, that slows down the weathering reaction after the initial 8 to 24 hours. Thus stronger acid concentrations in colder subzero temperatures does not overcome the effects of lower temperatures, but does make weathering rates comparable to those at room temperatures. Clearly understanding the cause of the low-temperature limitations will greatly aid in understanding the importance of this process on Mars.

In the future an experimental run in room temperature with 0.1M H_2SO_4 will be analyzed, along with the Fe^{2+} concentrations for the final fine grained samples and all the coarse. Also, weathering experiments are planned using different materials including: anorthite, enstatite, and basaltic glass with compositions similar to the martian meteorite Shergotty.

[1] Squyers, S.W. et al. Two years at Meridiani Planum: Results from the Opportunity Rover. Science 313, 1403-1407 (2006) [2] McCollom, T.M. & Hynek, B.M. A volcanic environment for bedrock diagenesis at Meridiani Planum on Mars. Nature 438, 1129-1131 (2005). [3] Knauth, L.P., Burt, D.M., & Wohletz, K.H. Impact origin of sediments at the Opportunity landing site on Mars. Nature 438, 1123-1128 (2005). [4] Niles, P.B. & Michalski, J. Meridiani Planum sediments on Mars formed through weathering in massive ice deposits. Nature Geoscience 2, 215-220 (2009). [5] Marion, G.M., A molal-based model for strong acid chemistry at low temperatures (<200 to 298 K). Geochimica et Cosmochimica Acta 66, 2499-2516 (2002). [6] Wogelius, R.A. & Walther, J.V., Olivine dissolution at 25°C: Effects of pH, CO_2, and organic acids. Geochimica et Cosmochimica Acta 55, 943-954 (1990). [7] Pokrovsky, O.S. & Schott, J., Kinetics and mechanism of forsterite dissolution at 25°C and pH from 1 to 12. Geochimica et Cosmochimica Acta 64, 3313-3325 (2000). [8] Chen, Y. & Brantly, S.L., Dissolution of forsteritic olivine at 65°C and 2 < pH < 5. Chemical Geology 165, 267-281 (2000).

NOTES

NOTES